

2013

Microfluidics and real-time behavioral analysis: Tools for screening drugs, toxins, and pathogens

Archana Parashar
Iowa State University

Follow this and additional works at: <https://lib.dr.iastate.edu/etd>

 Part of the [Biomedical Commons](#), [Electrical and Electronics Commons](#), and the [Social and Behavioral Sciences Commons](#)

Recommended Citation

Parashar, Archana, "Microfluidics and real-time behavioral analysis: Tools for screening drugs, toxins, and pathogens" (2013).
Graduate Theses and Dissertations. 13527.
<https://lib.dr.iastate.edu/etd/13527>

This Dissertation is brought to you for free and open access by the Iowa State University Capstones, Theses and Dissertations at Iowa State University Digital Repository. It has been accepted for inclusion in Graduate Theses and Dissertations by an authorized administrator of Iowa State University Digital Repository. For more information, please contact digirep@iastate.edu.

Microfluidics and real-time behavioral analysis: Tools for screening drugs, toxins, and pathogens

by

Archana Parashar

A thesis submitted to the graduate faculty
in partial fulfillment of the requirements for the degree of
DOCTOR OF PHILOSOPHY

Major: Electrical Engineering

Program of Study Committee:
Santosh Pandey, Major Professor
Timothy Bigelow
Sumit Chaudhary
Jaeyoun Kim
Jiming Song

Iowa State University
Ames, Iowa
2013

Copyright © Archana Parashar, 2013. All rights reserved.

TABLE OF CONTENTS

	Page
LIST OF FIGURES.....	v
LIST OF TABLES	viii
NOMENCLATURE.....	ix
ACKNOWLEDGEMENTS	x
ABSTRACT	xii
CHAPTER 1 Introduction	1
1.1 Microfluidics for <i>C. elegans</i> research	2
1.1.1 Behavioral arenas for <i>C. elegans</i>	4
1.1.2 Whole-animal drug screening	7
1.2 Microfluidic to study plant root systems.....	11
1.3 Device fabrication	13
1.3.1 Mask design and SU-8 master mold	13
1.3.2 PDMS replication.....	16
1.4 Imaging and device setup.....	17
1.5 Worm tracking program	18
1.6 Thesis Organization.....	20
1.7 References	21
CHAPTER 2 Amplitude-modulated sinusoidal microchannels for observing adaptability in <i>C. elegans</i> locomotion	25
2.1 Abstract	25
2.2 Introduction	26
2.3 Materials and Methods	28
2.3.1 <i>C. elegans</i> strains and culture.....	28
2.3.2 Experimental setup.....	29
2.3.3 Worm manipulation and imaging.....	29
2.4 Results	31
2.4.1 Average forward velocity.....	31
2.4.2 Number and duration of stops	33
2.4.3 Range of contact angle	34
2.4.4 Cut-off region	35
2.5 Discussion	37
2.6 Conclusion.....	41

2.7 References	42
CHAPTER 3 Multi-parameter behavioral analyses provide insights to mechanism of cyanide resistance in <i>Caenorhabditis elegans</i>	44
3.1 Abstract	44
3.2 Introduction	45
3.3 Materials and Methods	47
3.3.1 <i>C. elegans</i> strains and culture	47
3.3.2 HCN gas exposure assay	48
3.3.3 RNA interference assays	49
3.3.4 Quantitative real-time PCR	50
3.3.5 Microfluidic assay with cyanide in aqueous solution	50
3.4 Results	52
3.4.1 Over-activation of <i>hif-1</i> confers resistance to HCN gas	52
3.4.2 Partial loss-of-function in <i>egl-9</i> mutations confer intermediate resistance phenotypes	53
3.4.3 Design of the microfluidic device	54
3.4.4 Presence of food as an essential factor for consistent worm movement	55
3.4.5 Multi-parameter behavioral analysis in aqueous cyanide solution	56
3.4.6 Deciphering the role of <i>cysl-2</i> in cyanide resistance	64
3.4.7 Robustness of the assay and broader applications	67
3.5 Discussion	70
3.5.1 Higher spatiotemporal resolution in microfluidic assay	71
3.5.2 Genetics of cyanide resistance in <i>C. elegans</i>	73
3.6 Conclusion	74
3.7 References	75
CHAPTER 4 Algorithm-guided discovery of new combinations of existing drugs for parasitic worms	78
4.1 Abstract	78
4.2 Introduction	79
4.3 Material and Methods	84
4.4 Results	84
4.4.1 Iterations of algorithmic search	84
4.4.2 Performance of different cocktails	88
4.5 Discussion	92
4.6 Conclusion	94
4.7 References	95
CHAPTER 5 Plant-in-chip: Microfluidic system for studying root growth and pathogenic interactions in <i>Arabidopsis</i>	98
5.1 Abstract	98
5.2 Introduction	98
5.3 Material and Methods	100

5.4 Results and discussion.....	101
5.4.1 Characterization of root growth parameters.....	101
5.4.2 Imaging root-pathogen interactions	104
5.5 Conclusion.....	106
5.6 References	107
CHAPTER 6 Conclusions	110
LIST OF PUBLICATIONS	114
APPENDIX	117

LIST OF FIGURES

	Page
Figure 1.1 Life-cycle of <i>C. elegans</i> grown at 22°C	2
Figure 1.2 Worm chips test adaptability to different oxygen levels	5
Figure 1.3 Olfactory functions of <i>C. elegans</i> tested in behavioral assays	6
Figure 1.4 Pillar structures enhance the crawling behavior	7
Figure 1.5 Drug screening on <i>C. elegans</i> facilitated by microfluidics.....	8
Figure 1.6 Capture and imaging of multiple worms using droplet microfluidics ...	10
Figure 1.7 Observation of <i>Arabidopsis</i> root growth in microfluidics	12
Figure 1.8 Steps of microfluidic device fabrication	14
Figure 1.9 Raw greyscale images are processed by our worm tracking software...	19
Figure 2.1 Overview of the system and device design.....	28
Figure 2.2 Wild-type <i>C. elegans</i> crawling in different sections of a modulated sinusoidal channel	30
Figure 2.3 Average forward velocity versus channel amplitude is plotted for the three L4-stage <i>C. elegans</i> strains: <i>wild-type</i> , <i>lev-8</i> and <i>unc-38</i>	31
Figure 2.4 Average forward velocity and ratio of amplitude to wavelength (A/λ) for the three <i>C. elegans</i> strains on 2.5% agarose plates are shown.....	33
Figure 2.5 Average number (a) and duration (b) of stops versus channel amplitude are plotted for the three <i>C. elegans</i> strains (<i>wild-type</i> , <i>lev-8</i> and <i>unc-38</i>)	33
Figure 2.6 Illustration of the range of contact angle for a L4-stage <i>wild-type</i> worms in two sections of the modulated sinusoidal channel	34
Figure 2.7 Range of contact angle versus channel amplitude is plotted for the L4-stage <i>C. elegans</i> (<i>wild-type</i> , <i>lev-8</i> and <i>unc-38</i>).....	35
Figure 2.8 The lower and upper cut-off regions in the modulated sinusoidal channels are shown for the <i>wild-type</i> , <i>lev-8</i> and <i>unc-38</i> <i>C. elegans</i>	36

Figure 2.9 Image analysis using worm tracking program	37
Figure 3.1 <i>C. elegans</i> susceptibility to HCN gas	48
Figure 3.2 Setup for imaging the microfluidic assay	51
Figure 3.3 Characterizing worm movements in HCN gas assay.....	52
Figure 3.4 Average centroid velocity of worms without food (<i>E. coli</i>) in microfluidic chambers.....	56
Figure 3.5 Effects of cyanide on worm velocity in the microfluidic assay.....	58
Figure 3.6 Total distance traveled in the microfluidic chambers	59
Figure 3.7 Behavioral raster plots of the centroid velocities.....	61
Figure 3.8 Range and distribution of the average centroid velocities	62
Figure 3.9 Number of pauses in the microfluidic chambers	64
Figure 3.10 Effects of <i>cysl-2</i> depletion on cyanide resistance	65
Figure 3.11 Effects of <i>egl-9</i> depletion on cyanide resistance.....	66
Figure 3.12 Scaling-up the microfluidic technique with multiple worms in individual chambers	68
Figure 3.13 Applicability of the microfluidic device	69
Figure 3.14 Summary list of parameters extracted from gas exposure assay and microfluidic assay	71
Figure 4.1 Percentage responses of worms in the four drugs.....	85
Figure 4.2 Each iteration has eight cocktails to be tested	87
Figure 4.3 The velocity of body centroid is averaged over 600 seconds and is plotted for every cocktail through the four iterations.....	89
Figure 4.4 The velocity of body centroid is averaged over the last 120 seconds of the entire experimental time (i.e. 600 seconds).....	89

Figure 4.5 The total distance travelled by individual worms is calculated over the entire length of 600 seconds.....	90
Figure 4.6 Instantaneous average velocities of worms in different cocktails can be grouped into four categories.....	91
Figure 5.1 Schematic of the microfluidic device and experimental setup	100
Figure 5.2 Snapshot of multiple <i>Arabidopsis</i> roots growing in the microchannels	102
Figure 5.3 Root growth parameters measured during hydroponic growth of the <i>Arabidopsis</i> plants in the microfluidic device with different concentrations of growth media.....	103
Figure 5.4 Measurements of root diameter and cell length.....	104
Figure 5.5 Interactions between the <i>Arabidopsis</i> roots grown in microfluidic device with two plant pathogens	105
Figure 5.6 Time-lapsed images of <i>P. sojae</i> interaction with <i>Arabidopsis</i> root in microchannels.....	106

LIST OF TABLES

	Page
Table 1.1 Summary of microfluidic device fabrication steps	15
Table 3.1 Comparison of relative <i>cysl-2</i> mRNA expression levels	67
Table 4.1 Concentration keys and color codes corresponding to each drug concentration that is later used in the different cocktails predicted by the FSC algorithm	86

NOMENCLATURE

ANOVA	Analysis of Variance
CGC	Caenorhabditis Genetics Center
DNA	Deoxyribo-Nucleic Acid
EC ₅₀	Effective Concentration 50
FSC	Feedback System Control
GUI	Graphic User Interface
HCN	Hydrogen Cyanide
HIF-1	Hypoxia-Inducible Factor-1
IPA	IsoPropyl Alcohol
KCN	Potassium Cyanide
MEMS	MicroElectroMechanical Systems
MS	Murashige and Skoog
nAChR	Nicotinic AcetylCholine Receptor
NGM	Nematode Growth Medium
OD	Optical Density
PCR	Polymerase Chain Reaction
PDMS	PolyDiMethylSiloxane
RNA	Ribo-Nucleic Acid
ROI	Regions of Interest
SBN	Sugar Beet Nematode

ACKNOWLEDGEMENTS

Foremost, I would like to express my sincere gratitude to my advisor Dr. Santosh Pandey for his continuous support of my study and research, motivation, enthusiasm, and immense knowledge. His guidance helped me in all the time of research and writing of this thesis. I could not have imagined having a better advisor and mentor for my Ph.D. study.

I would like to thank the rest of my thesis committee members: Dr. Sumit Chaudhary, Dr. Timothy Bigelow, Dr. Jiming Song, and Dr. Jaeyoun Kim for their guidance and support throughout the course of this research.

In addition, this thesis was made possible by contributions from several individuals. I learnt numerous experimental techniques from Dr. Jo Anne Powell-Coffman, Dr. Richard Martin, Dr. Alan Robertson, and Dr. Donald Sakaguchi. I am fortunate to have free access to fabrication equipment and biosafety cabinet in the laboratories of our bioengineering faculty, including Dr. Jaeyoun Kim, Dr. Liang Dong, and Dr. Timothy Bigelow.

I cherish my interactions and collaborative work with graduate students such as Jenifer Saldanha, John Carr, Baozhen Chen, Roy Lycke, Zach Njus, Rachana Kaul. In the past years, it was a pleasure working with undergraduate students in our lab, many of which helped me develop/refine the worm tracking software and test new experimental methods. In particular, I thank Richard Gibson, Kyle Peterson, and Justin May for helping develop data analysis toolbox, Zach Njus and Douglas Feldman for writing

MATLAB based pattern recognition program, and Roy Lycke for help in device development and testing.

Our UCLA collaborators Dr. Chih-Ming Ho and Dr. Xianting Ding provided access to their algorithm for identifying new drug cocktails. I gratefully acknowledge their invaluable advice and consistent help. The departmental staff, particularly Vicky Thorland-Oster, and the graduate committee chairs, were always proactive in guiding me through my graduate program.

I also would like to thank my previous advisors Dr. Yong Li, Dr. William Dean, and Dr. Thomas Geoghegan at University of Louisville, Kentucky who gave me an opportunity to work on miRNA and allowed me to learn molecular biology techniques.

Last but never the least, I thank my parents, brothers and entire family for their constant love, encouragement, and support throughout my life.

ABSTRACT

The concept of *in vivo* screening of whole animals that model diseased conditions, in contrast to *in vitro* tests on cell cultures and tissues that may not translate to clinical trials, is now gaining wide-spread acceptance. One model whole animal, *Caenorhabditis elegans*, has been extensively studied to understand molecular mechanisms of ageing, cell death, development, and neuronal signaling. Because of its small size, this worm is especially suited for microfluidic systems having microscale geometries, regulated fluid flow, and imaging options.

In this thesis, a survey of some microfluidic systems for *C. elegans* research is first presented (Chapter 1). Methods of capturing and restraining single worms, exposing them to chemical stimuli (e.g. gases, drugs, toxicants), and reading signals from the pharynx and neurons are discussed. The following chapters describe our work on understanding worm behavior in different microenvironments using a combination of microfluidics, real-time imaging, and computer-controlled data collection. The engineering tools developed in this work are aimed to be simple in operation/handling, reliable and robust, information rich, portable for easy transport, and requiring minimal human intervention.

We designed a series of sinusoidal microchannels with fixed wavelength and modulating amplitude to study the locomotion patterns of *C. elegans* (Chapter 2). The sinusoidal microchannels attempt to mimic the physical nature of soil and test the worms' ability to bend their bodies during navigation. The simple, passive locomotion

assay is able to differentiate the wild-type worms from mutants showing uncoordinated or quasi-uncoordinated movement.

The natural worm movement changes upon exposure to chemicals or toxins (e.g. hydrogen cyanide). Exposure to gaseous hydrogen cyanide kills wild-type *C. elegans*; however, deletion of specific genes confers varying levels of resistance to the worms. We designed a microfluidic device to characterize the toxicity of aqueous potassium cyanide and conferred resistance in mutants lacking specific genes (Chapter 3). Results from microfluidic experiments were consistent with those from gas assay experiments.

The above platform was employed to test the effectiveness of four commercially available drugs known to paralyze the worm's neuromuscular system (Chapter 4). We observed interesting phenotypic differences in each drug environment, suggesting that an optimal combination of the four drugs may be more effective than individual drugs, even at lower dosage. We used an algorithmic search method, provided by Dr. Chih-Ming Ho, to find this winning drug cocktail through searching 32 combinations. The idea of creating superior-performing cocktails from existing drugs using algorithmic search, in contrast to discovering new drugs using biologically-driven hypotheses, is compelling for the pharmaceutical industry.

Besides pharmacology, the non-parasitic *C. elegans* is a widely accepted model in parasitology as most parasitic worms have complex life-cycles and impractical for imaging in their natural environments. These challenges lured us to design a microfluidic platform for growing *Arabidopsis* plants and imaging live roots within microchannels (Chapter 5). After 7-days period, the roots were inoculated with plant-parasitic worms

and imaged for another 10 days. Unlike previous microfluidic platforms designed for short-term experiments, this system showed the possibility of conducting very long-term experiments in microfluidics.

Several aspects of the presented devices and tracking program have been adopted by researchers working on other parasites. Depending on the parasite under study, the original chip dimensions and geometry were altered for specific needs. The tracking program now has a graphic-user-interface for easy video capture, compression, and post-processing. In addition, we are regularly striving to make our system simple and user-friendly so that the developed techniques can be transferred to biology laboratories.

Chapter 1

Introduction: Microfluidics for whole-organism studies

Microfluidics refers to the manipulation, and analysis of small (10^{-9} to 10^{-18} liters) amount of fluid within physical structures of micrometer dimensions.¹⁻³ This interdisciplinary field has been widely adopted for studying biological processes, chemical reactions, drug screening, and lab-on-chip diagnostics at the small scale.³ Notable benefits of microfluidic systems, compared to macro-scale platforms, include small sample volumes, low cost of reagents, faster screening, improved data resolution, higher information content, and automated sample preparation and handling.³

Silicon fabrication techniques to realize MicroElectroMechanical Systems (MEMS) with microscale features (ranging from 1 to 100 μm) were modified to establish the fabrication protocols of microfluidic devices.^{2,4} In microfluidics, soft lithography involves the process of fabricating master molds, which is followed by the application of a silicone elastomer, polydimethylsiloxane (PDMS).⁴⁻⁶ This elastomer is optically transparent, gas permeable, non-toxic, inert, and compatible with aqueous solutions – thus making it suitable for microscopic observation and biological tests. The past decade has witnessed an exponential rise in the myriad of biological experiments

that can be performed in two- and three-dimensional PDMS-based microfluidic devices.^{6,7} With the ability to culture different cell lines over a long time period with controlled fluid exchange, microfluidics has helped us gain insights into cell migration, cell proliferation, intercellular communication, tissue regeneration, and separation of desired cell types.^{1,8} With the ability to entrap, sort, and image single organism on-demand, microfluidics has recently accelerated our understanding of model microorganisms and functioning of their neuromuscular systems.⁹⁻¹³ Research on the following three organisms have significantly benefitted from our ability to engineer microfluidic devices: nematode *Caenorhabditis elegans*,¹⁴ fruit fly *Drosophila melanogaster*,¹⁵⁻¹⁷ and the zebra fish *Danio rerio*.¹⁸

1.1 Microfluidics for *C. elegans* research

Caenorhabditis elegans was the first animal whose genome was successfully sequenced.¹⁹ The life-cycle of this worm is illustrated in Figure 1.1.

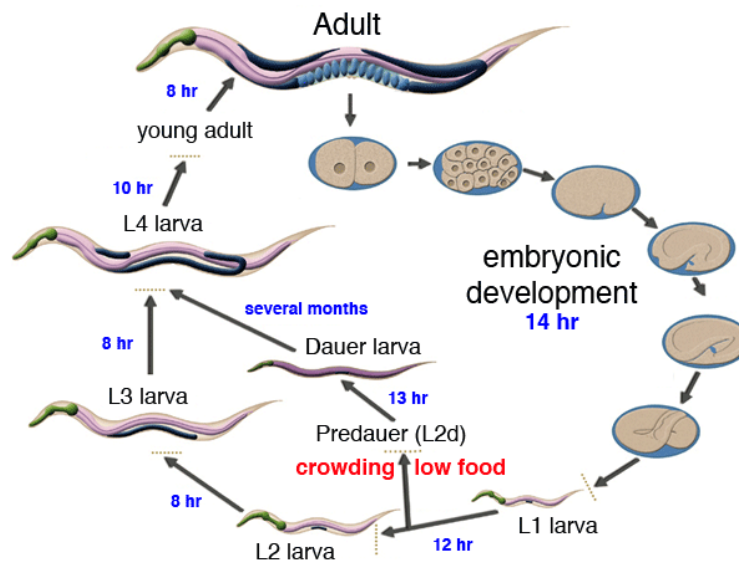


Figure 1.1 Life-cycle of *C. elegans* grown at 22°C (www.wormatlas.com).

Several attributes make this organism an attractive model in biology, such as short lifespan of 18 days, ease of culture in standard laboratories, conserved genes in offsprings, virtually transparent anatomy, and non-parasitic nature.²⁰⁻²⁴

Before the advent of microfluidics, most *C. elegans* research was limited to manual observation of *C. elegans* cultures on agarose plates for signs of behavioral changes upon applying external stimuli (e.g. gas mixtures, liquid chemical or toxins, mechanical stimulation).^{14,22,25} Some typical parameters that quantified behavioral changes on agarose plates were worm movement, number of alive/dead worms, number of eggs hatched, lifespan, and ratio of males to females. Because of the time-consuming nature of the experiments, it was difficult to manipulate experimental protocols and test multiple parameters on different mutants within a reasonable timeframe.

The microfluidic technology provided a range of devices that eventually became indispensable for researchers in *C. elegans* biology.^{11,12,20-23,26-32} In this regard, some important breakthroughs were the invention of leak-free membrane valves,³³ incorporation and parallel operation of these valves to control fluid flow, fabrication of three-dimensional structures within microchannels, and ability to apply on-chip mechanical suction to entrap organisms.^{11,34,35} In addition, significant progress in the area of real-time imaging and automated pattern recognition programs was made to aid the microfluidic experiments and capture behavioral changes in the organisms without human intervention.^{21,27,28,33,36}

In general, key functions of microfluidic systems in *C. elegans* research fall in three categories: worm entrapment or restricting single worms at defined locations,

worm handling or physically moving/transporting worms to desired locations, and worm imaging or visualization of whole animal and its internal anatomy.^{36,37} Different microfluidic devices or systems integrating multiple microfluidic devices have been designed to study the worm's olfactory functions, neuromuscular working, and behavioral preferences.^{12,21-23,26,32} In recent years, there also has been a great emphasis on adding automation steps and computer-controlled acquisition of experimental data. Progress in bioinformatics and combinatorial chemistry has further enabled the pursuit of hypothesis-driven experiments on microfluidic platforms. In our view, the main challenge in microfluidics lies in defining the exact biological process we wish to study in *C. elegans*, devising simple yet efficient device designs to accomplish the goals, formulating ways to gather relevant information, and eventually proving a hypothesis using multiple approaches.^{14,22,24,30,38} More importantly, the developed technology platforms should be simple and portable to be adopted by biologists in their laboratories. In the next section, we discuss some examples of novel microfluidic platforms that gained significant attention from the scientific community for their simplicity, innovativeness, information content, and ease of adoption.

1.1.1 Behavioral arenas for *C. elegans*

Worm chips have been developed to study behavioral responses of these organisms to controlled chemical stimuli (with spatial and temporal gradient).^{10,24,26,32} Behavior of worms has been tested in microfluidics having dissolved gas concentrations, nutrients, chemoattractants, pheromones, pathogenic substances, and temperature. In this context, one of the pioneering works was carried out in the laboratory of Cornelia

Bargmann, a renowned *C. elegans* biologist.³⁹ Her group demonstrated behavioral response of *C. elegans* in microscale chambers with a spatially varying oxygen flow (Figure 1.2a). Spatial gradients of gases were generated in flow channels adjacent to the chamber housing the worms. Temporal step changes in the concentrations of oxygen or carbon dioxide have also been applied on single worms, with the ability to image neuronal activities during gas exposure (Figure 1.2b).¹²

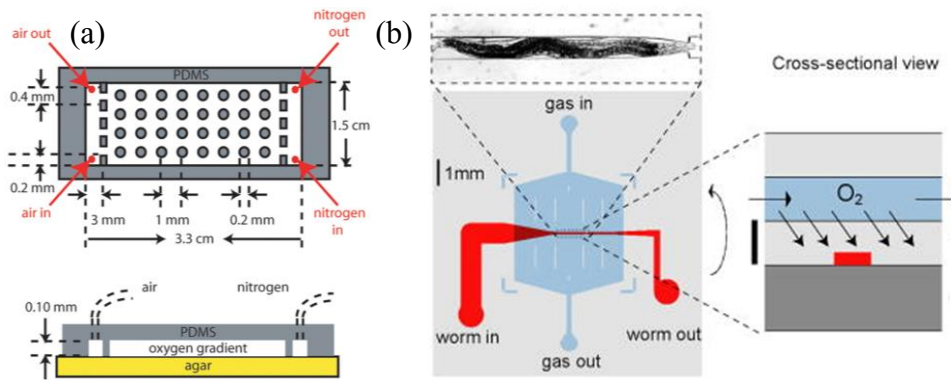


Figure 1.2 Worm chips test adaptability to different oxygen levels. **(a)** Oxygen gradients are established in the flow channel while worms are housed in a PDMS chamber. Top: top view, bottom: side view.³⁹ **(b)** Worms are immobilized in the PDMS channel and exposed to temporal changes in oxygen concentration.¹²

The preference of worms towards different odors can also be studied in microfluidic devices. In one example, an eight-arm maze was fabricated and placed on top of an agarose plate (Figure 1.3a).¹⁸ Worms were expected to differentiate and choose among four different odors. It was observed that trained worms exhibited directed movement towards food odors over odors from pathogenic bacteria. Another classic example developed a microfluidic system to test olfactory functions of entrapped single worms in constricted channel (Figure 1.3b).³² The worm trap, created by mechanical suction, allowed the worm's nose to protrude into a channel where chemicals could be

delivered. Four individual channels were used to inject chemicals, buffer or dyes, and related neuronal activity was imaged using a high-resolution microscope.

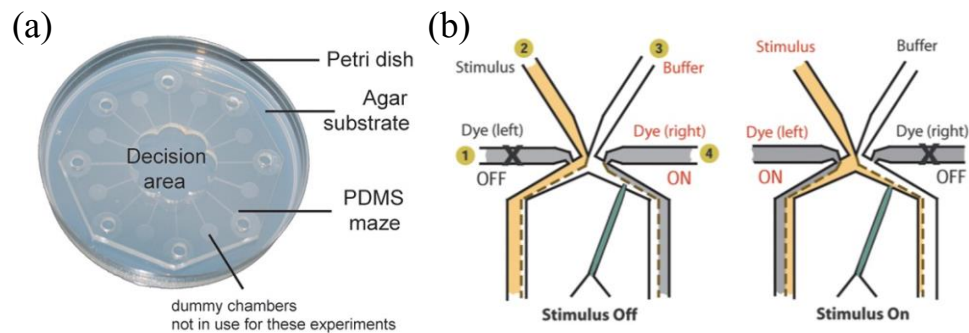


Figure 1.3 Olfactory functions of *C. elegans* tested in behavioral assays. **(a)** Worms are placed in the central chamber of the maze and allowed to differentiate between odors from pathogenic and non-pathogenic bacteria.¹⁸ **(b)** Immobilized worms are exposed to high-osmotic strength chemical stimuli and their behavior is correlated to the activity of their interneurons.³²

In our view, restraining worms (partially or completely) may produce unknown stress within them, especially when the restraint is maintained for long time periods. This is the reason why worm biologists still prefer to observe worm behavior in macroscale agarose plates where the organisms are freely moving and surrounded by abundant bacterial food. The surface of agarose also provides adequate friction to enable worm crawling. Unfortunately, these unrestrained worms are difficult to image within the limited field-of-view of microscopes, and thus, visual scoring is the preferred choice. Recently, novel microfluidic devices have attempted to emulate the locomotion behavior of free-moving worms on agarose plates, with added experimental capabilities that were not possible in plate systems.

Chemical stimuli in the form of temporal pulses, gradients, and spatial bands have been applied to freely moving worms using inlet channels with different

designs.^{26,40-42} In these cases, pillar structures or micro-posts mimic the natural soil environment that aid worm movement while microscale filters serve to restrict the direct flow of chemicals (Figure 1.4). Besides pillar structures, sinusoidal channels were also found to be suitable for worm crawling.⁴⁰ A series of pillars and sinusoidal channels with different dimensions were fabricated, and it was shown that worms could adapt to a range of physical structures. In a related work, flexible SU-8 pillars were created and the deflection of the pillars (due to the force exerted by the worms against the pillars) was quantified using imaging tools.⁴³

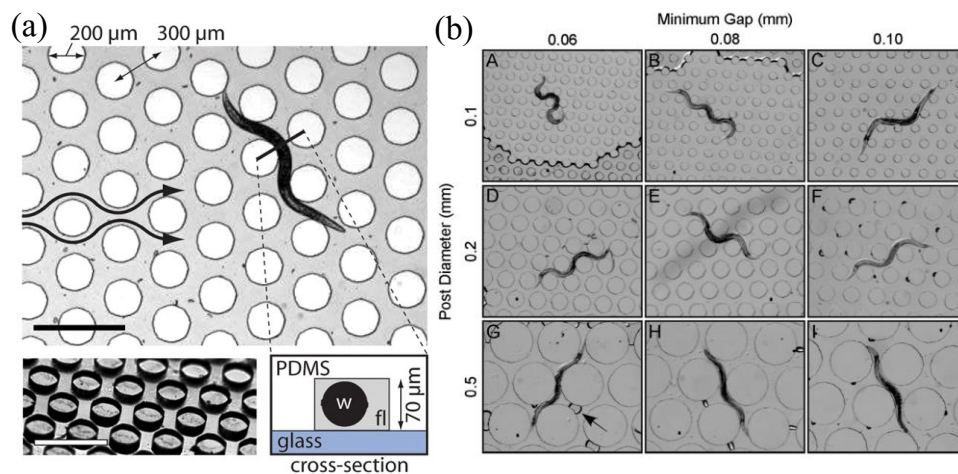


Figure 1.4 Pillar structures enhance the crawling behavior. **(a)** Worms crawling in micro-post filled arena under chemical stimuli, scale bars = 500 μm.²⁶ **(b)** The crawling behavior is tested on artificial dirt chips having pillar structures with varying feature size and spacing.⁴⁰

1.1.2 Whole-animal drug screening

Screening the effectiveness of drugs on model organisms, such as *C. elegans*, has gained significant interest in pharmacology and drug discovery.^{12,14,38,41} Most of these drugs were primarily developed to kill parasitic nematodes and, generally speaking, target and paralyze specific sites of the worm's neuromuscular system. Unfortunately,

parasitic nematodes are becoming increasingly resistant to almost all available drugs, and faster quantification of drug efficacy on readily available organisms is needed. Compared to larger animals (e.g. mouse, chicken, sheep), *C. elegans* provide a relatively cheap subject for *in vivo* drug testing with a simple life cycle and ease of culture.^{32,44} In addition, microfluidics technology provides the advantage of faster screening of multiple drugs, low consumption of compounds, and computerized data acquisition.^{26,45,46}

Our group researched microfluidic approaches for screening drugs and toxins on *C. elegans*. We demonstrated a microfluidic platform to lure free-moving worms into drug-filled chambers and record their behavior pre- and post-exposure to the compound.⁴¹ Different concentrations of levamisole were tested and the response to electric fields was used to quantify the effectiveness of the drug (Figure 1.5a). Recently, the laboratory of Shawn Lockery published their work on measuring pharyngeal signals of single worms.³⁰ Their device comprised an array of microchannels, each capable of trapping single worms, and electrodes to detect their electrical activity under drug exposure (Figure 1.5b).

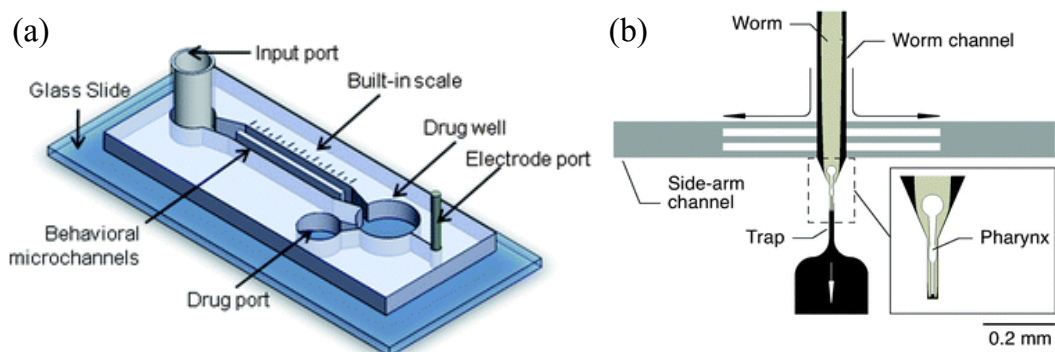


Figure 1.5 Drug screening on *C. elegans* facilitated by microfluidics. **(a)** Our drug screening device uses electro taxis to coax worms in a pre-filled drug well and characterizes the drug effect in behavioral microchannels.⁴¹ **(b)** A single worm is trapped in a worm channel and the electrical activity from its pharynx is recorded during drug exposure.³⁰

Besides screening drugs for pharmacological applications, testing the effects of toxins on *C. elegans* is valuable for studies in environmental sciences, toxicology, and ecology. Toxins can range from chemical compounds that severely damage our nervous system to heavy metal ions that stay within our system for many years.¹⁴ Because *C. elegans* have a short life-cycle, it is relatively easy to conduct short-term and long-term toxicological studies on worm's biology.¹⁹ Furthermore, the conservation of stress response pathways, and availability of transgenic strains, and gene tractability has contributed to the popularity of *C. elegans* in toxicology. In general, most studies track changes in *C. elegans* behavior following exposure to toxins and attempt to predict developmental shifts and/or damage to neuronal pathways. For example, exposure to developmental and/or neurological toxicants shows phenotypic changes in growth, reproduction, size, feeding, and locomotion. Prolonged exposure to toxicants may promote adaptation of these organisms over generations that can be observed using anti-sense RNA technologies. Due to the ease of creating stress-responsive transgenic worms, it is possible to screen different levels of toxicants against genetically modified animals (for their selectivity and sensitivity) and predict the affected genetic pathways.

One of the pioneering works integrating droplet-microfluidics and *C. elegans* drug screening demonstrated a method to automatically generate multiple droplets and entrap single worms within each droplet (Figure 1.6a).⁴⁷ By regulating the flows of drug compound and buffer, each droplet was created with a defined drug concentration. The success rate of worm capture in individual droplets was around 60%. Thereafter, the thrashing of worms was imaged and quantified to characterize the effectiveness of a

given drug concentration. In a related work, a novel trap array with tapered channels was presented to entrap single worms in single wells (Figure 1.6b).³⁴ The device enabled evaluations of worm motility and analysis of fluorescence images simultaneously. A neurotoxin (6-hydroxydopamine, 6-OHDA) was tested shown to trigger movement defects and neuron degeneration in individual worms.

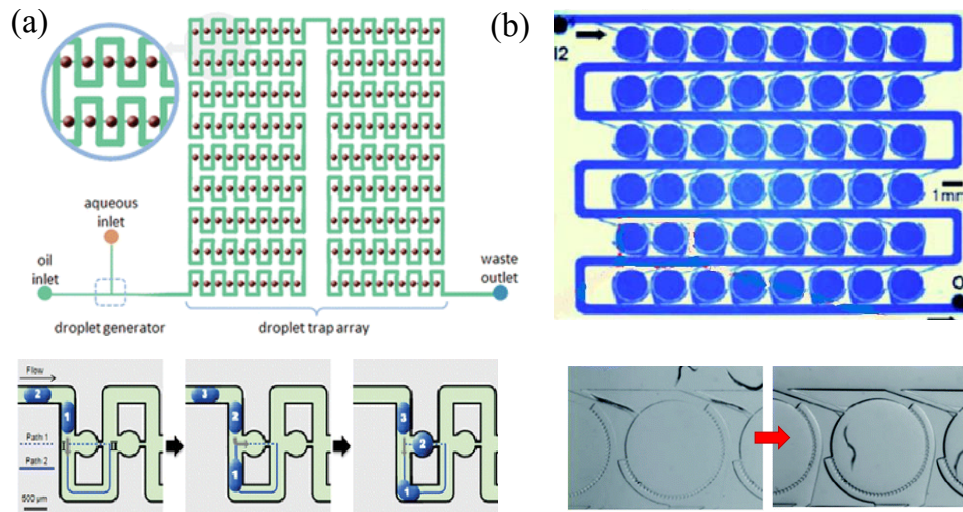


Figure 1.6 Capture and imaging of multiple worms using droplet microfluidics. (a) Droplets containing neurotoxins, created in surrounding oil medium, capture individual worms and the stroke frequency is measured over multiple droplets.⁴⁷ (b) Circular chambers with tapered entrances are used to automatically capture single worms and the locomotion is correlated to 6-OHDA concentration levels.³⁴

It is evident that progress in microfluidic techniques has directly benefitted chemical screening on small animals, and has the potential to revolutionize conventional approaches to drug discovery. As the field progresses, we can expect to witness the development of simpler testing platforms that can be readily adopted by *C. elegans* biologists. Keeping this in mind, we will discuss chemical screening devices that were developed in our laboratory, in close collaboration with biologists, to be simple in design, easy to handle, reliable in operation, and with minimal human intervention.

1.2 Microfluidic to study plant root systems

Till now, we discussed the applications of microfluidics in characterizing *C. elegans* behavior and how this behavior alters in the presence of chemicals or toxins. In parasitology, experiments on *C. elegans* are often used to model some behavioral traits of parasitic nematodes. However, as *C. elegans* is non-parasitic, studies on mechanisms of parasitism require actual parasites that reside and thrive within their specific hosts (e.g. in intestine of animals, roots of plants). We questioned if we can re-create the process of pathogenesis in a microfluidic device, and if so, we could learn valuable information about host-pathogen interactions. After careful consideration, we chose to cultivate live plant roots in microfluidic channels and subsequently inoculate them with plant-parasitic nematodes to observe how worms thrive inside root systems. Our work is described in Chapter 5.

During the initiation of our planned work, there was one recently published paper that showed the feasibility of growing excised plant roots in microfluidic chambers.⁴⁸ *Arabidopsis* plants were grown on agarose plates. Roots were excised and inserted in microfluidic channels for imaging (Figure 1.7a). Two flow channels were created to allow the passage of buffer or stimulants. The rate of root growth was measured over a few hours and it was shown that stimulants promoted the growth rates. The basic concept of demonstrating root growth in microfluidic channels, with the capabilities of chemical flow, was novel. *Arabidopsis* is a model plant system that has thin roots, and thus suitable for microfluidic platforms. This method could be adopted for studying roots of higher plants that have economic importance (e.g. soybean, tomato).

Factors affecting root health can be varied and observation of root structures in soil environments is challenging. These factors include water availability, nutrient concentrations, pH, salinity, light intensity, temperature, and presence of micro-organisms. While it is impossible to re-create the diversity and plurality of biological communities around root systems in their natural habitats, it is possible to create and fluctuate the levels of physical parameters in microfluidics. Recently, a RootChip device described a method to culture parallel *Arabidopsis* roots with time- and content-controlled perfusion of chemicals (Figure 1.7b).⁴⁹

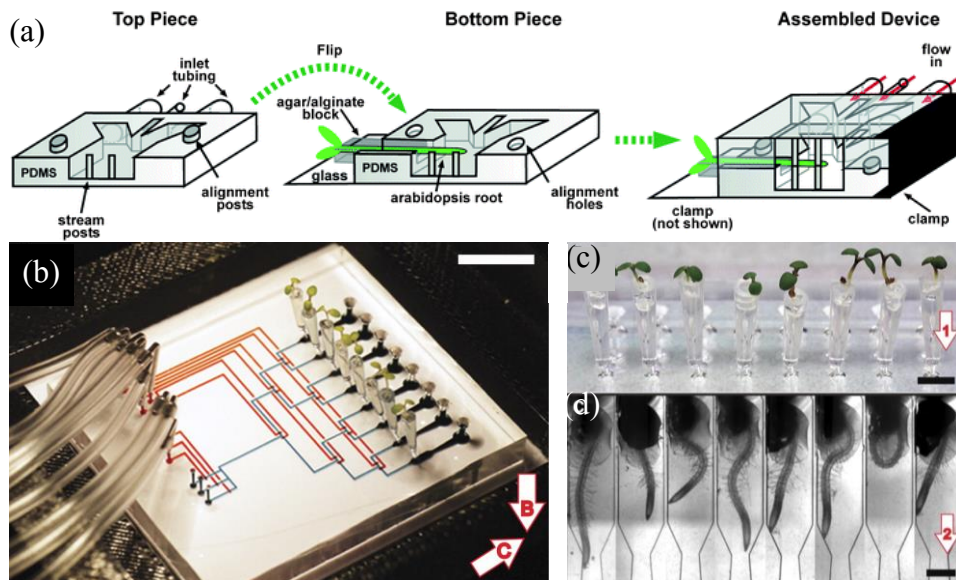


Figure 1.7 Observation of *Arabidopsis* root growth in microfluidics. **(a)** Schematic of a microfluidic platform housing an excised, live *Arabidopsis* root and allowing flow of stimulants around the root system.⁴⁸ **(b)** A microfluidic device (RootChip) with multiple live *Arabidopsis* plants. Scale bar = 1 cm. **(c)** Side view of eight plants in conical containers filled with agarose and mounted onto the chip. Arrow indicates the direction of root growth. Scale bar = 0.5 cm. **(d)** The roots of seedlings are observed 7 days after germination. Scale bar = 0.5 mm.⁴⁹

The RootChip used *Arabidopsis* roots expressing a genetically encoded fluorescence sensor for Förster resonance energy transfer (FRET) measurements. The FRET sensors enabled non-invasive, real-time detection of metabolite levels and fluxes in live root

tissues. In contrast to growing seedlings in 96-well plates, this system allowed precise and rapid environmental changes across multiple roots with the ability obtain images at cellular resolution.

1.3 Device fabrication

In this section, we describe the steps of fabricating PDMS-based microfluidic devices.²⁻⁴ The same protocol is followed to fabricate our chips described in later chapters. The entire process can be grouped into two main categories: soft lithography or the generation of a SU-8 master mold with the desired (negative) features in high-relief, and replication of the master mold using a polymer mixture (PDMS). The process is delineated in the following sub-sections.

1.3.1 Mask design and SU-8 master mold

The device designs are drawn in a computer-assisted design program (e.g., AutoCAD[®] or Adobe Illustrator[®] software) taking the chip dimensions and experimental purpose into consideration. Several alternates of the same design are drawn as it is often difficult to predict the optimal chip dimensions suited for the organisms under test. Typically, we run through 4-5 device designs before starting the actual experiments. The device dimensions are determined by their function and the size of the sample to be used. While designing the mask, the aspect ratio is kept above 1:10 (height to width). Features with $\sim 8 \mu\text{m}$ lateral resolution can be realized through high-resolution printing, often readily available through outside vendors. The designs are drawn clear over a black background and are printed dark-field for a negative-tone photoresist (SU-8,

MicroChem[®]) on a flexible transparency. This transparency is used as a mask for exposure of the photoresist to UV light only in clear areas.

For fabricating the master molds, the following materials are used: 3-inch silicon wafers, tweezers, SU-8, transparency mask with imprinted designs, SU-8 developer (MicroChem[®]), IPA, deionized water, air for drying, 2 (or 3) hot plates, spin-coater (Laurell Technologies[®]), UV light source, and vacuum pump. The steps for fabricating the master molds on silicon wafer are shown in [Figure 1.8](#) and listed below.^{2,4,37}

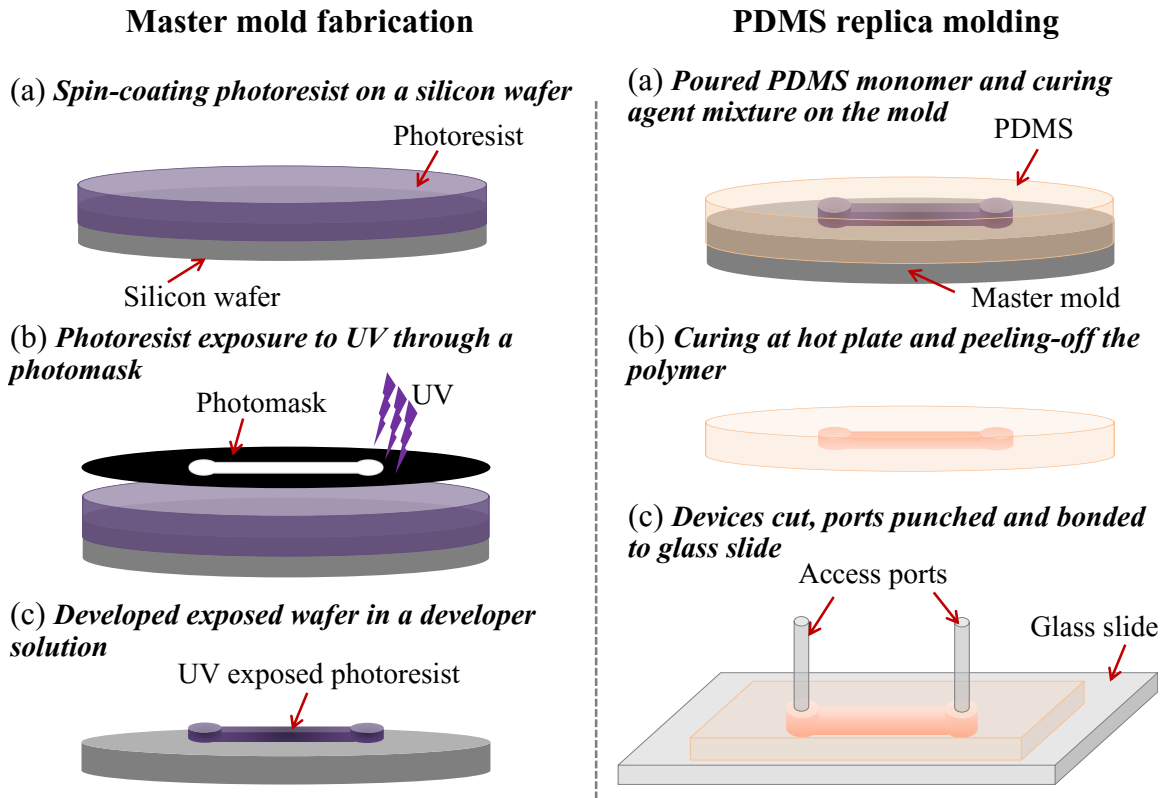


Figure 1.8 Steps of microfluidic device fabrication.

- The wafers are cleaned prior to processing. This is typically done by placing the wafers in a bubbling piranha solution (1:3 sulfuric acid and hydrogen peroxide) for 10 minutes. Wafers are then dehydrated by putting on a hotplate at 200°C for 15

minutes to evaporate any residual humidity followed by cooling down them for next 10 minutes.

- After the wafers are cleaned and dehydrated, the photoresist is spin-coated according to desired height of the devices. The spin speed is summarized in [Table 1.1](#).

Table 1.1 Summary of microfluidic device fabrication steps.

Device height	SU-8 used	Spin speed		Pre-bake exposure time (min)		UV exposure		Post-bake exposure time (min)		Develop (min)	Hard bake at 150°C (min)
		spread cycle	spin cycle	65°C	95°C	Intensity (mJ/cm ²)	time (sec)	65°C	95°C		
30 μm	negative -tone 2-25	500 rpm for 5 s*	1500 rpm for 30 s**	3	7	30	10	1	3	4	7
40 μm	negative -tone 2-25	500 rpm for 5 s*	1000 rpm for 30 s**	5	15	40	10	1	4	6	10
80 μm	negative -tone 2-25	500 rpm for 5 s*	1000 rpm for 25 s** (twice)	7	15	50	10	2	6	10	10

* at 100 rpm/s acceleration ** at an acceleration of 300 rpm/s

- Spin-coated wafer are pre-baked on a hotplate at 65°C followed by baking at 95°C for a specified time. The wafers are then allowed to cool down to room temperature before proceeding to the next step.
- The pre-baked wafers are exposed to UV which allows the crosslinking of SU-8 photoresist. During exposure, a transparency of desired device design is put directly on top of the coated wafer so that the design imprints on the wafer. The ink side of the transparency should be in contact with the wafer.

- Upon exposure, wafers are post-baked on a hotplate at 65°C and 95 °C for the amount of time specified in [Table 1.1](#). The wafers are allowed to cool down to room temperature before proceeding to the development step.
- The wafers are immersed in a glass container with SU-8 developer with a gentle swirling to mix the solution. The developing time depends on the features as well as the film thickness. After the development, wafers are rinsed with IPA and deionized water. After drying with nitrogen gas, wafers are hard-baked on the hot plate at 150°C for the recommended time.

1.3.2 PDMS replication

After the master mold is fabricated, the next step is cast molding ([Figure 1.8](#)).^{2,4} PDMS (Sylgard® 184) pre-polymer is mixed with curing agent in a ratio of 1:10 and poured onto the mold. The curing agent to pre-polymer ratio defines the stiffness of the PDMS after curing. Devices that require softer features can be poured at 1:20, while stiffer PDMS can be accomplished by reducing this ratio up to 1:5. After mixing the curing agent and pre-polymer, the mixture is kept in vacuum to remove air bubbles that can get trapped between the master mold surface and PDMS. Once the mixture is degassed, it is poured onto the master mold and cured at 70°C for ~ 1-2 hours or at room temperature for 12-24 hours. The cured PDMS polymer can now be easily peeled off the master mold. Holes are created in the PDMS polymer for access ports using biopsy punches and sealed to the glass slide/coverslip. Irreversible bonding is achieved by exposing both PDMS and glass surfaces to air plasma that activates Si-O-Si bonds.

1.4 Imaging and device setup

In this section, we discuss the experimental setup used in our microfluidic experiments.^{41,42} After fabricating the microfluidic devices using the protocol mentioned previously, the PDMS chip is mechanically secured to the stage of a stereomicroscope using a scotch tape. A small plastic tube (Tygon[®] microbore tubing (ID = 0.51 mm, OD = 1.52 mm)) is connected to a syringe and the microfluidic device is filled with liquid chemical or buffer. The room temperature is maintained at ~ 23°C as fluctuations in temperature can produce experimental variability and stress in the animals. Single L4-stage worms are picked using a sterile platinum wire pick and dropped into the input port. A small amount of pressure is applied at the input port to push a single worm into each chamber. This protocol of worm handling requires practice and, depending on the specific device geometry, can differ from user to user.

To facilitate real-time imaging of worm movement, we use a Leica[®] MZ16 transmission stereozoom microscope that has a wide field of view (to record multiple chambers) and 35 mm working distance (for fluidic handling). The microscope has 1x and 2x objective lenses that enabled 7.1x to 230x range of magnification, which is adequate for the experiments. The microscope is coupled with a QICam[®] 12-bit Mono Fast 1394 cooled digital camera interfacing with QCapture PRO[®] software. This allowed us to capture digital images (1392 × 1040 pixels) at a specified time interval (typically 1 s). The images from a recorded experiment are sequenced together and compressed into the Audio Video Interleave (.avi) video format. Our laboratory has an external server and several hard-drives to store the recorded videos.

1.5 Worm tracking program

After experiment, the .avi videos are post-processed by our worm tracking program written in the C++ programming language. The program analyzes a large number of images (typically ~ 600-1200) to extract motility parameters such as amplitude, wavelength, forward velocity, path (*i.e.* track) traversed by the worm, track length, number of stops and pauses. The program is adjustable to a range of image-capture speeds (typically up to 40 frames per second) and microscope resolution.

The first step in the worm tracking program is *background subtraction*. Here the program runs through initial 20 consecutive frames of the recorded video to extract static image areas. The background subtraction step is used to negate the channel walls, debris, air bubble and other features except worms in the devices. The Lucas-Kanade optical flow algorithm was used to compute motion vectors of the worm. In addition, the user could ask the program for information about any region of interest (ROI). The ROI specifies the areas of the video that need to be processed further, ignoring the rest. This feature allows the user to ignore irrelevant spots, shorten execution time, and use separate data sets from parallel experiments running at different locations.

The next steps in worm tracking are *worm segmentation and recognition*. After background subtraction, the ROI is processed and polygons are fitted to the moving shapes. Instances where two or more worms are in contact can make the green polygon too large and are discarded. Polygons between consecutive images are then overlapped to provide tracking data over time. The entire body of the worm is represented by an articulated model composed of 13 distinct points connected to form segments running

along its center approximating its posture. Further, the centroid of the worm at each frame is tracked as the worm changes its posture or moves forward and is calculated as the centroid of the fitted polygon (Figure 1.9).

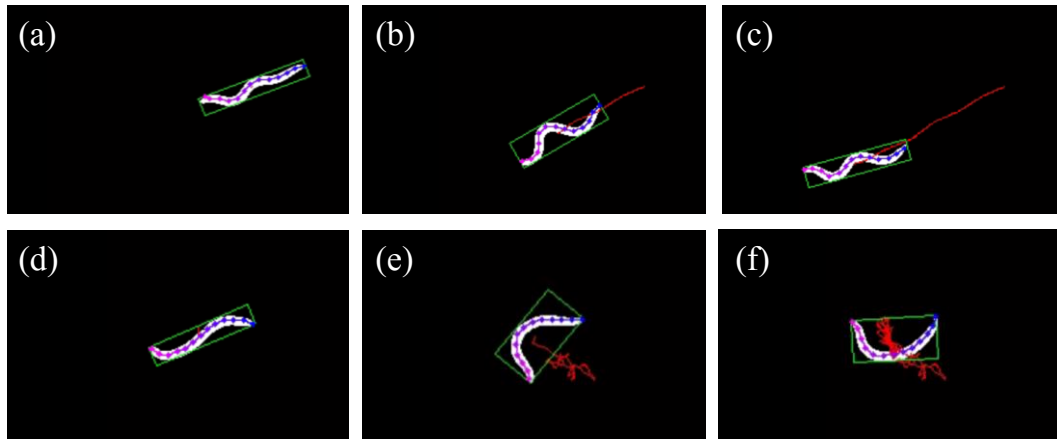


Figure 1.9 Raw greyscale images are processed by our worm tracking software. **(a-c)** During crawling on agarose surface, the body appears to move as a sine-wave with one to one-and-half waves. **(d-e)** During swimming in liquid media, the worm thrashes its body and appears to have one-half sine-wave.

The last step in worm tracking is the *extraction of motility parameters*. The worm-tracking program outputs a Microsoft Excel spreadsheet, post-processed video file, and red track signatures and an .xml file containing the information of 13 body segments as requested by the user. A typical a Microsoft Excel spreadsheet includes the following for every tracked worm: sequential x,y position coordinates, instantaneous velocity, number of stops and reversals, and instantaneous amplitude and wavelength. A custom Graphic User Interface (GUI) program, written in MATLAB[®], further allowed the user to calculate and plot the locomotion parameters from multiple data files. Afterwards, statistical analysis using GraphPad[®] prism and JMP[®] are done to quantify significant differences between data sets and plot the graphical output.

1.6 Thesis Organization

The following chapters are an accumulation of the three published journal papers of which I am the first/primary author.

Chapter 2 illustrates a passive, movement-based assay to observe locomotion behavior of *C. elegans* using sinusoidal microchannels of varying amplitude. A set of locomotion parameters captures the adaptability of a worm's body to navigate through the microchannels, which is then used to screen mutants showing difference in locomotion phenotype. The chapter is modified from the journal paper "Amplitude-modulated sinusoidal microchannels for observing adaptability in *C. elegans* locomotion" published in *Biomicrofluidics*, 5(2), 024112 (2011).

Chapter 3 describes a microfluidic platform, in combination with real-time imaging, to study cyanide toxicity and resistance in *C. elegans*. A multi-parameter analysis method is presented to monitor the effects of the toxicants on wild-type worms, along with the screening of mutants showing varying levels of resistance. This chapter is modified from the journal paper "Multi-parameter behavioral analyses provide insights to mechanism of cyanide resistance in *Caenorhabditis elegans*" published in *Toxicological Sciences*, 135, 156-168 (2013).

Chapter 4 presents an algorithmic search method to find combinations of existing drugs that are more effective at killing *C. elegans* than individual drugs. Starting from the dose response of four commonly used anthelmintics, the winning drug combination is identified through 32 cocktails and has lower concentrations of individual drugs

(compared to their EC_{50} values). The performance of each drug cocktail is quantified by movement parameters analyzed at different points of the experiments.

Chapter 5 demonstrates a microfluidic platform to observe how plant parasitic worms interact with live root systems. Multiple *Arabidopsis* seedlings are cultured in microfluidics, with individual roots housed in separate microchannels. After characterizing root growth parameters, the roots are inoculated with two parasites and observed for subsequent interactions through several days. This chapter is modified from the journal paper “Plant-in-chip: Microfluidic system for studying root growth and pathogenic interactions in *Arabidopsis*” published in Applied Physics Letters, 98, 263703 (2011).

Chapter 6 summarizes the conclusions and future research directions.

1.7 References

1. H. Andersson and A. van den Berg, Sensors and Actuators B: Chemical, 2003, **92**, 315-325.
2. S. K. Sia and G. M. Whitesides, Electrophoresis, 2003, **24**, 3563-3576.
3. G. M. Whitesides, Nature, 2006, **442**, 368-373.
4. Y. N. Xia and G. M. Whitesides, Annual Review of Material Sciences, 1998, **28**, 153-184.
5. D. C. Duffy, J. C. McDonald, O. J. A. Schueller and G. M. Whitesides, Analytical Chemistry, 1998, **70**, 4974-4984.
6. J. C. McDonald, D. C. Duffy, J. R. Anderson, D. T. Chiu, H. Wu, O. J. A. Schueller and G. M. Whitesides, Electrophoresis, 2000, **21**, 27-40.

7. M. A. Unger, H. P. Chou, T. Thorsen, A. Scherer and S. R. Quake, *Science*, 2000, **288**, 113-116.
8. K. Chung, C. A. Rivet, M. L. Kemp and H. Lu, *Analytical Chemistry*, 2011, **83**, 7044-7052.
9. S. X. Guo, F. Bourgeois, T. Chokshi, N. J. Durr, M. A. Hilliard, N. Chronis and A. Ben-Yakar, *Nat Meth*, 2008, **5**, 531-533.
10. J. Qin and A. R. Wheeler, *Lab on a Chip*, 2007, **7**, 186-192.
11. M. F. Yanik, C. B. Rohde and C. Pardo-Martin, *Annual Review of Biomedical Engineering*, 2011, **13**, 185-217.
12. M. Zimmer, J. M. Gray, N. Pokala, A. J. Chang, D. S. Karow, M. A. Marletta, M. L. Hudson, D. B. Morton, N. Chronis and C. I. Bargmann, *Neuron*, 2009, **61**, 865-879.
13. Q. Wen, M. D. Po, E. Hulme, S. Chen, X. Liu, Sen W. Kwok, M. Gershow, Andrew M. Leifer, V. Butler, C. Fang-Yen, T. Kawano, William R. Schafer, G. Whitesides, M. Wyart, Dmitri B. Chklovskii, M. Zhen and Aravinthan D. T. Samuel, *Neuron*, 2012, **76**, 750-761.
14. T. Kaletta and M. O. Hengartner, *Nat Rev Drug Discov*, 2006, **5**, 387-399.
15. E. Bier, *Nature Review Genetics*, 2005, **6**, 9-23.
16. R. Drysdale, in *Drosophila*, ed. C. Dahmann, Humana Press, 2008, **420**, ch. 3, 45-59.
17. G. M. Rubin and E. B. Lewis, *Science*, 2000, **287**, 2216-2218.
18. G. Kari, U. Rodeck and A. P. Dicker, *Clinical Pharmacology & Therapeutics*, 2007, **82**, 70-80.
19. S. Brenner, *Genetics*, 1974, **77**, 71-94.
20. S. H. Chalasani, N. Chronis, M. Tsunozaki, J. M. Gray, D. Ramot, M. B. Goodman and C. I. Bargmann, *Nature*, 2007, **450**, 63-70.
21. N. Chronis, M. Zimmer and C. I. Bargmann, *Nature Methods*, 2007, **4**, 727-731.
22. J. M. Gray, J. J. Hill and C. I. Bargmann, *Proceedings of the National Academy of Sciences*, 2005, **102**, 3184-3191.

23. J. M. Gray, D. S. Karow, H. Lu, A. J. Chang, J. S. Chang, R. E. Ellis, M. A. Marletta and C. I. Bargmann, *Nature*, 2004, **430**, 317-322.
24. A. C. Miller, *Journal of Neuroscience*, 2005, **25**, 3369.
25. O. Hobert, *Journal of Neurobiology*, 2003, **54**, 203-223.
26. D. R. Albrecht and C. I. Bargmann, *Nature Methods*, 2011, **8**, 599-605.
27. M. M. Crane, K. Chung and H. Lu, *Lab on a Chip*, 2009, **9**, 38-40.
28. M. M. Crane, K. Chung, J. Stirman and H. Lu, *Lab on a Chip*, 2010, **10**, 1509-1517.
29. S. R. Lockery, *Nature Methods*, 2007, **4**, 691-692.
30. S. R. Lockery, S. E. Hulme, W. M. Roberts, K. J. Robinson, A. Laromaine, T. H. Lindsay, G. M. Whitesides and J. C. Weeks, *Lab on a Chip*, 2012, **12**, 2211-2220.
31. K. E. McCormick, B. E. Gaertner, M. Sottile, P. C. Phillips and S. R. Lockery, *PLoS ONE*, 2011, **6**, e25710.
32. Y. Zhang, H. Lu and C. I. Bargmann, *Nature*, 2005, **438**, 179-184.
33. T. V. Chokshi, D. Bazopoulou and N. Chronis, *Lab on a Chip*, 2010, **10**, 2758-2763.
34. K. Chung, M. Zhan, J. Srinivasan, P. W. Sternberg, E. Gong, F. C. Schroeder and H. Lu, *Lab on a Chip*, 2011, **11**, 3689-3697.
35. S. E. Hulme, S. S. Shevkoplyas, J. Apfeld, W. Fontana and G. M. Whitesides, *Lab on a Chip*, 2007, **7**, 1515-1523.
36. C. B. Rohde, F. Zeng, R. Gonzalez-Rubio, M. Angel and M. F. Yanik, *Proceedings of the National Academy of Sciences*, 2007, **104**, 13891-13895.
37. A. San-Miguel and H. Lu, *WormBook*, 2013.
38. C. Hu, J. Dillon, J. Kearn, C. Murray, V. O'Connor, L. Holden-Dye and H. Morgan, *PLoS ONE*, 2013, **8**, e64297.
39. J. M. Gray, D. S. Karow, H. Lu, A. J. Chang, J. S. Chang, R. E. Ellis, M. A. Marletta and C. I. Bargmann, *Nature*, 2004, **430**, 317-322.
40. S. R. Lockery, K. J. Lawton, J. C. Doll, S. Faumont, S. M. Coulthard, T. R. Thiele, N. Chronis, K. E. McCormick, M. B. Goodman and B. L. Pruitt, *Journal of Neurophysiology*, 2008, **99**, 3136-3143.

41. J. A. Carr, A. Parashar, R. Gibson, A. P. Robertson, R. J. Martin and S. Pandey, Lab on a Chip, 2011, **11**, 2385-2396.
42. S. Pandey, A. Joseph, R. Lycke and A. Parashar, Advances in Bioscience and Biotechnology, 2011, **2**, 409-415.
43. J. C. Doll, N. Harjee, N. Klejwa, R. Kwon, S. M. Coulthard, B. Petzold, M. B. Goodman and B. L. Pruitt, Lab on a Chip, 2009, **9**, 1449-1454.
44. W. Shi, H. Wen, Y. Lu, Y. Shi, B. Lin and J. Qin, Lab on a Chip, 2010, **10**, 2855-2863.
45. F. Zeng, C. B. Rohde and M. F. Yanik, Lab on a Chip, 2008, **8**, 653-656.
46. J. N. Stirman, M. Brauner, A. Gottschalk and H. Lu, Journal of Neuroscience Methods, 2010, **191**, 90-93.
47. W. Shi, J. Qin, N. Ye and B. Lin, Lab on a Chip, 2008, **8**, 1432-1435.
48. M. Meier, E. M. Lucchetta and R. F. Ismagilov, Lab on a Chip, 2010, **10**, 2147-2153.
49. G. Grossmann, W. J. Guo, D. W. Ehrhardt, W. B. Frommer, R. V. Sit, S. R. Quake and M. Meier, The Plant Cell, 2011, **23**, 4234-4240.

Chapter 2

Amplitude-modulated sinusoidal microchannels for observing adaptability in *C. elegans* locomotion

Modified from a paper published in Biomicrofluidics

Archana Parashar, Roy Lycke, John Carr, Santosh Pandey

2.1 Abstract

In this chapter, we present a movement-based assay to observe adaptability in *C. elegans* locomotion behavior. The assay comprises a series of sinusoidal microchannels with a fixed wavelength and modulating (increasing or decreasing) amplitude. The channel width is comparable to the body width of the organism. Worms are allowed to enter the channel from the input port and migrate towards the output port. Within channel sections that closely match the worm's natural undulations, the worm movement is relatively quick and steady. As the channel amplitude increases or decreases along the device, the worm faces difficulty in generating the propulsive thrust, begins to slow down and eventually fails to move forward. A set of locomotion parameters (i.e. average forward velocity, number and duration of stops, range of contact angle, and cut-off region) is defined for worm locomotion in modulated sinusoidal channels and extracted

from the recorded videos. The device is tested on N2 wild-type *C. elegans* and two mutants (*lev-8* and *unc-38*). We anticipate this passive, movement-based assay can be used to screen nematodes showing difference in locomotion phenotype.

2.2 Introduction

The nematode *C. elegans* is a powerful model organism for behavioral studies primarily because of its fully-mapped genome, relatively simple anatomy, short lifespan and ease of genetic manipulation.¹⁻⁵ Among the varied behavioral facets of *C. elegans*, locomotion is considered the most fundamental and is closely related to the neuromuscular functioning of this limbless animal.⁶⁻¹¹ The forward movement of nematodes results from rhythmic undulatory waves propagating from the head to the tail.^{6,7} These periodic undulations, caused by contraction and relaxation of body muscles, have helped quantify *C. elegans* locomotion on various substrates (e.g. agar plates,⁷ gelatin,¹¹ saturated particulates^{8,9} and buffer¹¹). The shape and speed of undulations depend on the response of the *C. elegans* to the physical environment – they crawl on agarose surface with undulations of low frequency and smaller wavelength; they swim in M9 buffer with undulations of higher frequency and longer wavelength.^{7,11}

With advances in microfluidic technology,¹² a new class of worm assays (T-mazes for memory and learning,¹³ culture and detection chambers,^{3,5} micro-clamps for olfactory sensing,¹⁴ integrated microscopy system for rapid phenotyping,¹⁵ piezoresistive displacement clamps for force measurement,¹⁶ compact discs for geotaxis studies,¹⁷ micro-traps for nanosurgery,¹⁸ and screening and sorting devices¹⁹⁻²¹) have emerged to study the mechanics and neuromuscular functioning of *C. elegans*. Particularly relevant

to this work are microfluidic devices^{8,9,22} that allow the observation of *C. elegans* locomotion in soil-like environments (compared to that on planar surfaces^{7,11}). One such example is the waveform generator²² consisting of sinusoidal channels (each of a fixed amplitude and wavelength) to experimentally control the waveform and trajectory of crawling worms. It was shown that, in the waveform generator, wild-type were able to pass through several different channels, suggesting that the mechanisms for generating and propagating undulations were largely independent of the channel amplitude and wavelength.²² The worms, however, faced difficulty in passing through sinusoidal channels whose amplitude and wavelength were larger (2 times or more) than the dimensions of its natural undulatory movement.²² In a different work, we used straight channels to show significant differences in the morphological and locomotion parameters between parasitic nematodes (*Oesophagostomum dentatum*), reflecting a difference in propulsive thrust between mutants.²⁴

In this study, we build on the above concepts of a waveform generator and differences in morphological/locomotion parameters among mutants to realize a simple tool for screening *C. elegans* by differentiating its ability to adapt to sinusoidal channels with controlled waveform. Here, the entire locomotion experiment is conducted in two *modulated* sinusoidal channels; one with gradually increasing amplitude and the other with gradually decreasing amplitude. We observed that worms moved steadily and vigorously through channel sections whose amplitude and wavelength closely matched that of the worm's natural undulations. Beyond this *adaptable range*, the worms found it difficult to move forward and eventually stopped. This enabled us to quantify

locomotion in modulated sinusoidal channels by a set of parameters (average forward velocity, number and duration of stops, and cut-off region). We tested the device on wild-type and two mutants (*lev-8* and *unc-38*) and observed differences in their crawling behavior. A custom worm tracking software was used to visually observe the tracks of worms with the possibility of automated data extraction from recorded videos. The system overview and design of the proposed microfluidic device is shown in [Figure 2.1](#).

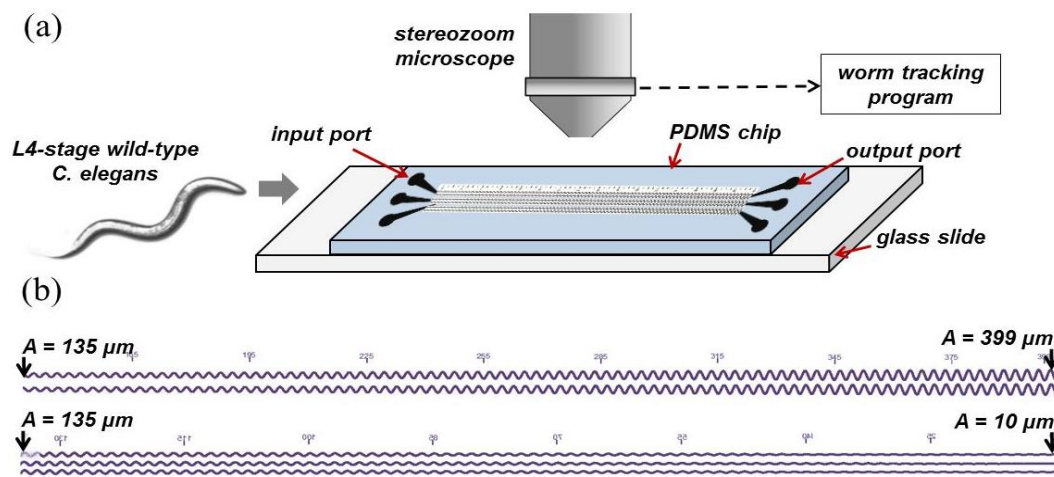


Figure 2.1 Overview of the system and device design. **(a)** Experimental setup comprising a microfluidic chip with sinusoidal channels, high-resolution microscope, and worm tracking program. **(b)** Magnified images of the two (i.e., with increasing and decreasing amplitude) modulated sinusoidal channels with vertical markers.

2.3 Materials and Methods

2.3.1 *C. elegans* strains and culture

Wild-type (N2) and mutants (CB904 [*unc-38(e264)*] and ZZ15 [*lev-8(x15)*]) worms are obtained from the Caenorhabditis Genetics Center (CGC) at University of Minnesota (St. Paul, USA). The worms are cultivated at 25°C on NGM plates seeded with *Escherichia coli* OP50 bacteria. For the experiments, L4-stage *C. elegans* are

picked using a sterilized platinum wire. A polyethylene tubing (OD = 1 mm, ID = 0.58 mm) is connected to a 1-mL syringe and the sinusoidal channels are filled with standard M9 buffer. Care is taken to ensure that the input ports and channels do not trap any air bubbles. During our initial trials, we noticed that air bubbles would block the path of worms which end up clogging the channels. Thereafter, L4-stage *C. elegans* are dropped onto the input ports.

2.3.2 Experimental setup

The experimental setup is shown in [Figure 2.1](#). Two microchannels were designed: the first comprises an amplitude A that increases from 135 μm to 399 μm in steps of 6 μm ; the second has amplitude A decreasing from 135 μm to 10 μm in steps of 3 μm . For both microchannels, an input port is placed at $A = 135 \mu\text{m}$ and an output port is placed at $A = 10 \mu\text{m}$ or at $A = 399 \mu\text{m}$. The channel wavelength (λ) is fixed at 360 μm . The channel width (60 μm) and height (80 μm) are chosen to allow sinusoidal movement of crawling worms but with limited latitudinal and longitudinal freedom, as discussed for the waveform generator.²² In every chip, multiple (8-12) modulated sinusoidal channels are placed in parallel to record several worms at the same field of view. The devices are fabricated using the steps mentioned in Section 1.3.

2.3.3 Worm manipulation and imaging

In our experiments, the worms were allowed to enter the sinusoidal channels without applying any attractants (e.g. food source^{1,13}), deterrents (e.g. citric acid) or mechanical forces^{15,18}. Previous work used a syringe to apply suction to push the worms

into the sinusoidal channels.²² In our devices, we observed that suction sometimes caused temporary immobilization of the worm and the organism needed time to resume with its forward movement. As an alternate method of inserting the worms, we found that electrotaxis can help direct the worms into the modulated channel (anode at input port, cathode at output port). This is consistent with the current literature that shows nematodes with developed electrosensory neurons respond to applied electric fields.^{25,26} However, for our experiments, we preferred not to use any external electrical, chemical or mechanical factors which may affect the measured locomotion parameters.

After a brief scouting time (~ 3-5 minutes), worms enter the channels and move towards the output port. A Leica MZ16 stereomicroscope is used to record the worms' motility along the different channel sections as shown in [Figure 2.2](#). The .avi video is post-processed by a worm tracking program (Section 1.5) that extracts track signatures and locomotion parameters of individual and/or multiple worms.

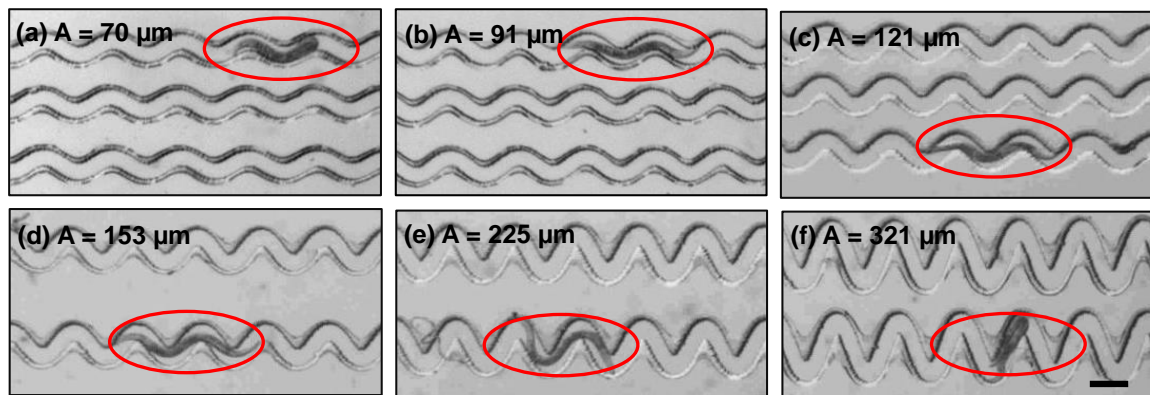


Figure 2.2 Wild-type *C. elegans* (encircled) crawling in different sections of a modulated sinusoidal channel. The worm shows relatively smooth movement in the adaptable range of channel amplitudes (**b-e**). In sections beyond this adaptable range (**a, f**) the worm is unable to move forward.

A set of locomotion parameters are extracted as: (i) *Average forward velocity*: This is the ratio of the net body displacement to the total time traversed in a given channel section. (ii) *Stops*: We define a stop as a halt (net body displacement less than one channel wavelength) for time duration more than or equal to 3 seconds. (iii) *Range of contact angle*: The worm makes contact with and pushes against the channel sidewall to move forward. The range of contact angle is defined as the angle within which the body touches the sidewall. (iv) *Cut-off region*: The cut-off region is defined as the region where a worm appears virtually immobilized (net body displacement less than one channel wavelength) for time duration greater than 300 seconds.

2.4 Results

2.4.1 Average forward velocity

Figure 2.3 plots the average forward velocity of *C. elegans* (wild-type, *lev-8* and *unc-38*) as a function of the channel's amplitude.

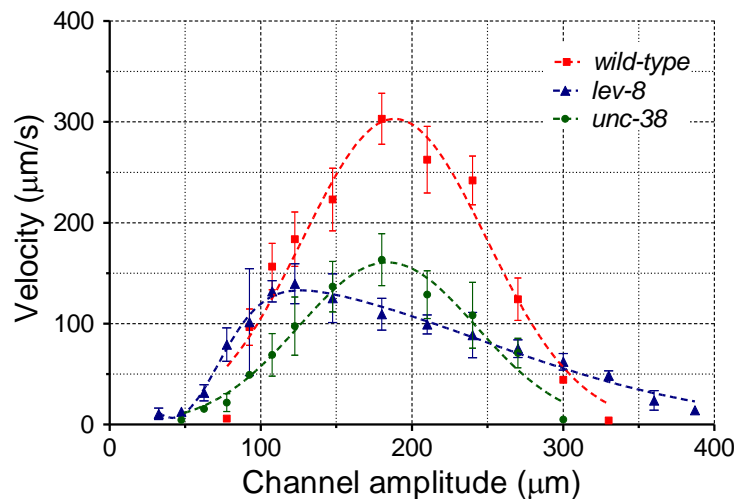


Figure 2.3 Average forward velocity versus channel amplitude is plotted for the three L4-stage *C. elegans* strains: *wild-type*, *lev-8* and *unc-38*.

For each strain, the velocity curve has a peak ($303 \pm 25 \mu\text{m/s}$ for wild-type, $140 \pm 20 \mu\text{m/s}$ for *lev-8*, and $163 \pm 26 \mu\text{m/s}$ for *unc-38*; mean \pm S.E.) at a certain amplitude ($180 \mu\text{m}$ for wild-type, $123 \mu\text{m}$ for *lev-8*, and $180 \mu\text{m}$ for *unc-38*, $n = 15-20$, $N = 3$) and decays on either side of this amplitude. On either side of the peak amplitude, the worm has to acclimatize its body posture along the channel geometry to push forward. This increases the time needed to traverse a certain displacement, which in turn lowers the average forward velocity. Further, the velocity curves for wild-type and *unc-38* are symmetrical on either side of their peak values. The *lev-8* mutant, however, shows a prolonged and gradual decrease in velocity at higher channel amplitudes while having a sharp drop at lower channel amplitudes. This suggests that, at amplitudes above $100 \mu\text{m}$, the *lev-8* mutant is able to adapt itself better than wild-type and *unc-38* mutant with a finite forward velocity up to channel amplitudes of $390 \mu\text{m}$.

In an attempt to correlate the location of peak forward velocity in the modulated sinusoidal channel with the natural undulations of the worms, we measured the amplitude, wavelength and velocity of *C. elegans* crawling on 2.5% agarose plates without any food (Figure 2.4). The A/λ ratio for the three strains ($n = 12-15$) on agarose plates are: $A/\lambda = 0.46$ for wild-type, $A/\lambda = 0.33$ for *lev-8*, and $A/\lambda = 0.54$ for *unc-38*. From Figure 2.3, the peak velocities occur at channel regions where $A/\lambda = 0.50$ for wild-type, $A/\lambda = 0.34$ for *lev-8*, and $A/\lambda = 0.50$ for *unc-38*. It thus seems likely that the peak velocity in modulated sinusoidal channel occurs at an amplitude where the channel A/λ ratio closely matches the A/λ ratio of worm's natural undulations on agarose plates. Furthermore, the peak velocities for individual strains in the sinusoidal channels (Figure

2.3) are in close agreement with the forward velocities measured on agarose plates (Figure 2.4). This suggests that, at these channel regions, the worms crawl as comfortably as they would on agarose culture plates.

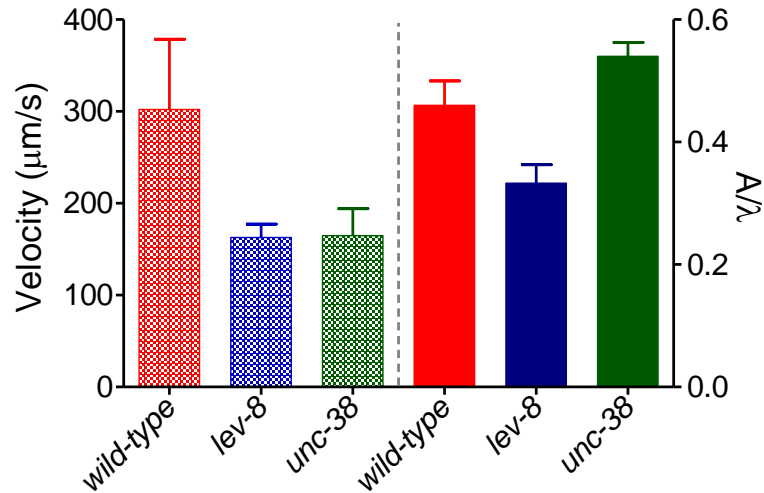


Figure 2.4 Average forward velocity and ratio of amplitude to wavelength (A/λ) for the three *C. elegans* strains on 2.5% agarose plates are shown.

2.4.2 Number and duration of stops

Figure 2.5 shows the number and duration of stops exhibited by wild-type, *lev-8* and *unc-38* worms during their forward movement in modulated sinusoidal channels.

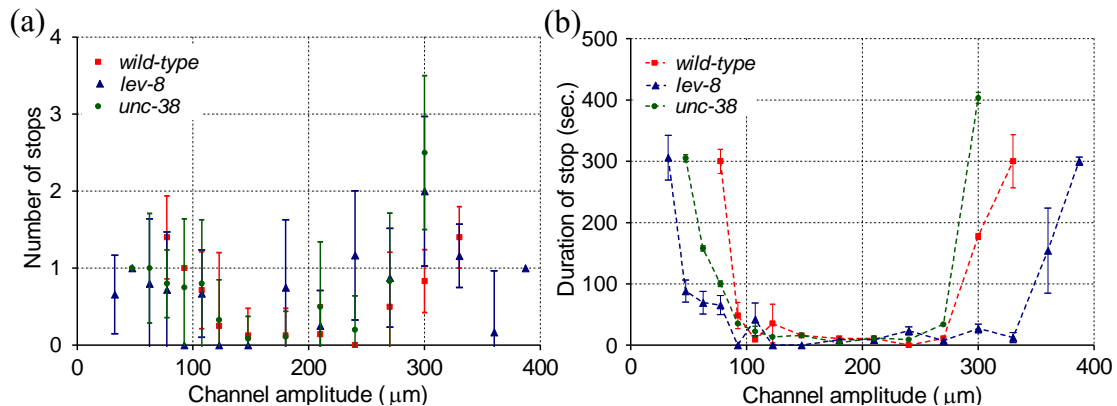


Figure 2.5 Average number (a) and duration (b) of stops versus channel amplitude are plotted for the three *C. elegans* strains (*wild-type*, *lev-8* and *unc-38*).

In the adaptable range (100 μm - 250 μm), all three strains stop less frequently (< 1.4 times) and for a short duration ($t < 35$ seconds). As the channel amplitude increases or decreases beyond this adaptable range, the duration and average number of stops increase significantly (~ 300 seconds and > 1.4 times, respectively). Unlike the Gaussian decay observed in average velocity (Figure 2.3), the duration of stops increases sharply as the worm encounters the channel section close to its cut-off region. A small stop duration ($t < 25$ seconds) is shown by *lev-8* over a wider amplitude range (50 μm - 345 μm) when compared to wild-type (100 μm - 300 μm) and *unc-38* (140 μm - 285 μm). This again shows that *lev-8* is better than wild-type and *unc-38* at showing steady movement over a wider range of channel amplitudes.

2.4.3 Range of contact angle

During its forward movement, the worm makes contact with the channel sidewall to overcome friction and generate the propulsive thrust. We measured the range of contact angle at different sections of the sinusoidal channel (Figure 2.6).

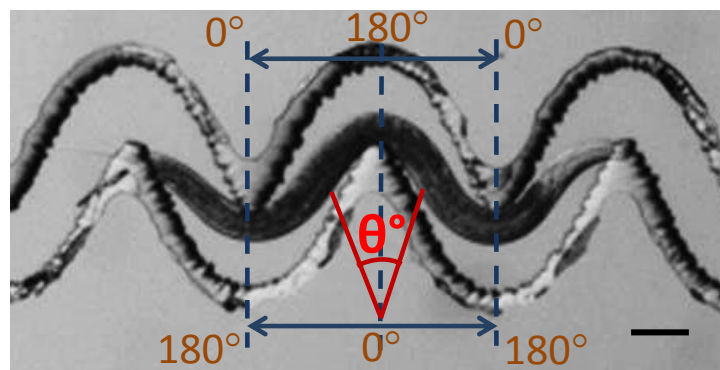


Figure 2.6 Illustration of the range of contact angle for a L4-stage wild-type worms in two sections of the modulated sinusoidal channel.

We observed that the worms made less contact ($\theta < 170^\circ$) with the channel sidewalls in the adaptable range of amplitudes (100 μm - 250 μm) while increased their range of contact angle in regions of difficulty. Compared to wild-type and *lev-8*, the *unc-38* mutant has a larger range of contact angle ($\theta > 170^\circ$) throughout the amplitude range which is probably due to its uncoordinated movement pattern (Figure 2.7). The wild-type has the smallest range of contact angle among the three strains for the entire distance of the channel. At amplitudes outside the adaptable range, most of the body for *unc-38* and *lev-8* mutants touches the channel sidewalls ($\theta > 300^\circ$) compared to wild-type that has a maximum range of contact angle of $\sim 200^\circ \pm 5^\circ$ (mean \pm S.E.).

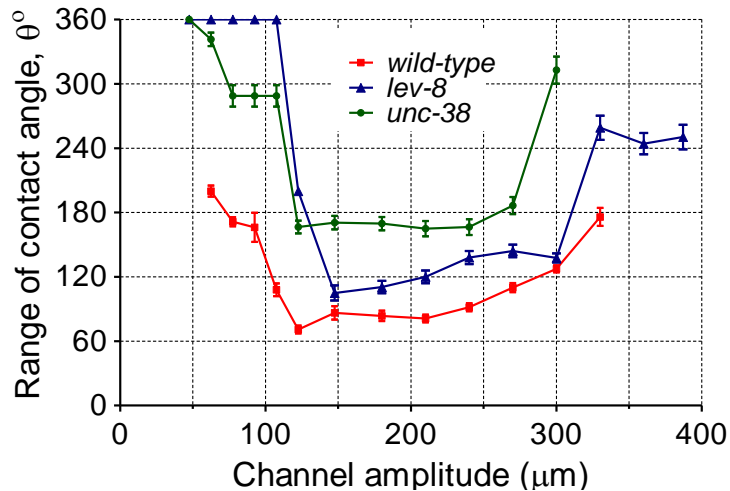


Figure 2.7 Range of contact angle versus channel amplitude is plotted for the L4-stage *C. elegans* (wild-type, *lev-8* and *unc-38*).

2.4.4 Cut-off region

The cut-off region in the lower amplitude range and higher amplitude range are measured for the wild-type, *lev-8* and *unc-38* *C. elegans*. The lower cut-off for the individual strains are $79 \pm 7 \mu\text{m}$ for wild-type, $31 \pm 8 \mu\text{m}$ for *lev-8*, and $44 \pm 8 \mu\text{m}$ for

unc-38 (mean \pm S.E., $n = 15-20$, $N > 3$). Unlike *lev-8* or *unc-38* mutants, the wild-type worm is unable to move beyond a channel amplitude less than 70 μm (Figure 2.8).

It is easier for *lev-8* and *unc-38* to adapt their body posture and continue moving to sections of lower amplitudes ($< 40 \mu\text{m}$). The upper cut-off for the individual strains are $323 \pm 14 \mu\text{m}$ for wild-type, $390 \pm 14 \mu\text{m}$ for *lev-8*, and $279 \pm 16 \mu\text{m}$ for *unc-38* (mean \pm S.E., $n = 15-20$, $N > 3$). In accordance with earlier results, *lev-8* has the farthest cut-off region among the three strains.

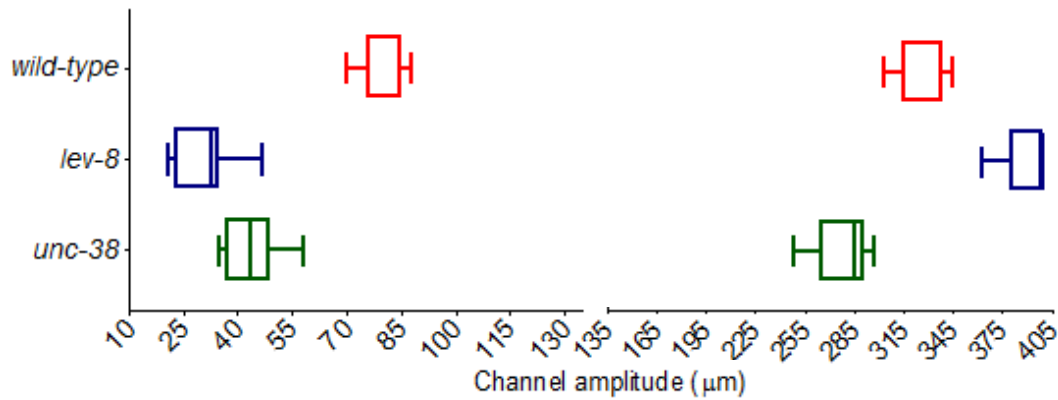


Figure 2.8 The lower and upper cut-off regions in the modulated sinusoidal channels are shown for the *wild-type*, *lev-8* and *unc-38* *C. elegans*.

The recorded videos are processed by a custom worm tracking program to obtain locations of the body centroid as a function of time. This is used to plot the path traversed (i.e. tracks) by individual worms in the modulated sinusoidal channels. As shown in Figure 2.9a, the worm tracking program converts the recorded grayscale video to black and white, identifies the worm body, measures its centroid location, and plots the tracks over a period of time. Figure 2.9b shows representative tracks of wild-type, *lev-8* and *unc-38* *C. elegans* along sections of the sinusoidal channel. Each channel section denotes a different level of difficulty for the worms. A somewhat linear track

indicates smooth movement of the worm, while a zigzag track denotes increasing difficulty for the worm to continue its forward movement. This visual observation of the worm movement provides a quick means of observing the worm difficulty and complements the previous quantitative analysis (Figure 2.3-2.6).

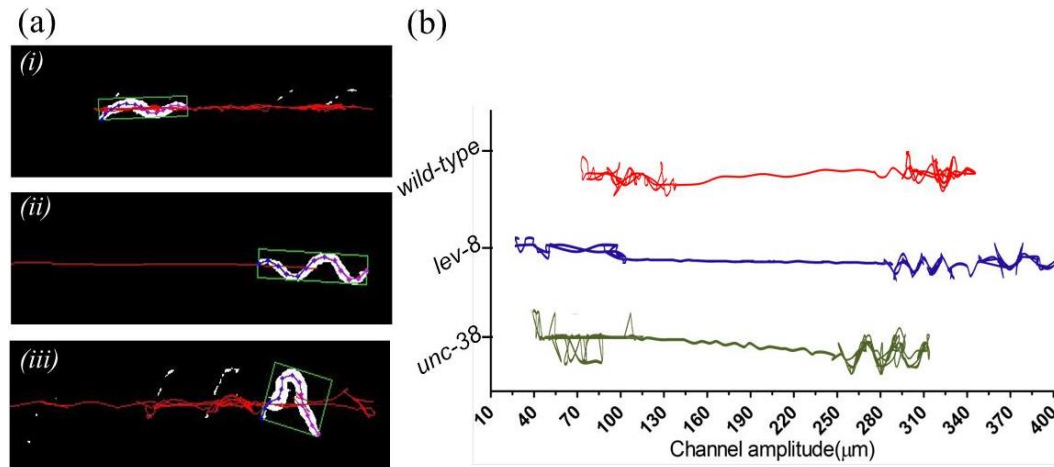


Figure 2.9 Image analysis using worm tracking program. **(a)** Snapshots of a L4-stage wild-type *C. elegans* are shown whose body positions and centroid are extracted. The tracks show the relative levels of difficulty faced by the worm in the different sections of the channel. [(i): lower cut-off region, (ii): adaptable region, and (iii): higher cut-off region²⁹] **(b)** Representative tracks of the body centroid for *C. elegans* along the modulated sinusoidal channel.

2.5 Discussion

For quite some time, it is known that the form and frequency of the waves passing down a nematode's body depends, among other factors, on the relative resistance exerted by the medium on the normal and tangential components of displacement.^{6,11} While tangential forces exerted by the medium retard its motion, the normal forces (or internally generated bending couples) generated by the nematode propels the body forward.^{6,7} When observed in straight microfluidic channels with relatively no physical constraints (besides the channel sidewalls separated by 300 μm),

body and locomotion parameters (amplitude, wavelength, frequency, average forward velocity) can be measured along the channel.^{24,25} The locomotion parameters were used to calculate the propulsive thrust, which is relatively distinct for a nematode species or isolate under the same set of experimental conditions.²⁴ From this, we hypothesized that the propulsive thrust and adaptability of *C. elegans* could be tested in modulated sinusoidal channels of varying amplitude. This allowed us to manipulate the natural undulations by forcing the worm to conform its body to the shape of the sinusoidal channel during its forward movement. As the channel width was comparable to the width of its body, the worm pushed against regions of the channel sidewalls to propel itself forward. The gradual change in channel amplitude necessitated the worm to adjust its locomotory behavior. Both UNC-38 and LEV-8 are essential subunits of the body wall muscle acetylcholine receptors.²⁷ This explains why both mutants (*unc-38* and *lev-8*) have a lower peak forward velocity compared to wild-type in the sinusoidal channels (Figure 2.3). The *unc-38* mutant, known to display uncoordinated movement, shows a larger range of contact angle (Figure 2.7) and a smaller cut-off region at the high A -limit (Figure 2.8) compared to the wild-type worm. It is interesting to observe that *lev-8* is able to cover the widest range of channel amplitudes, even though with significant difficulty close to its cut-off regions in the device. Previously, it was demonstrated that *lev-8* gene is also expressed in the GABAergic neurons innervating the body wall muscles and helps control the relaxation of dorsal muscles during wave oscillations.²⁷ This explains the smaller A/λ ratio of *lev-8* compared to wild-type in both sinusoidal channels and 2.5% agarose plates (Figure 2.4). The greater flexibility in body posture for

lev-8 demonstrated in our experiments suggests the possible role of other biological factors in regulating worm adaptation for crawling in constrained microenvironments.

The proposed study builds upon the previous work on waveform generator²² in three main ways: (i) *Increased throughput*: The waveform generator tested the crawling behavior in six individual fixed-wave channels (18 different A/λ ratio). Here, two modulated sinusoidal channels allowed us to observe crawling behavior through several (more than 80 different A/λ ratio) changing waveforms. For example, the modulated sinusoidal channel with increasing amplitude accommodates $(399-135)/6 = 44$ distinct waveforms. This helps to significantly increase the throughput of the locomotion experiments. (ii) *Quantifying locomotion*: The waveform generator was separated in three domains (i.e. green, blue, red) depending on the relative ease with which the worm can crawl through. In the modulated sinusoidal channels, we defined a set of locomotion parameters to better quantify the relative ease of worm crawling. (iii) *Testing mutants*: While the waveform generator was tested with wild-type worm to show the feasibility of controlling the crawling behavior, the modulated sinusoidal channels was studied with three *C. elegans* strains to show differences in crawling behavior between mutants.

The observed differences in locomotion parameters in the modulated sinusoidal channels can be used to differentiate mutant phenotypes. Compared to existing *C. elegans* screening methods, the movement-based assay presented here has some potential benefits. First, the method does not require any on-chip immobilization techniques (such as suction or cooling)^{14,15,18} which makes the device simple to use and requires a single mask fabrication process. Second, the worm is not subjected to external

factors (such as mechanical or chemical stress)^{1,14} that may physically harm or produce unknown behavioral changes in the organism. The worm is allowed to move freely through the sinusoidal channel and use its innate internal forces for the forward locomotion. Third, unlike observing single worms one at a time,¹⁴ parallel observation of individual worms in multiple modulated sinusoidal channels is possible. Since the input/output ports are accessible to the user, it is possible to add chemical compounds (e.g. anthelmintics) in individual channels and test their effects on worm locomotion at real-time.²⁴ Furthermore, the existing modulated sinusoidal channels could be used to test other *C. elegans* mutants (such as *cat-2*, *cat-4*, *sqt-1*, *lon-1*, *unc-54* and *goa-1*)⁷ without changing the device dimensions. This is because most mutants, studied on agarose plates, have similar body postures (e.g. $A/\lambda = 90/540$ for *goa-1* to $130/480$ for *unc-54*)⁷ and their forward velocities ($220 \pm 50 \mu\text{m/s}$ for *goa-1* to $40 \pm 10 \mu\text{m/s}$ for *unc-54*)⁷ are in the range that can be observed in our movement-based assay.

The *treadmill test* in modulated sinusoidal channels provides an advantage of limiting the area of experimental observation within the microscope's field of view, while measuring the locomotion adaptability in *C. elegans*. Behavioral intelligence has been suggested in previous studies where the worms adapted to range of physical^{8,11-14} and biochemical¹⁻⁵ environments. For example, these animals can migrate over a long distance on agarose plates in search of food or other attractants. This makes it difficult to predict or measure worm locomotion, characterized by frequent forward crawling, reverse crawling and omega turns,²² on agarose plates across a wide spatial area. Additionally, it is challenging to design constrained microenvironments on agarose

plates to observe locomotion adaptability. The modulated sinusoidal channel design provides directed path for the worm to move and makes relatively easier to measure changing locomotion parameters. The measured average velocity accounted for the forward/reverse crawling and the stops during forward movement. The cut-off region indicated the upper limit of propulsive force generated by the worm.

2.6 Conclusion

In this study, we inserted the *C. elegans* into sinusoidal channels of a width comparable to the nematode's body width. While the wavelength of the sinusoidal channel was fixed, its amplitude kept gradually increasing (or decreasing). The restricted channel geometry forced the worms to constantly adapt its locomotory behavior during its forward movement. The modulated sinusoidal channel design thus manipulated the propulsive thrust exerted by the worm as reflected by a set of locomotion parameters. The wild-type worm had a significantly higher peak forward velocity compared to *lev-8* and *unc-38* mutants. The *lev-8* worm was able to cover a wider range of channel amplitudes. The *unc-38* worm traverses the smallest range of increasing channel amplitudes. This passive device does not require any movable parts and allows real-time imaging of locomotion adaptability. The modulated sinusoidal channels are expected to provide a simple platform to automatically identify differences in *C. elegans* locomotion.

2.7 References

1. A. C. Miller, T. R. Thiele, S. Faumont, M. L. Moravec, and S. R. Lockery, *Journal of Neurosciences*, 2005, **25**, 3369–3378.
2. J. M. Gray, J. J. Hill, and C. I. Bargmann, *Proceeding of National Academy of Sciences*, 2005, **102**, 3184–3191.
3. N. Chronis, M. Zimmer, and C. I. Bargmann, *Nature Methods*, 2007, **4**, 727–731.
4. S. H. Chalasani, N. Chronis, M. Tsunozaki, J. M. Gray, D. Ramot, M. B. Goodman, and C. I. Bargmann, *Nature*, 2007, **450**, 63–70.
5. J. M. Gray, D. S. Karow, H. Lu, A. J. Chang, J. S. Chang, R. E. Ellis, M. A. Marletta, and C. I. Bargmann, *Nature*, 2004, **430**, 317–322.
6. J. Gray and H. S. Lissmann, *Journal of Experimental Biology*, 1964, **41**, 135–154.
7. J. Karbowski, C. Cronin, A. Seah, J. Mendel, D. Cleary, and P. Sternberg, *Journal of Theoretical Biology*, 2006, **242**, 652–669.
8. S. Jung, *Physics of Fluids*, 2010, **22**, 031903.
9. G. Juarez, K. Lu, J. Sznitman, and P. Arratia, *Europhysics Letters*, 2010, **92**, 44002.
10. J. Sznitman, P. Purohit, P. Krajacic, T. Lamitina, and P. E. Arratia, *Biophysical Journal*, 2010, **98**, 617–626.
11. C. Fang-Yen, M. Wyart, J. Xie, R. Kawai, T. Kodger, S. Chen, Q. Wen, and A. Samuel, *Proceeding of National Academy of Sciences*, 2010, **47**, 20323–20328.
12. G. M. Whitesides, *Nature*, 2006, **442**, 368–373.
13. J. Qin and A. R. Wheeler, *Lab on a Chip*, 2007, **7**, 186–192.
14. Y. Zhang, H. Lu, and C. I. Bargmann, *Nature*, 2005, **438**, 179–184.
15. K. Chung, M. M. Crane, and H. Lu, *Nature Methods*, 2008, **5**, 637–643.
16. S. J. Park, M. B. Goodman, and B. L. Pruitt, *Proceeding of National Academy of Sciences*, 2007, **104**, 17376.

17. K. Nahui, C. M. Dempsey, J. V. Zoval, J. Sze, and M. J. Madou, *Sensors Actuators B*, 2007, **122**, 511–518.
18. C. B. Rohde, F. Zeng, R. Gonzalez-Rubio, M. Angel, and M. F. Yanik, *Proceeding of National Academy of Sciences*, 2007, **104**, 13891–13895.
19. M. Crane, K. Chung, J. Stirman, and H. Lu, *Lab on a Chip*, 2010, **10**, 1509–1517.
20. N. Chronis, *Lab on a Chip*, 2010, **10**, 432-437.
21. T. V. Chokshi, A. Ben-Yakar, and N. Chronis, *Lab on a Chip*, 2009, **9**, 151-157.
22. S. R. Lockery, K. J. Lawton, J. C. Doll, S. Faumont, and S. M. Coulthard, *Journal of Neurophysiology*, 2008, **99**, 3136–3143.
23. J. Carr, A. Parashar, R. Gibson, A. Robertson, R. J. Martin, and S. Pandey, *Lab on Chip*, 2011, **11**, 2385-2396.
24. B. Chen, A. Deutmeyer, J. Carr, A. P. Robertson, R. J. Martin, and S. Pandey, *Parasitology*, 2011, **138**, 80–88.
25. C. V. Gabel, H. Gabel, D. Pavlichin, A. Kao, D. Clark, and A. Samuel, *Journal of Neurosciences*, 2007, **27**, 7586-7596.
26. P. Rezai, A. Siddiqui, P. Selvaganapathy, and B. Gupta, *Lab on a Chip*, 2010, **10**, 220.
27. P. R. Towers, B. Edwards, J. E. Richmond, and D. B. Sattelle, *Journal of Neurochemistry*, 2005, **93**, 1-9.

Chapter 3

Multi-parameter behavioral analyses provide insights to mechanism of cyanide resistance in *Caenorhabditis elegans*

Modified from a paper published in Toxicological Sciences

Archana Parashar[‡], Jenifer Saldanha[‡], Santosh Pandey, Jo Anne Powell-Coffman
[‡] first authors.

3.1 Abstract

Environmental toxicants influence development, behavior, and ultimately survival. The nematode *Caenorhabditis elegans* has proven to be an exceptionally powerful model for toxicological studies. Here, we develop novel technologies to describe the effects of cyanide toxicity with high spatiotemporal resolution. Importantly, we use these methods to examine the genetic underpinnings of cyanide resistance. *C. elegans* that lack the EGL-9 oxygen sensing enzyme have been shown to be resistant to hydrogen cyanide (HCN) gas produced by the pathogen *Pseudomonas aeruginosa* PAO1. We demonstrate that the cyanide resistance exhibited by *egl-9* mutants is completely dependent on the HIF-1 hypoxia inducible factor and is mediated by the *cysl-2* cysteine synthase, which likely functions in metabolic pathways that inactivate cyanide. Further, the expression of *cysl-2* correlates with the degree of cyanide

resistance exhibited in each genetic background. We find that each mutant exhibits similar relative resistance to HCN gas on plates or to aqueous potassium cyanide (KCN) in microfluidic chambers. The design of the microfluidic devices, in combination with real-time imaging, addresses a series of challenges presented by mutant phenotypes and by the chemical nature of the toxicant. The microfluidic assay produces a set of behavioral parameters with increased resolution that describe cyanide toxicity and resistance in *C. elegans*, and this is particularly useful in analyzing subtle phenotypes. These multiparameter analyses of *C. elegans* behavior hold great potential as a means to monitor the effects of toxicants or chemical interventions in real time and to study the biological networks that underpin toxicant resistance.

3.2 Introduction

The free-living nematode *C. elegans* has proven to be an excellent model for studying the mechanisms by which animals respond to environmental signals or toxicants.^{1,23,39} Advantages include a fully sequenced genome, genetic tractability, extensive knowledge of its development and anatomy and ease of culture.⁵ Behavioral analyses of *C. elegans* can be employed to assess fast acting toxicants or pharmacological treatments that cause uncoordinated movement or paralysis. The combination of genetics and in-depth analyses of toxicant effects provide important insights to the mechanisms by which toxicants or pollutants impair animal function.

There are technical challenges to assaying the effects of fast-acting aqueous toxicants. In the laboratory, *C. elegans* are usually cultured on agarose plates with

bacterial food. If animals are placed in a liquid droplet, they thrash and are difficult to image. Microfluidic devices resolve this by maintaining the animals in a single plane of focus, but animals often seek to escape chambers containing poisonous substances. To overcome these obstacles, we designed a chamber that allows mechanical insertion of individuals. We also engineered a custom port design that permits worm entry but prevents exit. Additional design modifications enable real-time imaging and chemical testing with applications for mutants that behave unpredictably in the presence of in electric fields, agarose gel or toxicants.

Among the toxicants in our environment, cyanide is an especially potent poison.^{2,7,17} It is produced as a by-product of many industrial processes, chemical reactions and even fires.¹⁸ Cyanide exerts its toxic effects by irreversibly binding to iron, thereby incapacitating proteins required for aerobic respiration and ultimately causing cellular asphyxiation and death.² Several bacteria, including the nearly ubiquitous human pathogen *Pseudomonas aeruginosa*, produce cyanide,⁴ and this is especially devastating to patients with compromised respiratory or immune systems.

C. elegans lacking a functional *egl-9* gene have been shown to be resistant to HCN gas produced by the pathogen *P. aeruginosa* PAO1.^{13,17,35} This is especially intriguing because the EGL-9 protein functions as a cellular oxygen sensor. EGL-9 hydroxylates the HIF-1 hypoxia-inducible factor using oxygen as a co-substrate, and this modification targets HIF-1 for degradation.¹⁶ The HIF-1 transcription factor controls changes in gene expression that allow animals to adapt to oxygen deprivation.^{20,36} Loss-of-function mutations in the *C. elegans egl-9* gene cause HIF-1 to be expressed at high

levels and to be over-active.^{3,16,37} This, in turn, impacts *C. elegans* development, stress response, longevity, and behavior.²⁹ How does a loss-of-function mutation in *egl-9* and the accompanying over-activation of HIF-1 protect *C. elegans* from cyanide toxicity? To address this question, we examined the roles of *egl-9*, *hif-1* and the *cysl-2* cysteine synthase gene in cyanide resistance, employing both HCN gas assays and real-time imaging in a custom microfluidic device to describe multiple parameters of these behavioral phenotypes. These experiments confirmed that mutations that confer resistance to the paralyzing effects of HCN gas also protect *C. elegans* from KCN in the microfluidic chambers, and they illuminate the mechanisms that protect *egl-9* mutant worms from cyanide toxicity. We further explored and verified the broader applicability of our microfluidic device, using the anthelmintic drug levamisole. The combination of microfluidics and automated imaging increases the power of *C. elegans* as a genetic model system to study the effects of toxicants or chemical interventions in real time.

3.3 Materials and Methods

3.3.1 *C. elegans* strains and culture

C. elegans strains were grown at 20°C, on standard NGM agarose plates with *Escherichia coli* OP50 bacterial food, as previously described.⁵ All experiments were performed at 20 – 22°C using L4-stage worms. The following strains were used in this study: N2 wild-type, JT307 [*egl-9(sa307)*], ZG448 *iaIs07[Pnhr-57::gfp unc-119 (+)] IV; egl-9 (ia60) V*, ZG493 *iaIs07[Pnhr-57::gfp unc-119 (+)] IV; egl-9 (sa330) V*, ZG347 *iaIs07[Pnhr-57::gfp unc-119 (+)] IV; egl-9 (sa307) hif-1(ia04) V*, ZG175 *iaIs07[Pnhr-57::gfp unc-119 (+)] IV; hif-1(ia04) V*. The *egl-9(sa307)* allele is a 243 bp

deletion, and is a strong loss-of-function mutation. The *ia60* mutation is a Mos1 transposon insertion in the *egl-9* gene, while the *sa330* allele is a C-to-T mutation that creates a nonsense codon at amino acid 38.^{13,34} The *hif-1(ia04)* mutation is a 1,231-bp deletion of the second, third, and fourth exons which causes a frame-shift and premature stop in the mutant mRNA.²⁰

3.3.2 HCN gas exposure assay

Assay setup. As shown in [Figure 3.1a](#), L4-stage worms were placed on 3.5 cm NGM agarose plates in the absence of bacterial food.

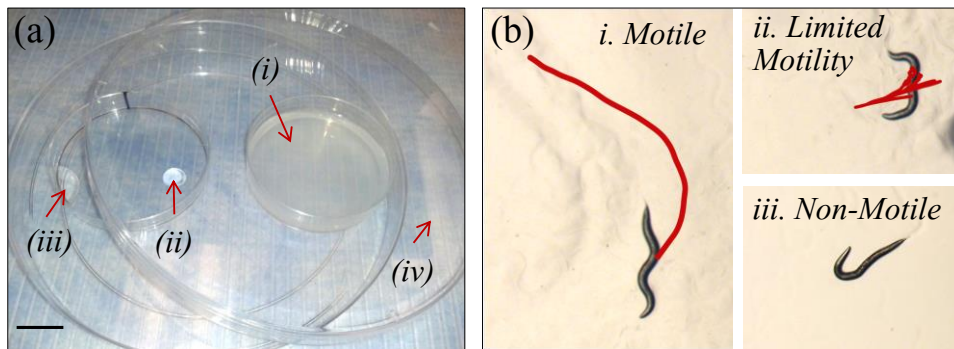


Figure 3.1 *C. elegans* susceptibility to HCN gas. **(a)** Setup for the gas assay: (i) unseeded NGM plate with L4-stage worms and, in a separate plate, aliquots of (ii) hydrochloric acid and (iii) KCN dissolved in sodium hydroxide. The liquids were mixed to generate HCN gas. The larger petri dish (iv) formed the chamber and was sealed with Parafilm to prevent any gas leakage. Scale bar = 20 mm. **(b)** worms were scored as being motile, having limited motility or being non-motile at 30-minute time points for a total of 150 minutes of HCN exposure, followed by 2 hours recovery in room air ($n = 60$, $N = 3$). In these photos, the red line traces the movement of a representative animal over 22 seconds.

This plate and a separate inverted 3.5 cm lid were positioned in a larger 10 cm petri dish. The lid contained drops of 0.18 M hydrochloric acid (100 μ l) and a solution of KCN (0.1 M) in 0.18 M sodium hydroxide (250 μ l). Concentrations of the chemicals used were based on previous work.¹³ The larger dish was then sealed with Parafilm M[®] and tipped

to mix the two liquids, thus generating HCN gas in the enclosed setup. For each 30-minute time point in the assay, a single plate of L4-stage worms was set inside its own individual chamber. A total of five such chambers were set up in a chemical fume hood for the five time points of the 2.5-hour assay. For observing recovery after HCN gas exposure, the fifth plate of worms was placed in room air (with a lid on top), and the worms were observed every 30 minutes. All observations of the phenotype were done using a Leica MS 5 stereomicroscope in room air. Every experiment included controls to assess consistency of HCN or KCN effects. At least three biological replicates were performed for each genotype tested.

Scoring worm phenotypes. At each time point, animals were scored as being motile, non-motile or having limited-motility (Figure 3.1b). The red line denotes the track of the worm body centroid over a period of 22 seconds. “Motile” worms (Figure 3.1 b.i) foraged actively on the plates on their own accord, without any need for tapping or prodding with a pick. Worms that showed slight movements of their head and body were scored as having “limited motility” (Figure 3.1 b.ii). Worms were scored as “non-motile” (Figure 3.1 b.iii) if they lay immobile on the plates and did not move despite tapping the plate and prodding with a pick.

3.3.3 RNA interference assays

RNAi experiments were performed as previously described.²¹ L4-stage worms were fed either HT115 bacteria with empty vector L4440 (negative control), HT115 bacteria with the vector expressing *egl-9* (positive control fed to wild-type worms) or

HT115 bacteria with the vector expressing *cysl-2*.³⁷ Animals were fed the RNAi food for two generations before conducting the experiments.

3.3.4 Quantitative real-time PCR

Trizol (Invitrogen) was used to isolate RNA from synchronized populations of L4-stage worms. The total extracted RNA from each sample was treated with DNase (Promega) and then reverse transcribed into complimentary DNA using Oligo(dT18) primers and AffinityScript reverse transcriptase (Stratagene). Quantitative RT-PCR was performed using SYBR GREEN supermix (Bio-Rad) and each reaction used cDNA from 100 ng of total RNA. The primers for K10H10.2 and *inf-1* have been previously published.^{36,37} Three biological replicates were analyzed for each experiment. Additionally, each PCR reaction was performed in duplicate. The standard curve method was used to analyze the expression levels.²² Two-sample unpaired t-tests were used to analyze the variation.

3.3.5 Microfluidic assay with cyanide in aqueous solution

The setup of the microfluidic assay is illustrated in [Figure 3.2a](#), and it includes a microfluidic chip housing the worms being tested, a stereozoom microscope and a computer-controlled camera. The microfluidic chips were fabricated using a standard soft-lithography process described in Section 1.3.^{8,9,28} The PDMS molds are punched with holes for the fluidic ports, and irreversibly bonded to a standard glass slide ([Figure 3.2b,c](#)). The final device design was selected after several rounds of preliminary tests.

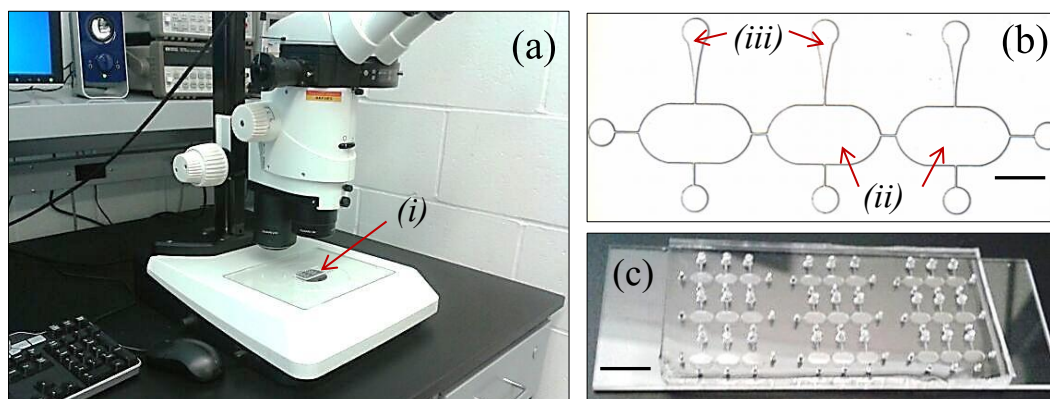


Figure 3.2 Setup for imaging the microfluidic assay. **(a)** The device (i) was observed under a stereomicroscope connected with a camera and computer. **(b)** Magnified image of three microfluidic chambers (ii) in which the worms were assayed; each chamber having its individual port (iii) through which the worms and chemical solutions are introduced. Scale bar = 1.5 mm. **(c)** Image of the actual PDMS microfluidic device bonded on a glass slide. Scale bar = 10 mm.

For the control experiments, a suspension of M9 buffer and *E. coli* OP50 bacteria is injected through the input port (Figure 3.2b). For the cyanide assay, 0.5 mM KCN in M9 buffer and bacterial suspension was prepared and filled in the chambers using the same method. The final concentration of *E. coli* was maintained at 0.2 O.D. (Optical Density) in both cases. For levamisole exposure, drug solutions in M9 buffer were prepared to expose the animals to concentrations of 0, 0.1, 1, 10 and 100 μM respectively. Single L4-stage worms were picked using a sterile platinum wire pick and dropped into the input port. A small amount of pressure was applied at the input port to push a single worm into each chamber. Once all three chambers were occupied by three individual worms, images were recorded for a period of 1000 seconds at the rate of one image per second. The saved videos were analyzed for extraction of the multiple locomotion parameters. To facilitate real-time imaging of worm movement, we used a Leica MZ16 transmission stereozoom microscope that has a wide field of view (to record multiple chambers) and 35 mm working distance (for fluidic handling).

The saved video files were post-processed by our custom worm tracking program described in Section 1.5.^{9,28} A custom Graphic User Interface (GUI) program, written in MATLAB, further allowed the user to calculate and plot the locomotion parameters from multiple data files. GraphPad Prism (GraphPad, USA), JMP, and SAS software were used for statistical analyses of the generated data.^{32,33}

3.4 Results

3.4.1 Over-activation of *hif-1* confers resistance to HCN gas

Prior studies had shown that *egl-9*-deficient worms could survive concentrations of HCN gas that killed wild-type worms.¹⁷ In our experiments, we monitored the effects of HCN gas on worm motility at 30 minute time points for a total of 150 minutes, and then examined the abilities of the animals to recover (Figure 3.3).

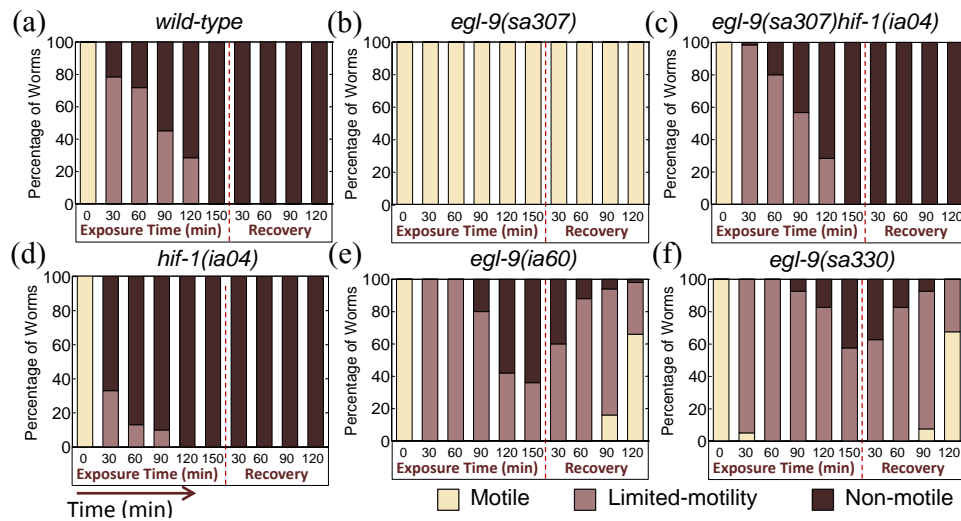


Figure 3.3 Characterizing worm movements in HCN gas assay. (a) Wild-type animals were rapidly immobilized by HCN gas and did not recover over the span of the assay. (b) *egl-9(sa307)* mutant animals remained motile in the presence of HCN gas. (c) The *egl-9(sa307) hif-1(ia04)* double mutants and (d) *hif-1(ia04)* showed a decrease in motility similar to wild-type and did not recover. HCN slowed *egl-9(ia60)* (e) and *egl-9(sa330)* (f) mutants, but the animals were able to recover motility after 2 h in room air.

As shown in [Figure 3.3a](#), wild-type animals were rapidly immobilized in the presence of HCN gas. In contrast, the *egl-9*-deficient animals ([Figure 3.3b](#)) were motile even after 2.5 hours, and foraged actively on the plates despite exposure to the toxicant. We hypothesized that the HCN resistance exhibited by *egl-9*-deficient mutants was due, in whole or in part, to over-activation of HIF-1. To test this, we compared the responses to HCN of *egl-9* mutants with those animals that carried loss-of-function mutations in both *egl-9* and *hif-1*. The double mutants were rapidly immobilized in the presence of cyanide gas ([Figure 3.3c](#)), and this phenotype was very similar to that of *hif-1* single mutant animals ([Figure 3.3d](#)). These results confirmed that resistance to HCN gas conferred by a loss-of-function mutation in *egl-9* was dependent on *hif-1* function.

3.4.2 Partial loss-of-function *egl-9* mutations confer intermediate resistance phenotypes

Prior genetic studies had isolated and characterized several different mutations in *egl-9*. Severe loss-of-function mutations, such as *egl-9(sa307)*, had been shown to cause egg-laying defects and dramatic over-expression of numerous HIF-1 targets.^{13,34,37,38} The defects conferred by the *egl-9(sa330)* and *egl-9(ia60)* mutations have been shown to be less severe.^{13,34} We tested the hypothesis that animals carrying the *egl-9(sa330)* or *egl-9(ia60)* mutations would have less resistance to HCN gas, compared to *egl-9(sa307)*. As seen in [Figure 3.3e](#) and [f](#), these less severe mutations resulted in an intermediate resistance phenotype. By 2.5 hours of exposure to the cyanide gas, these mutants were unable to actively forage on the plates. When left to recover from HCN gas exposure, they soon regained their motility.

While observing the phenotypes we found that there was a subtle difference in the extent and nature of limited motility of the *egl-9(ia60)* and the *egl-9(sa330)* alleles, but were unable to quantify it readily by manual scoring. These phenotypes demonstrated the need to diagnose behavioral responses to toxicants with higher spatio-temporal resolution. Additionally, we sought to develop technologies that would support the analysis of water-soluble toxicants, including KCN. Accordingly, we designed microfluidic devices coupled to real-time imaging and data analysis platforms. The HCN gas assays in [Figure 3.1](#) provided a valuable benchmark, as we developed novel and reliable cyanide toxicity assays in microfluidic systems.

3.4.3 Design of the microfluidic device

We proceeded to design a microfluidic chip suitable for assaying small, fast-acting toxicants. Unfortunately, existing devices were not optimal for KCN toxicity studies, so the design of a novel chip proved crucial to our experiments. In prior studies, we had fabricated microfluidic devices to measure the dose-dependent effects of levamisole (an anthelmintic drug) on the movement of *C. elegans* in real time and at high resolution.⁹ Even though these devices were later tested with other anthelmintic drugs, they could not be adopted for cyanide assays because of three main obstacles. First, they relied upon an electric field to guide the worms (i.e. electrotaxis), and an electric field would dissociate KCN molecules. In addition, some mutants of interest were not as sensitive to the applied electric fields as the wild-type *C. elegans*. Initial tests indicated that electrotaxis of *egl-9* mutants required electric fields at higher voltage ranges (10-12 volts) that incapacitate wild-type worms. Second, it was difficult to

contain the free-moving worms within the previously constructed microfluidic chamber in the presence of cyanide. We observed that worms responded quickly to KCN solution by trying to escape the chamber, and they explored potential exit points. In many cases, after cyanide application, worms were found swimming on the liquid surface in the exit ports. Third, agarose was not a suitable medium for observing worm movement, particularly for *egl-9* mutants. These mutants frequently paused in agarose-filled microfluidic chambers. We also tested alternate devices with soil-like pillar structures,²⁴ but the *egl-9* mutants paused in between the pillars.

The custom chip that we designed for this study overcomes these obstacles. It enables the worms to move freely in aqueous solutions, but does not allow them to escape. The chip was designed to have nine chambers, wherein three chambers were used simultaneously during an experimental run (Figure 3.2b and c). The dimensions of the chambers (length = 3.5 mm, width = 1.8 mm, height = 80 μm) were chosen to fit the field-of-view of the microscope under a suitable magnification with sufficient volume to allow free *C. elegans* swimming while maintaining the animals in a single plane of focus. Each chamber, in turn, had a one-way input port with a tapered neck (width = 25 μm , height = 80 μm) (Figure 3.2b). This design allowed us to simply push the worms into the chamber from one side but prevented them from escaping back through the port.

3.4.4 Presence of food as an essential factor for consistent worm movement

In experiments designed to optimize the conditions for behavioral analyses in microfluidic devices, we determined that bacterial food promoted consistent movement.

In the absence of food, the *egl-9* mutants had a tendency to rest for long periods of time; resulting in a great variability in centroid velocity (Figure 3.4).

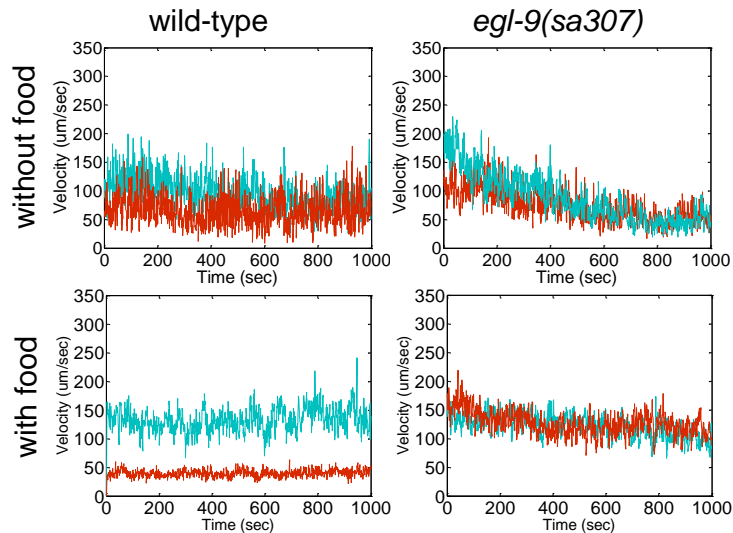


Figure 3.4 Average centroid velocity of worms without food (*E. coli*) in microfluidic chambers. The *egl-9* mutants were moved very little in the microfluidic chamber and rested for long periods of time. Blue line shows the control experiment and red line shows the worms exposed to 0.5 mM aqueous KCN.

This resting behavior was also displayed in other environments that lacked food, including agarose plates or microfluidic chambers filled with agarose gel or PDMS support pillars (data not shown). However, when food was added, the worms moved more consistently. This suggests that food can be an important variable in microfluidic behavioral studies. In the later experiments, we ensured that the animals had ample food.

3.4.5 Multi-parameter behavioral analysis in aqueous cyanide solution

To more completely and accurately define the effects of KCN on wild-type and mutant animals we used real-time imaging of *C. elegans* in microfluidic chambers to address the following questions: Are the effects of KCN immediate, or do *C. elegans* slow down over time? What is the range of velocities exhibited by a population in the

presence of the toxicant? Do our data support the hypothesis that mutations that protect *C. elegans* from HCN gas also protect the animals from aqueous KCN?

For experiments examining cyanide response phenotypes in microfluidic devices, individual chambers were filled with chemical solutions described in Materials and Methods and illustrated in [Figure 3.2](#). Single L4-stage worms were then inserted into the microfluidic chambers, and their movement was recorded for 1000 s. The worm tracking program produced a list of body centroid locations for each animal as a function of time, which provided quantitative information on the resistance phenotypes.

Average velocity of body centroid. To assess the effects of cyanide on wild-type and mutant animals, we placed the animals in the microfluidic chamber, tracked movement over time, and calculated the velocity of the body centroid. More precisely, we calculated the ratio of the net distance between two successive points to the net change in time (1 s). An example is shown in [Figure 3.5a](#), in which a worm located at centroid position (x_1, y_1) at time instance t_1 swam to another centroid position (x_2, y_2) at time instance t_2 . The red dotted line denotes the path of the body centroid and the centroid velocity v_{21} can be expressed by Equation 1:

$$v_{21} = \sqrt{(x_2 - x_1)^2 + (y_2 - y_1)^2} / (t_2 - t_1) \quad (1)$$

The effects of KCN on wild-type worms were evident from time 0. In [Figure 3.5b-f](#), the plots provide information on the magnitude of overall average centroid velocity for particular populations at every second. The blue lines represent the control conditions, while the red lines show average centroid velocities in the presence of 0.5

mM KCN. Notably, the average centroid velocity of wild-type worms did not change markedly over the 1000 seconds of recording (Figure 3.5b). In contrast to the wild-type animals, the *egl-9(sa307)* mutants showed similar average centroid velocities both in control conditions ($122 \pm 19 \mu\text{m/s}$) and in cyanide solution ($127 \pm 21 \mu\text{m/s}$). Interestingly, in the first few seconds of the assay, the *egl-9(sa307)* animals moved faster in the presence of KCN, compared to controls.

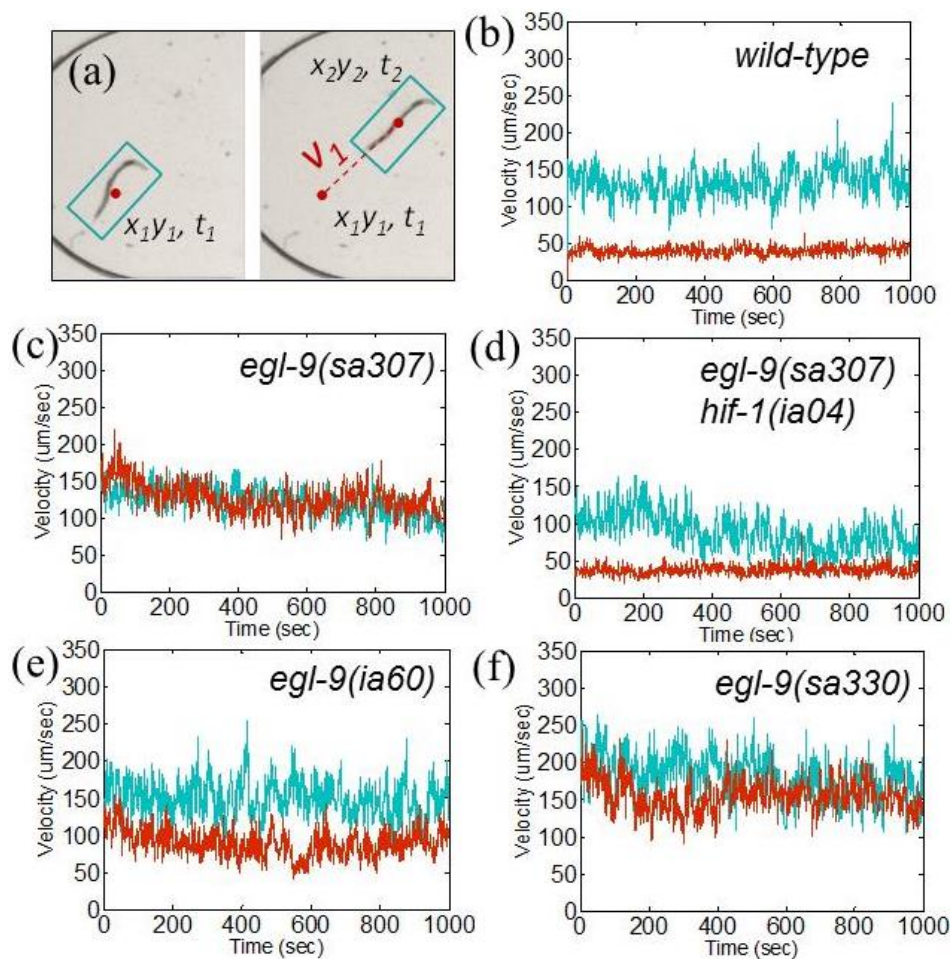


Figure 3.5 Effects of cyanide on worm velocity in the microfluidic assay. (a) In this diagram, the red-dotted line denotes the representative path of the body centroid. The velocity was calculated using the worm's centroid positions $[(x_1, y_1)$ and $(x_2, y_2)]$ at their two successive time instances (t_1 and t_2). (b–f) Average velocity of body centroid in control (blue) and 0.5 mM liquid cyanide (red) conditions. In all plots, the centroid velocity was calculated by taking the average of all instantaneous velocities of all animals ($n = 15$, $N = 7$).

As predicted, the KCN resistance phenotype exhibited by *egl-9(sa307)* mutants was suppressed by a loss-of-function mutation in *hif-1* (compare Figures 3.5c with d). We also assayed two weaker alleles of *egl-9*. As shown in Figure 3.5e, the *egl-9(ia60)* mutants were slowed by KCN, but not as the wild-type. The KCN had relatively little effect on the centroid velocity of *egl-9(sa330)* animals (Figure 3.5f).

Total distance covered by the body centroid. To understand the summative consequences of changes in movement over time, we calculated the total distance traveled by each population assayed. Figure 3.6a-c depicts the movement of representative individuals in the microfluidic device. Figure 3.6d plots the average distance travelled by the worms' body centroid during 1000 seconds.

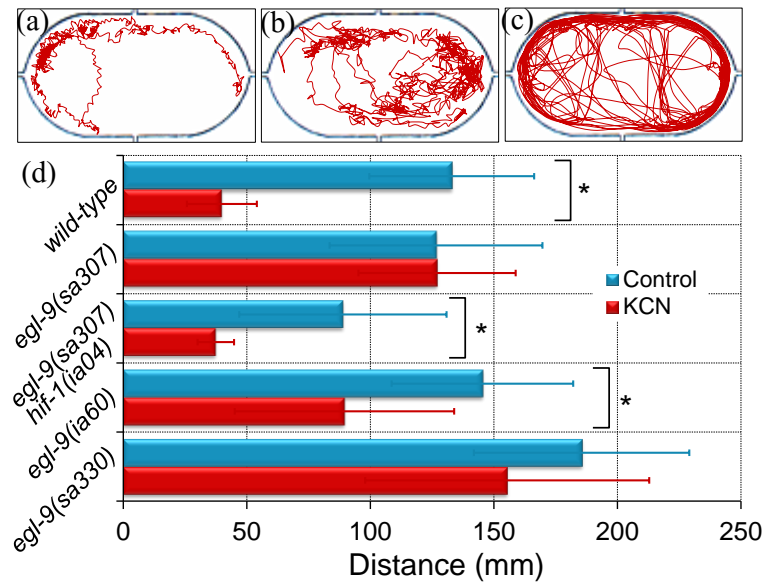


Figure 3.6 Total distance traveled in the microfluidic chambers. (a–c) Examples of tracks of animals affected differently by KCN. (a) Tracks representative of animals that exhibited periods of limited motility and eventually ceased movement. (b) Tracks representative of animals that exhibited periods of limited motility in the presence of the toxicant but did not become immotile. (c) Tracks representative of animals that continued to swim around the chamber throughout the experiment. (d) The average distance travelled by the worms within 1000 seconds of recording is shown (n = 15, N = 7). * $p < 0.0002$, two-way ANOVA.

Under control conditions, the wild-type and *egl-9(sa307)* mutants roughly covered the same distance (133 ± 33 mm), but wild-type animals traveled significantly less distance in the KCN solution (40 ± 13 mm, $p < 0.0001$). The *egl-9(sa307)hif-1(ia04)* double mutant also showed a significant decrease from 89 ± 42 mm in control to 37 ± 7 mm in cyanide solution ($p < 0.0002$). In control conditions, the *egl-9(sa330)* strain covered the maximum distance, relative to other strains tested. The *egl-9(ia60)* strain showed a significant decrease in the distance covered upon cyanide exposure (from 145 ± 37 mm in control to 90 ± 44 mm in cyanide solution, $p < 0.0001$).

Do the cyanide-induced decreases in distance traveled reflect a slower-moving worm with uniform velocity or a relatively fast-moving worm that pauses intermittently? Is the answer the same for all individuals in a population? To address these questions, we examined the movement patterns of individual animals (Figure 3.7). We also calculated peak velocities for each condition (Figure 3.8), and we quantified the times that worms were immotile (Figure 3.9).

Behavioral raster representation of instantaneous centroid velocity. To more fully understand the effects of the toxicant, we examined the range of responses exhibited by individual worms. Figure 3.7 represents the instantaneous centroid velocities in microfluidic devices as behavioral raster plots. Each row is a collection of pixels, where the color intensity of each pixel reflects the relative instantaneous centroid velocity of an individual worm that is tracked for 1000 s: from light tan indicating high velocity to dark brown indicating no movement. The plots thus provide a very detailed look at the distribution of individual worm velocities. The *egl-9(sa307)* mutant animals

showed a lighter raster in both the control and experimental conditions with almost no pauses. Worms with the weaker allele, *egl-9(ia60)*, had a relatively darker raster in the cyanide solution as compared to that in control conditions.

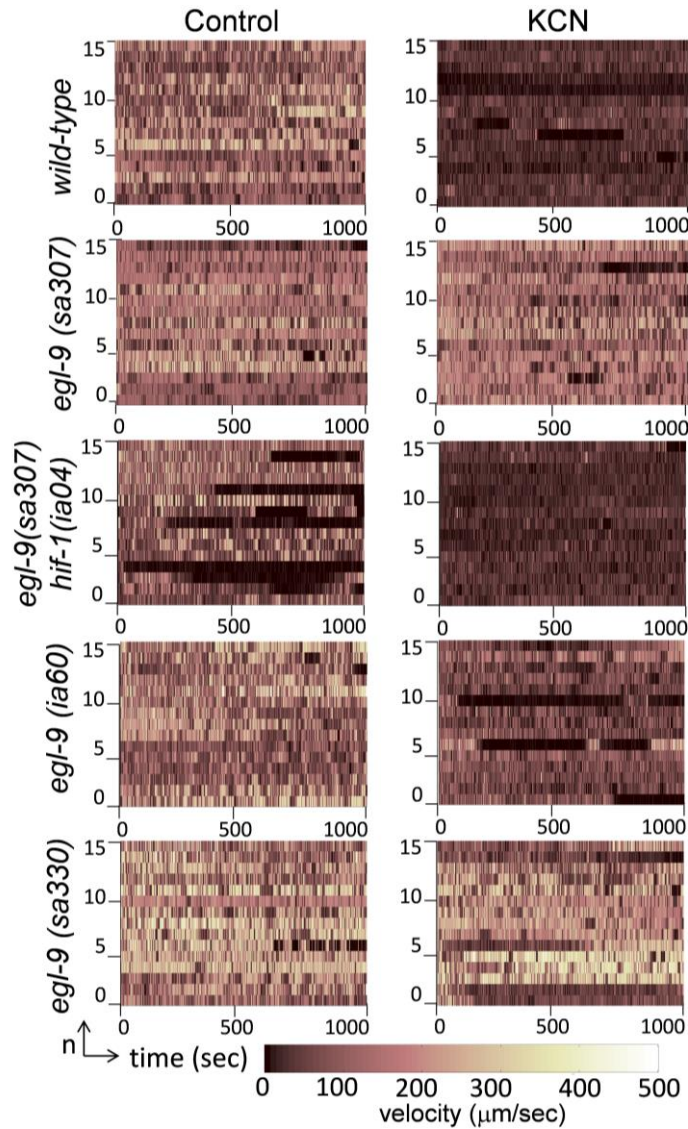


Figure 3.7 Behavioral raster plots of the centroid velocities. In our color scheme, white color denotes a maximum velocity of 500 $\mu\text{m/s}$ and black color denotes a minimum velocity of 0 $\mu\text{m/s}$. Within every raster plot, each individual row corresponds to a distinct animal that is tracked for 1000 seconds and the color intensity of each pixel corresponds to the animal's instantaneous velocity ($n = 15$, $N = 7$). The wild-type and *egl-9(sa307) hif-1(ia04)* double mutants show a distinctly slower velocity in cyanide solution (as shown by a darker raster) compared with that in control conditions. The *egl-9(sa307)* mutants had similar velocities in both control and experimental conditions (as shown by a lighter raster).

In some cases, individual animals paused for long intervals. A few of the wild-type and the *egl-9(ia60)* worms were inactive for long intervals. Interestingly, approximately half of the *egl-9(sa307)hif-1(ia04)* double mutants paused for extended periods in control conditions. This behavior was less evident in the presence of KCN, which suppressed movement in all the wild-type and *hif-1*-deficient worms assayed. The *egl-9(sa330)* animals moved quickly and paused infrequently.

Range and distribution of average centroid velocity. Recognizing the variable responses of individual animals as illustrated in the raster plots, we interrogated these phenotypes further by calculating the distribution of centroid velocities achieved by each genotype in each condition (Figure 3.8).

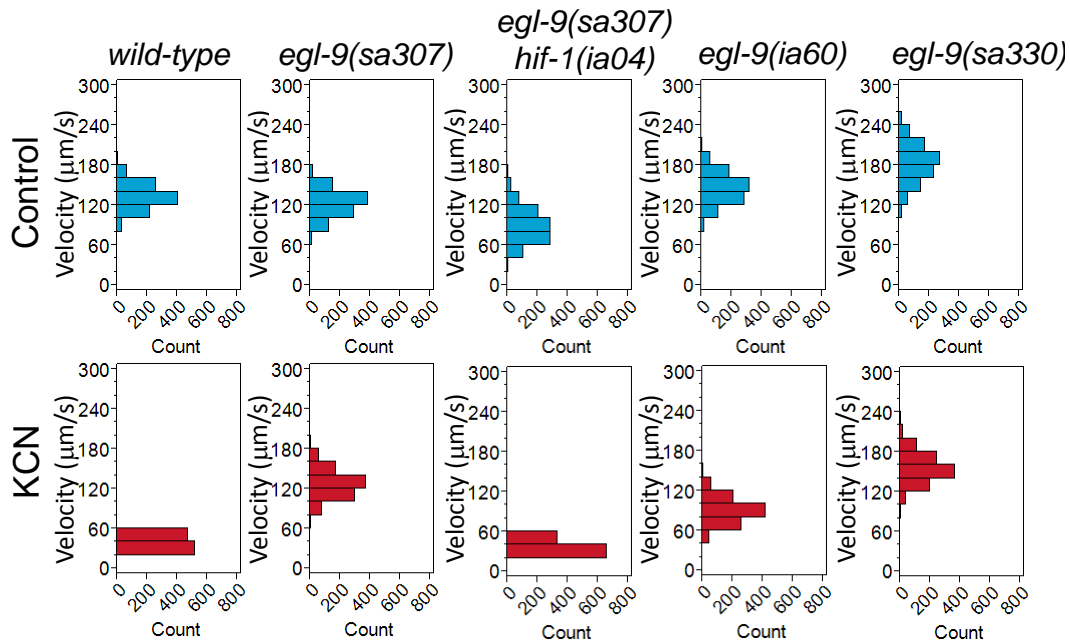


Figure 3.8 Range and distribution of the average centroid velocities. Compared with *egl-9(sa307)* mutant animals, the other genotypes showed a decrease in their mean velocities when exposed to 0.5mM KCN (red). Data for control conditions are shown in blue (n = 15, N = 7).

This range and distribution of centroid velocities is estimated by counting the occurrences of velocity values within intervals of 20 $\mu\text{m/s}$ for all worms tested under control or experimental conditions. In control conditions, the mean velocity for wild-type and *egl-9(sa307)* animals were $133 \pm 19 \mu\text{m/s}$ and $123 \pm 19 \mu\text{m/s}$, respectively. In cyanide solution, this mean velocity for *egl-9(sa307)* worms showed no significant change ($127 \pm 21 \mu\text{m/s}$, $p > 0.05$), whereas the mean velocity for wild-type worms decreased significantly ($40 \pm 6 \mu\text{m/s}$, $p < 0.0001$) (Figure 3.8). Compared with wild-type, the *egl-9(sa307)hif-1(ia04)* worms exhibited a slightly lower mean velocity in control conditions ($89 \pm 25 \mu\text{m/s}$), but they showed a significant decrease in cyanide solution ($37 \pm 7 \mu\text{m/s}$). Consistent with the raster plots (Figure 3.7), the *egl-9(sa330)* animals moved relatively faster than the other worms types in control conditions ($182 \pm 28 \mu\text{m/s}$) with a wider range. In cyanide solution, the mean velocity of the *egl-9(sa330)* animals decreased to $155 \pm 23 \mu\text{m/s}$. The *egl-9(ia60)* mutants behaved similar to wild-type animals in control conditions ($143 \pm 23 \mu\text{m/s}$) but did not show a dramatic decrease in mean velocity upon cyanide exposure ($90 \pm 19 \mu\text{m/s}$).

Pausing behavior. To further define this behavior, we identified and quantified the instances in which individual worms slowed to velocities in the 0-15 $\mu\text{m/s}$ range. These data are shown as boxplots in Figure 3.9. To our advantage, the worm tracking program was particularly sensitive in detecting miniscule changes in centroid velocity with a resolution of 7.5 $\mu\text{m/s}$. After recording the videos, the worm velocities extracted from the software were compared manually. We noticed that a centroid velocity of 15 $\mu\text{m/s}$ corresponded to worms that exhibited only small changes in body posture and were

otherwise immotile. Hence, we chose 15 $\mu\text{m/s}$ as the threshold velocity below which animals were recorded as having stopped. Cyanide caused an increased number of stops, relative to control conditions, for the wild-type animals (26 in control, 155 in cyanide) and *egl-9(sa307)hif-1(ia04)* double mutants (66 in control, 197 in cyanide). By comparison we found that the cyanide treatment did not cause the *egl-9* single mutants to stop as frequently. In some cases, these analyses reveal differences that were not evident from cursory examination of the raster plots. For example, although the mean velocities of *egl-9(sa307)* and wild-type are very similar (Figure 3.8), the *egl-9(sa307)* mutants paused more frequently than did wild-type animals in control conditions (Figure 3.9).

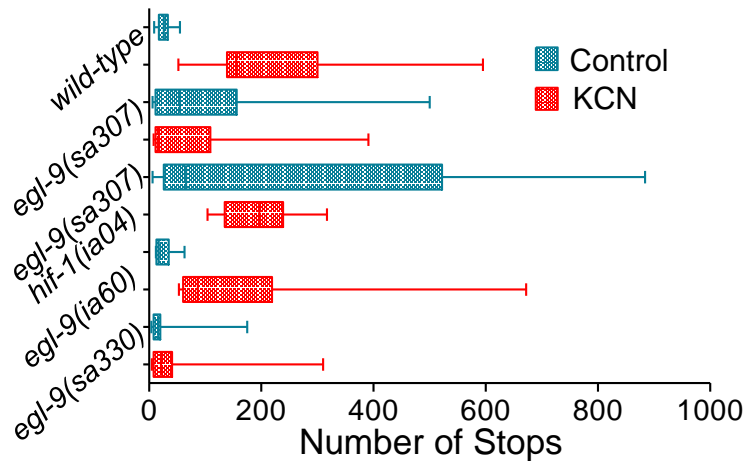


Figure 3.9 Number of pauses in the microfluidic chambers. Pauses were counted as time instances (within the entire 1000 s) when the centroid velocity was less than a threshold velocity of 15 $\mu\text{m/s}$. Blue bars represent control conditions and red bars represent experimental conditions ($n = 15$, $N = 7$).

3.4.6 Deciphering the role of *cysl-2* in cyanide resistance

We next investigated the role of the cysteine synthase-like gene *cysl-2* in *egl-9*-mediated resistance to aqueous KCN. Over-expression of HIF-1 in *egl-9* mutants has

been shown to cause a marked increase in the expression of *cysl-2/K10H10.2* mRNA.^{7,34,36,37} Further, during the course of our studies, Budde and Roth⁷ had demonstrated that RNAi-mediated depletion of *cysl-2* caused *egl-9*-deficient animals to become more susceptible to HCN gas. We proposed two testable hypotheses. First, we predicted that RNAi-mediated depletion of *cysl-2* would diminish the resistance of *egl-9* deficient mutants to KCN in aqueous solution. Second, we hypothesized that there would be a correlation between the levels of *cysl-2* mRNA levels and the cyanide resistance phenotypes in *egl-9* mutant animals.

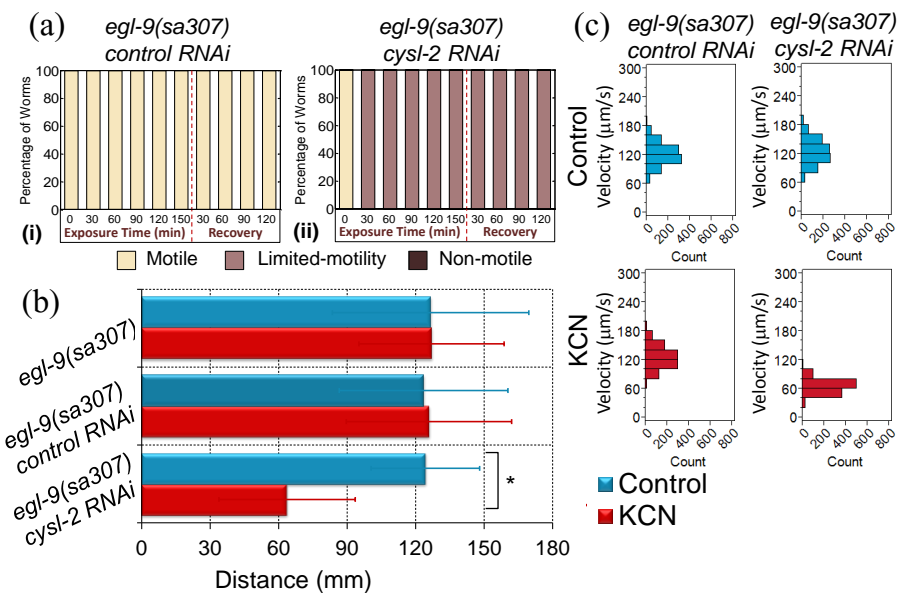


Figure 3.10 Effects of *cysl-2* depletion on cyanide resistance. **(a)** In the presence of HCN gas, *egl-9(sa307)* worms treated with control RNAi (i) remain motile, but *cysl-2* (RNAi) (ii) suppresses this resistance phenotype (n = 60 and N = 3). **(b)** Average distance travelled in the microfluidic chambers. * $p < 0.0001$, two-way ANOVA (n = 15, N = 7). **(c)** Frequency distribution of the average centroid velocities shows a decrease in mean velocity for *cysl-2* RNAi treated *egl-9(sa307)*.

In control experiments, we tested the hypothesis that reducing *cysl-2* expression would largely suppress resistance to HCN gas in *egl-9(sa307)* animals; we depleted *cysl-*

2 mRNA by feeding them bacterial food that carried double-stranded *cysl-2* RNA (*cysl-2* RNAi). The efficacy of the RNAi protocol was validated in parallel experiments (Figure 3.11). The *egl-9(sa307)* mutants treated with *cysl-2* RNAi (Figure 3.10 a.ii) slowed down in the presence of HCN gas. By comparison, the *egl-9(sa307)* mutants fed control RNAi bacteria were resistant to the toxicant (Figure 3.10 a.i).

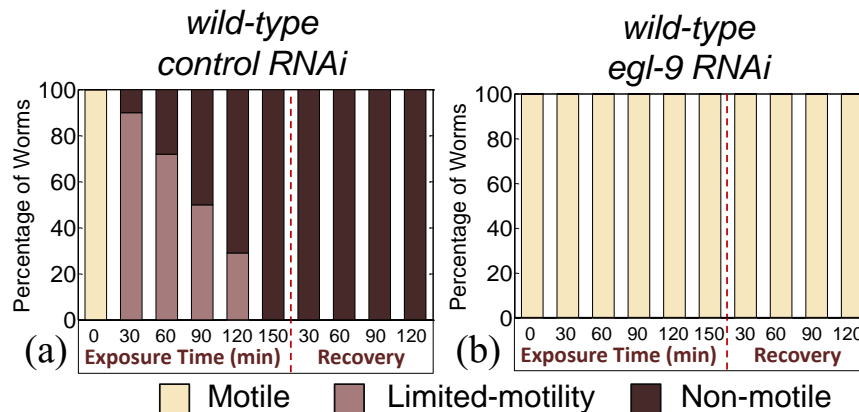


Figure 3.11 Effects of *egl-9* depletion on cyanide resistance. (a) wild-type worms treated with control RNAi were rapidly immobilized by HCN gas. (b) Knockdown of *egl-9* by RNAi in wild-type worms conferred resistance to the toxicant.

To examine the role of *cysl-2* in KCN toxicity, we performed experiments in the microfluidic device pictured in Figure 3.2c. We found that depletion of *cysl-2* by RNAi increased the sensitivity of *egl-9(sa307)* mutant animals to the toxicant. This was evidenced by a significant decrease in average distance traveled ($p < 0.0001$, two-way ANOVA; Figure 3.10b) and reduced average centroid velocity. The *cysl-2* RNAi did not have marked effects on the mean velocity of the *egl-9(sa307)* animals in control conditions, but toxicant exposure caused a decrease in mean velocity (Figure 3.10c).

To test the hypothesis that there would be a correlation between the levels of *cysl-2* mRNA levels and the cyanide resistance phenotypes in *egl-9* mutant animals, we

performed quantitative real-time PCR and assessed the levels of *cysl-2* expression in *egl-9(sa307)*, *egl-9(sa330)*, and *egl-9(ia60)* mutant animals (three biological replicates for each). We found that the expression level of *cysl-2* mRNA was 11-fold higher in *egl-9(sa307)* strong loss-of-function mutants compared to the *egl-9(ia60)* and *egl-9(sa330)* mutants (Table 3.1). Together, these data are consistent with the hypothesis that the strong cyanide resistance phenotype in *egl-9(sa307)* mutant animals is due to higher levels of *cysl-2* expression compared with the *egl-9(sa330)* and *egl-9(ia60)* mutants, which show comparatively reduced resistance.

Table 3.1 Comparison of relative *cysl-2* mRNA expression levels.

Genotypes compared	Relative mRNA expression levels
<i>egl-9(sa307)</i> compared to <i>egl-9(ia60)</i>	11.34 ± 8
<i>egl-9(sa307)</i> compared to <i>egl-9(sa330)</i>	11.03 ± 5.4

3.4.7 Robustness of the assay and broader applications

We investigated whether these assays could be adapted for increased throughput, as this might also broaden its applicability. Higher throughput might be accomplished most readily by increasing the number of animals in each chamber or by shortening the time of assay. We determined that inserting multiple worms (up to three) inside individual microfluidic chambers did not markedly change the cyanide resistance phenotype (Figure 3.12). We measured the average centroid velocities of wild-type and *egl-9(sa307)* worms in control and experimental conditions. Tests were conducted by using one, two or three worms within individual microfluidic chambers. In each set of

experiments, KCN caused a significant decrease in the velocity of the wild-type worms in each case (Figure 3.12, $p < 0.0001$). This indicates that the microfluidic assay is not limited to testing a single worm per chamber but can be scaled-up for multiple worms (up to three) per chamber without losing resolution.

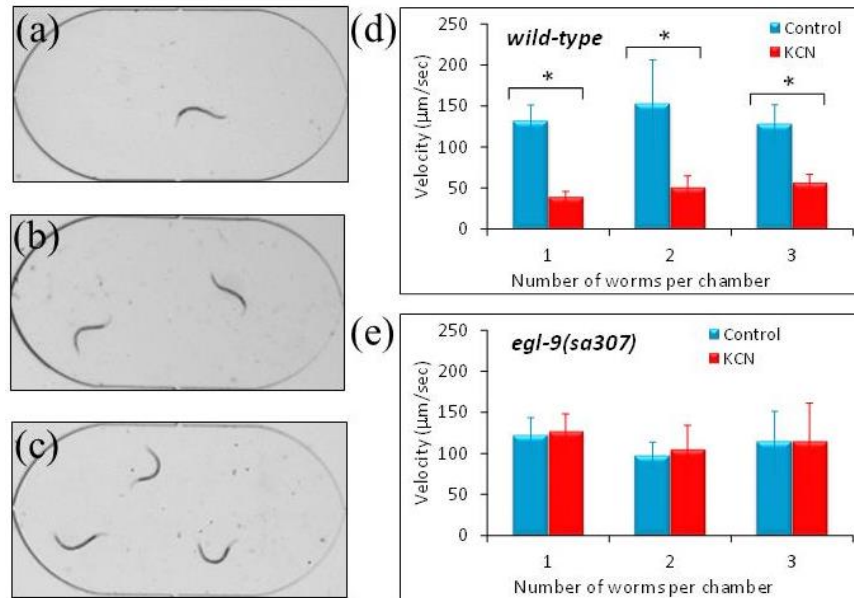


Figure 3.12 Scaling-up the microfluidic technique with multiple worms in individual chambers. (a–c) Snapshots of the microfluidic chamber housing one, two, or three worms ($n = 12$, $N = 3$). (d) Average centroid velocities of single or multiple wild-type worms in a microfluidic chamber are plotted under control conditions and 0.5 mM KCN. In each of the three cases (with one, two, or three worms), there was a significant reduction in the centroid velocity upon exposure to cyanide solution ($*p < 0.0001$). (e) Average centroid velocities of single or multiple *egl-9(sa307)* worms. The number of worms in the chamber had no significant difference on the average velocity measured in each condition ($p > 0.05$).

Furthermore, we noticed that the duration of the microfluidic experiment could be shortened without losing crucial information. In other words, even though our microfluidic experiments were recorded for 1000 seconds, the required behavioral information could be obtained from experiments recorded for the first 300 seconds. As an example, the percentage reduction in average centroid velocity for worms in cyanide

solution was roughly maintained throughout the experimental duration of 1000 seconds (Figure 3.5b). Our calculations show that, for wild-type worms, the percentage reduction in average centroid velocity caused by cyanide exposure was approximately 30%, whether it was measured over 300, 600 or 900 seconds. This 3-fold decrease in experimental time will be particularly useful in further improving the efficiency of the microfluidic assay.

We designed the microfluidic chamber with the idea that it could be applicable to other water soluble toxicants that cause acute changes in mobility, potentially inducing genotoxins, heavy metals, environmental toxicants, pharmacological products and xenobiotics. To test this principle, we used the assay, coupled with real time imaging, to analyze the effects of the anthelmintic drug levamisole on wild-type worm motility. As seen in Figure 3.13, the total distance covered by the worms steadily decreased with an increase in the concentration of the drug.

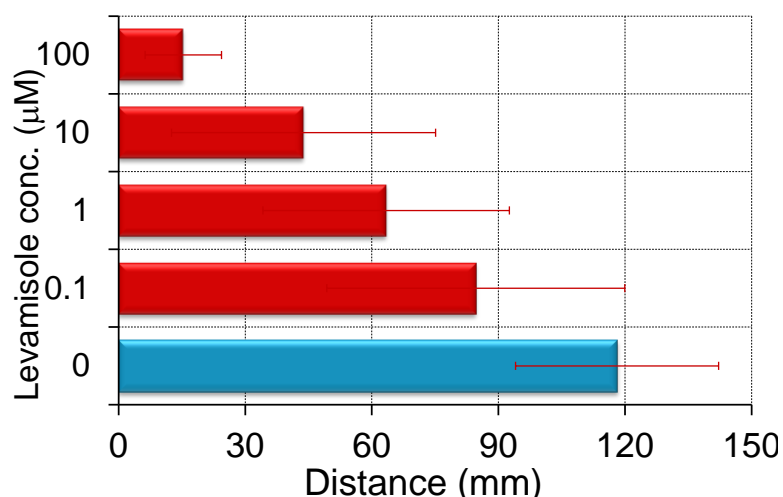


Figure 3.13 Applicability of the microfluidic device. The distance covered by wild-type worms decreased as the concentration of the anthelmintic drug levamisole increased from 0 μM (control) to 100 μM ($n = 12$, $N = 3$).

3.5 Discussion

Overactivation of HIF-1, via loss-of-function mutations in *egl-9*, has been shown to impact *C. elegans* longevity and stress resistance.²⁹ We were particularly interested in investigating how a loss-of-function mutation in *egl-9* and the accompanying overactivation of HIF-1 could protect *C. elegans* from cyanide toxicity. In this chapter, we have presented a novel microfluidics-based approach to study the responses of *C. elegans* to this toxicant. We confirmed that the resistance of *egl-9(sa307)* strong loss-of-function worms was dependent on *hif-1* function, and we investigated the HCN resistance phenotypes of other mutant alleles of *egl-9*. Compared with the *egl-9(sa307)* mutation, the *ia60* and *sa330* alleles cause less severe egg-laying defects.^{13,34} Here, we reported a correlation between *cysl-2* mRNA expression and cyanide resistance phenotypes in these *egl-9* mutants. Detailed analyses of intermediate phenotypes, such as those exhibited by the *egl-9(ia60)* and *egl-9(sa330)* strains, can be very informative to understanding the genetic bases of cyanide response and resistance.

Microfluidics allowed us to quantitate the responses to aqueous toxicants with superior spatio-temporal resolution at the individual worm level and in a much shorter period of time. We established that the genotypes that were resistant to HCN gas were also resistant to aqueous KCN in the microfluidic device. We investigated multiple parameters, including average centroid velocity, total distance covered, behavioral raster representation of individual animals, range and distribution of mean velocities, and pausing behavior. Collectively, these data provide a rich and detailed analysis of the cyanide resistance phenotypes, and of the roles of *egl-9*, *hif-1*, and *cysl-2*.

3.5.1 Higher spatiotemporal resolution in microfluidic assay

Prior studies have demonstrated the efficacy of microfluidic devices for *C. elegans* analyses, such as force sensor arrays,¹⁵ mazes,^{27,30} microtraps,^{19,24} fluorescent sorters,^{10,11} electrotaxis sorters,^{26,31} and olfactory assays,¹⁰ and recent review articles summarize the key developments in microfluidic worm chips.^{6,10,12,14} The combination of microfluidics and automated imaging increases the power of *C. elegans* as a genetic model system to study the effects of toxicants or chemical interventions in real time. A major contribution of our work is the development of a liquid-based microfluidic assay coupled to imaging technologies to quantify the toxicant response of *C. elegans*. The discrete scoring of worm motility was further quantified by specific movement parameters generated by our computer program after real-time imaging (Figure 3.14).

Standard Assay	Microfluidic Assay
motile	motile Velocity 100-260 $\mu\text{m}/\text{sec}$ Distance 120-180 mm Stops 20-50
limited-motile	limited-motile Velocity 40-150 $\mu\text{m}/\text{sec}$ Distance 50-120 mm Stops 50-200
non-motile	non-motile Velocity 20-80 $\mu\text{m}/\text{sec}$ Distance 25-50 mm Stops 70-600

Figure 3.14 Summary list of parameters extracted from gas exposure assay and microfluidic assay. In the gas exposure assay, worms were visually scored as being non-motile, motile or having limited-motility. The microfluidic assay complements the gas exposure assay by quantifying worm movement with multiple-parameters (centroid velocity, raster plots, distance traveled, and number of stops) extracted by an automated computer program.

The need for a real-time analysis system with increased resolution is particularly acute when analyzing subtle phenotypic differences among genotypes of interest. Mutants with strong cyanide resistance phenotypes [such as *egl-9(sa307)*] show markedly distinct movement patterns under cyanide exposure compared to the wild-type worms. This behavior is easy to detect and score manually in gas-based assays (Figure 3.1). However, differences between mutants with weaker cyanide resistance [such as *egl-9(ia60)*] are difficult to score manually, especially when they have a range of decreased velocities or pause for extended times. The microfluidic assay provided much higher spatio-temporal resolution, we were able to record the x and y coordinates (Figure 3.5) of each individual worm at every second of the assay time span. The average velocity of the worm populations (Figure 3.5) showed that the effects of KCN were quick, and the drop in velocity was then consistent for the time span we tested. The total distance covered by the worms (Figure 3.6) gave an overview of the cumulative effects of the toxicant on worm movement. Interestingly, the behavioral raster representation of individual worms showed some surprising insights into worm behavior in the toxicant. The real-time imaging and worm tracking program allow us to detect velocities as low as 7.5 $\mu\text{m/s}$ and number of pauses as small as 20-50, which cannot be recorded via a manual scoring technique

Using these technologies we discovered important features of specific strains and their responses to cyanide. Of particular interest: (1) the *egl-9(sa307)hif-1(ia04)* double mutant strain had lower overall velocity in control conditions compared to the wild-type strains. Our data show that this difference was largely attributable to more frequent

pausing (Figure 3.7 and Figure 3.9). (2) In control conditions the *egl-9(sa330)* mutant worms moved a greater distance during the course of the experiment. This was due to both higher peak velocity (Figure 3.8) and less pausing (Figure 3.9). (3) In both the HCN gas assays and the KCN toxicity experiments, the *egl-9(ia60)* strain was more affected by the toxicants, relative to the *egl-9(sa330)* strain. As shown in Figure 3.7 and Figure 3.9, the *egl-9(sa330)* mutants did not pause more frequently in response to KCN, and while the mean velocity was lower in KCN (Figure 3.8), the summative effects on total distance were relatively small (Figure 3.6)

3.5.2 Genetics of cyanide resistance in *C. elegans*

Over-activation of HIF-1 has been shown to dramatically increase expression levels of the cysteine synthase *cysl-2* gene, and Budde and Roth hypothesized that *cysl-2* functioned to metabolize cyanide.^{7,34,37} This suggested a model in which loss of *egl-9* function increases HIF-1 activity, which in turn increases *cysl-2* expression and the ability of *C. elegans* to inactivate toxic cyanide. Here, we tested specific predictions made by this model. First, we asked whether depletion of *cysl-2* was sufficient to suppress the *egl-9(sa307)* cyanide resistance phenotype, assayed in gas chambers or in liquid. As shown in Figure 3.10, depletion of *cysl-2* by RNA interference dramatically decreased the resistance of *egl-9(sa307)* animals to cyanide. The microfluidic technologies coupled to real-time imaging provided quantitative descriptions of these phenotypes (Figure 3.13). The *egl-9(sa307)* animals treated with *cysl-2* RNAi exhibited decreased average centroid velocity and distance travelled when compared to control RNAi treatments. Additionally, we found that the levels of the *cysl-2* cysteine synthase

mRNA were much higher in the *egl-9(sa307)* mutant animals compared to the *egl-9(ia60)* and *egl-9(sa330)* mutants. This correlates well with the variation we observed in the cyanide resistance phenotype in these strains. While these data clearly show that *cysl-2* has a central role in cyanide resistance, we postulate that other HIF-1 targets also contribute to the ability of *egl-9* mutants to survive in the presence of this toxicant.

3.6 Conclusion

In this chapter, we discussed a new microfluidic technology to examine the genetic underpinnings of cyanide resistance. The HCN gas exposure assay validated the microfluidic assay, and both provided insights to the phenotypes and reinforced central conclusions. Prior studies had shown that mutations in *egl-9* protected *C. elegans* from cyanide. Here, we show that this resistance phenotype is dependent upon the HIF-1 transcription factor. Further, the expression of *cysl-2* in each mutant correlates with the degree of cyanide resistance. This was further assayed by multi-parameter analyses of worm motility, which described these phenotypes in much greater detail. The combination of *C. elegans* genetics and the microfluidics-enabled approaches and technologies developed here can be used to address many toxicological and biological questions. HIF-1 in particular has been shown to have roles in the responses to diverse stresses and toxicants,²⁹ and in future studies we will employ these and related technologies to elucidate the functions of HIF-1 and interacting genes. The combination of real-time imaging, microfluidic technologies, and *C. elegans* genetics hold great promise for the study of water-soluble toxicants.

3.7 References

1. D. R. Albrecht and C. I. Bargmann, *Nature Methods*, 2011, **8**, 599-605.
2. D. M. G. Beasley and W. I. Glass, *Occupational Medicine*, 1998, **48**, 427-431.
3. T. Bishop, K. W. Lau, A. C. R. Epstein, S. K. Kim, M. Jiang, D. O'Rourke, C. W. Pugh, J. M. Gleadle, M. S. Taylor, J. Hodgkin and P. J. Ratcliffe, *PLoS Biology*, 2004, **2**, e289.
4. C. Blumer and D. Haas, *Archives of Microbiology*, 2000, **173**, 170-177.
5. S. Brenner, *Genetics*, 1974, **77**, 71 - 94.
6. S. D. Buckingham and D. B. Sattelle, *Invertebrate Neuroscience*, 2008, **8**, 121-131.
7. M. W. Budde and M. B. Roth, *Genetics*, 2011, **189**, 521-532.
8. J. A. Carr, R. Lycke, A. Parashar and S. Pandey, *Applied Physics Letters*, 2011, **98**, 143701-143703.
9. J. A. Carr, A. Parashar, R. Gibson, A. P. Robertson, R. J. Martin and S. Pandey, *Lab on a Chip*, 2011, **11**, 2385-2396.
10. N. Chronis, M. Zimmer and C. I. Bargmann, *Nature Methods*, 2007, **4**, 727-731.
11. K. Chung, M. M. Crane and H. Lu, *Nature Methods*, 2008, **5**, 637-643.
12. M. M. Crane, K. Chung, J. Stirman and H. Lu, *Lab on a Chip*, 2010, **10**, 1509-1517.
13. C. Darby, C. L. Cosma, J. H. Thomas and C. Manoil, *Proceedings of the National Academy of Sciences*, 1999, **96**, 15202-15207.
14. P. S. Dittrich and A. Manz, *Nature Review of Drug Discovery*, 2006, **5**, 210-218.
15. J. C. Doll, N. Harjee, N. Klejwa, R. Kwon, S. M. Coulthard, B. Petzold, M. B. Goodman and B. L. Pruitt, *Lab on a Chip*, 2009, **9**, 1449-1454.
16. A. C. R. Epstein, J. M. Gleadle, L. A. McNeill, K. S. Hewitson, J. O'Rourke, D. R. Mole, M. Mukherji, E. Metzen, M. I. Wilson, A. Dhanda, Y.-M. Tian, N. Masson, D. L. Hamilton, P. Jaakkola, R. Barstead, J. Hodgkin, P. H. Maxwell, C. W. Pugh, C. J. Schofield and P. J. Ratcliffe, *Cell*, 2001, **107**, 43-54.

17. L. A. Gallagher and C. Manoil, *Journal of Bacteriology*, 2001, **183**, 6207-6214.
18. J. Hamel, *Critical Care Nurse*, 2011, **31**, 72-82.
19. S. E. Hulme, Shevkoplyas, S. S, Apfeld, J., Fontana, W., Whitesides, G. M., *Lab on a chip*, 2007, **7**, 1515.
20. H. Jiang, R. Guo and J. A. Powell-Coffman, *Proceedings of the National Academy of Sciences*, 2001, **98**, 7916-7921.
21. R. Kamath, M. Martinez-Campos, P. Zipperlen, A. Fraser and J. Ahringer, *Genome Biology*, 2000, **2**, 1-10.
22. A. Larionov, A. Krause and W. Miller, *BMC bioinformatics*, 2005, **6**, 62.
23. M. C. K. Leung, P. L. Williams, A. Benedetto, C. Au, K. J. Helmcke, M. Aschner and J. N. Meyer, *Toxicological Sciences*, 2008, **106**, 5-28.
24. S. Lockery, *Nature Methods*, 2007, **4**, 691-692.
25. S. R. Lockery, K. J. Lawton, J. C. Doll, S. Faumont, S. M. Coulthard, T. R. Thiele, N. Chronis, K. E. McCormick, M. B. Goodman and B. L. Pruitt, *Journal of Neurophysiology*, 2008, **99**, 3136-3143.
26. X. Manière, F. Lebois, I. Matic, B. Ladoux, J.-M. Di Meglio and P. Hersen, *PLoS ONE*, 2011, **6**, e16637.
27. S. Pandey, A. Joseph, R. Lycke and A. Parashar, *Advances in Bioscience and Biotechnology*, 2011, **2**, 409-415.
28. A. Parashar, R. Lycke, J. Carr and S. Pandey, *Biomicrofluidics*, 2011, **5**, 024112.
29. J. A. Powell-Coffman, *Trends in Endocrinology & Metabolism*, 2010, **21**, 435-440.
30. J. Qin and A. R. Wheeler, *Lab on a Chip*, 2007, **7**, 186-192.
31. P. Rezai, S. Salam, P. R. Selvaganapathy and B. P. Gupta, *Lab on a Chip*, 2012, **12**, 1831-1840.
32. J. Sall, L. L. Creighton and A. Lehman, SAS Institute, Cary, NC, 2005.
33. SAS Institute, SAS/Stat 9.3, 2011, SAS Institute Inc.
34. Z. Shao, Y. Zhang and J. A. Powell-Coffman, *Genetics*, 2009, **183**, 821-829.

35. Z. Shao, Y. Zhang, Q. Ye, J. N. Saldanha and J. A. Powell-Coffman, PLoS Pathogens, 2010, **6**, e1001075.
36. C. Shen, D. Nettleton, M. Jiang, S. K. Kim and J. A. Powell-Coffman, Journal of Biological Chemistry, 2005, **280**, 20580-20588.
37. C. Shen, Z. Shao and J. A. Powell-Coffman, Genetics, 2006, **174**, 1205-1214.
38. C. Trent, N. Tsung and H. R. Horvitz, Genetics, 1983, **104**, 619-647.
39. S. Zuryn, J. Kuang and P. R. Ebert, Toxicological Sciences, 2008, **102**, 179-186.

Chapter 4

Discovering new combinations of existing drugs for parasitic worms

4.1 Abstract

The discovery of new drugs is often propelled by the increasing resistance of parasites to existing drugs and the availability of better technology platforms. As an alternative to finding new drugs and potential biological targets, we demonstrate the use of an algorithmic search method to find combinations of existing drugs that are more effective at killing *C. elegans* than individual drugs. The algorithmic search method is run through four iterations, each iteration having eight cocktails, to identify the drug combination producing the minimum average velocity of worms. Different cocktails of the four drugs (i.e. pyrantel, levamisole, tribendimidine, and methyridine) were tested. The final cocktail comprised levamisole and tribendimidine close to their EC_{50} values, while pyrantel and methyridine were at much lower concentrations. Further, we observed that levamisole and pyrantel produce similar behavioral traits in worms, methyridine causes a flailing action, and tribendimidine is crucial component of the final cocktail. Some of the behavioral differences were previously observed when we tested these drugs separately. Thus this study shows the feasibility of developing effective

combinations of existing drugs for nematodes as a faster alternative to cost-prohibitive, long-term discovery of new drugs.

4.2 Introduction

Anthelmintics are classes of compounds that have been developed and extensively studied for the treatment of intestinal nematodes.^{1,2} In the absence of available vaccines, anthelmintic chemotherapy is the preferred choice for control of intestinal infection in humans and livestock.^{3,4}

Two of these classes of drugs have been approved for use by the World Health Organization: benzimidazoles and nicotinic acetylcholine receptor (nAChR) agonists. The common benzimidazoles are mebendazole and albendazole.⁵ The nicotinic acetylcholine receptor agonists are grouped under two receptors subtypes they target: L-type and N-type.^{6,7} While levamisole and pyrantel are examples of L-type nAChR agonists, methyridine is an example of N-type nAChR agonist.^{8,9} Tribendimidine is relatively understudied and its mechanism of action is shown to be similar to levamisole and pyrantel.^{3,4} With slow progress in the discovery of new anthelmintics, parasitic worms have developed varying levels of resistance to these compounds.² In fact, multidrug resistance in parasitic worms has now become a prevalent global menace that continues to overwhelm basic research in chemotherapeutic agents.^{2,4}

Platforms to investigate the efficacy and resistance of anthelmintics are dependent on the choice of the biological host under study. *In vivo* animal assays are undoubtedly the best way to test parasitic worms in their natural growth

environment.^{10,11} These assays, however, require large quantities of the compounds, huge spaces to house the animals, long wait times, and thus higher research costs. Tests on smaller rodents such as mice and chicken are pragmatic but require about 100 mg of the chemical and are impractical for any large-scale random experiments with multiple chemicals. For these reasons, *in vitro* assays are the preferred choice in parasitology, especially for primary screening.^{5,11-13}

C. elegans is an established small animal model in parasitology for studying novel drug targets and modes of drug action.¹⁴⁻¹⁶ The relative ease of culturing *C. elegans* on agarose plates in standard laboratory conditions is in contrast to culturing parasitic worms that have complex life cycles. In this context, microfluidics has served as an enabling technology to study the effects of different drugs and toxins on single or multiple *C. elegans*. As seen in Chapter 1, microfluidic devices have integrated various techniques (e.g. droplet generation, automated valve operations, suction, image recognition, laser ablation) to demonstrate faster and high-throughput methods of sampling worms and observing drug effects. While these technological advancements are commendable, it is reasonable to state that almost all microfluidic-enabled drug studies on *C. elegans* are limited to tests on existing and commercially available drugs. In such studies, a dose response curve (i.e. worm survivability at different concentrations) is plotted showing the efficacy of the drug under study.^{17,18}

Are there other ways to characterize drug effects in these animals beyond using a dose response curve and will such ways help reveal useful behavioral information? We recently showed that the effect of a certain drug could change over the length of

experiment (as *C. elegans* is known to adapt to their environment) and quantifying the patterns of worm adaptation of the chemical environment could be used as a means to test different chemicals. In our study, four anthelmintics were chosen that act on the neuromuscular system of the *C. elegans*: pyrantel, levamisole, methyridine, and tribendimidine. The worms were exposed to the individual drugs in an electric field-based microfluidic device (Figure 1.5) and their activity was recorded for 40 minutes.

Upon initial drug exposure in the above device, an active worm showed three types of movement patterns: crawling, curling, and flailing. Crawling is the undulatory, sinusoidal movement of a worm that results in forward or backward locomotion. Curling occurs when the worm's head touches or overlaps its tail. Flailing happens when a worm oscillates its body in half waves about a fixed location, and is an unusual swimming-like behavior we observed in 0.8% agarose.

As time progresses during the exposure, a drug may cause an actively moving worm to show periods of being (partially or completely) immobilized before paralyzing its body. We grouped these immobilization patterns into three categories: being active, temporarily immobilized or permanently immobilized. From our definition, a worm is considered active (or actively moving) if its entire body is displaced from its original location within a given timeframe (1 second). A worm is permanently immobilized if its entire body remains stationary for at least 600 seconds, after which we denote the worm as being paralyzed. A worm is temporarily immobilized if parts of its body (and not the entire body) are still moving or if it can become active after being completely immobile for a certain time period (less than 600 seconds).

We characterized these behavioral changes by a set of parameters and compared the results among the four drugs. The parameters we extracted were curls per second, types of paralyzation, mode frequency, and number/duration of active/immobilization cycles. We found that a single parameter was unable to capture the overall drug effects through the experimental period. Three key observations after data analysis are: Pyrantel is more effective than levamisole in immobilizing the worms at the end of the 40-minute experiments. In tribendimidine, worms display shorter number of active cycles before permanently immobilizing than in pyrantel or levamisole. In methyridine, worms exhibit a swimming-like movement that is different from the normal crawling movement in pyrantel, levamisole, and tribendimidine. Our results suggested the following: methyridine acts on a different subtype of nAChR receptors than the other three anthelmintics, the action of pyrantel and levamisole is similar but pyrantel is more effective than levamisole, and tribendimidine is more potent than pyrantel or levamisole in causing an irreversible paralysis of the worms. In our view, this multi-parameter extraction method of *C. elegans* paralysis expands the repertoire of phenotypic characterization tools available in existing drug-based microfluidic devices.

While developing reliable characterization techniques for screening existing compounds is important, multidrug resistance in parasites is now recognized as the biggest challenge in parasitology.^{1,2,4} The conventional notion of finding new drugs or drug targets using biological assumptions is considered impractical for reasons of long drug development time, large capital needed, and incomplete or unknown genome of

most parasites. Because of these reasons, there are no new drugs in the market today targeting nematodes that have developed resistance to multiple drugs.

We hypothesized that a certain combination of the abovementioned four drugs, used at lower concentrations than their EC₅₀ values, could be more effective at killing *C. elegans* than the individual drugs (used at their EC₅₀ values). Our hypothesis was driven by our previous experiments with individual drugs.³¹ We saw that worms had a tendency to flail in methyridine and would paralyze after a longer times than in the other three drugs. This hinted that the eventual cocktail may require minimal or no presence of methyridine. In addition, levamisole and pyrantel had similar effects, even though pyrantel was slightly more effective than levamisole. This indicated that the eventual cocktail may not require equal concentrations of both levamisole and pyrantel, and the presence of one may be sufficient. Tribendimidine was the most effective in paralyzing worms, often within 2-3 active cycles. This suggested that the presence of tribendimidine may be important in the eventual cocktail. The above assumptions have no concrete biological basis as each drug may have multiple target receptors or receptor subtypes. It would be very difficult to predict specific target sites when a cocktail composed of multiple drugs is ingested by the animal.

Our UCLA collaborator, Dr. Chih-Ming Ho, has developed a unique feedback system control (FSC) scheme to identify the most effective cocktail of chemicals used in any experiment having multiple variables (i.e. concentrations of individual chemicals, number of chemicals).¹⁹⁻²² We adopted this technique for screening *C. elegans* with cocktails of the four drugs. Through four iterations, each having eight cocktails, the FSC

scheme gave us an optimized, effective cocktail that used lower concentrations of each of the four drugs. We show that, in contrast to testing several random cocktails, this directed algorithmic search led us to the desired result within a reasonable timeframe.

4.3 Materials and methods

The microfluidic device is similar to the cyanide-testing device discussed in Chapter 3.²³ Each cocktail under test is prepared to a pre-specified concentration and filled in the drug well. A Leica MZ16 stereozoom microscope is connected with a high-speed QImaging camera for real-time recording of worm behavior in the drug well. The QCapture software is programmed to record grayscale images of the drug well (every second) for a period of 600 seconds. Subsequently, the images are stitched into a single .avi file for data analysis. All experiments are conducted multiple times ($N \geq 5$). Each experiment is run on three parallel devices, each having a single worm. With every cocktail test, control experiments are conducted simultaneously. Statistical analysis is performed using the GraphPad Prism software.

4.4 Results

4.4.1 Iterations of algorithmic search

To test the applicability of FSC scheme for searching an effective combination of four drugs used, we used the previously described cyanide-testing microfluidic device (Chapter 3).²³ Different concentrations of each of the four drugs were tested separately and the dose responses are plotted in [Figure 4.1](#). The performance of a drug concentration is estimated by measuring the average velocity of body centroid and

normalizing it to the average velocity in M9 buffer (i.e. percentage response). Details of the tracking and method to calculate the average velocity are described in Chapter 3.²³ The EC_{50} values (i.e. drug concentration where the average velocity drops to 50% of the value under control conditions) of individual drugs are listed in the Figure 4.1. We see that levamisole has the lowest EC_{50} value (2.23 μM) while methyridine has the highest EC_{50} value (1672 μM). Under two drug environments, percentage response was above 100% as worms were hyper active and exhibited higher average velocity than under control conditions.

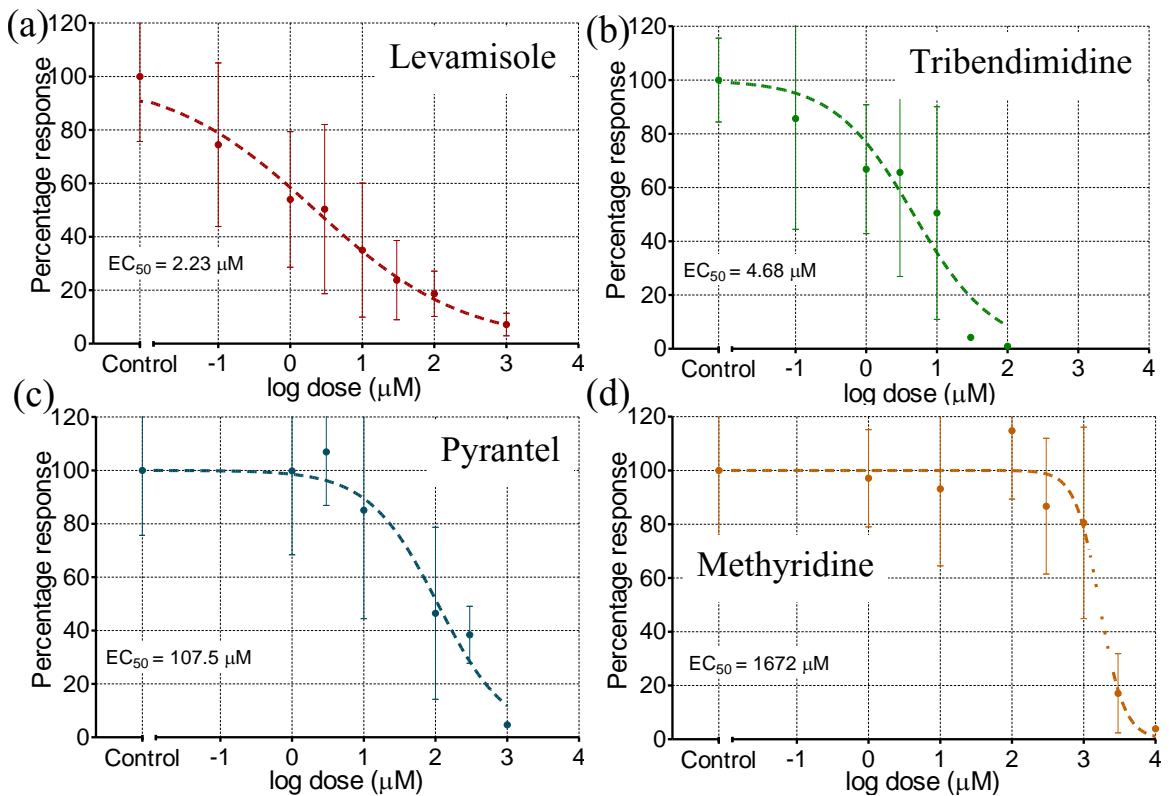


Figure 4.1 Percentage response of worms in the four drugs. (a) levamisole, (b) tribendimidine, (c) pyrantel, and (d) methyridine is plotted. Worm percentage response is calculated by extracting the average velocity and normalizing it to the average velocity under control conditions. EC_{50} values or the concentrations where the average velocity drops to 50% of control values are listed for each drug.

After characterizing the dose response of individual drugs, we chose six concentration keys for each drug. Rather than using actual concentrations as input, the FSC algorithm requires user input as concentration keys to determine subsequent cocktails during each run.¹⁹⁻²¹ To choose actual concentrations that would denote concentration keys, we follow the following steps. The highest concentration key is near the EC₅₀ value of the drug under test. Each subsequent lower concentration key is chosen to correspond to half the current concentration. Our goal is to arrive at an effective cocktail that uses minimal concentrations of each drug but still produces better results (i.e. lowest average velocity) than individual drugs (at their EC₅₀ concentrations). [Table 4.1](#) illustrates the respective color codes for different concentrations and their corresponding concentration keys. The same color codes are used in the next figure to illustrate the drug combinations during each iteration.

Table 4.1 Concentration keys and color codes corresponding to each drug concentration that is later used in the different cocktails predicted by the FSC algorithm.

Levamisole	concentration key	0	1	2	3	4	5
	concentration	0 μ M	0.125 μ M	0.25 μ M	0.5 μ M	1 μ M	2 μ M
	color code						
Tribendimidine	concentration key	0	1	2	3	4	5
	concentration	0 μ M	0.25 μ M	0.5 μ M	1 μ M	2 μ M	4 μ M
	color code						
Pyrantel	concentration key	0	1	2	3	4	5
	concentration	0 μ M	6.25 μ M	12.5 μ M	25 μ M	50 μ M	100 μ M
	color code						
Methyridine	concentration key	0	1	2	3	4	5
	concentration	0 μ M	100 μ M	200 μ M	400 μ M	800 μ M	1600 μ M
	color code						

For the first iteration, all concentration keys are entered into the FSC program and the algorithm outputs eight random combinations (P1 through P4 and T1 through T4). This is shown in Figure 4.2. Each drug cocktail is prepared and tested on single worms (with at least five repeats). The average velocity of worms in each drug experiment is calculated and normalized to the average velocity of worms in M9 buffer. This performance parameter, normalized average velocity, for the eight cocktails is fed back into the FSC program to produce the next set of eight cocktails to be tested in the next iteration. Figure 4.2 illustrates this iterative process through the four iterations we tried. For each new iteration, the performance of P versus T (P1 with T1, P2 with T2, and so on) is compared and the better-performing four cocktails from previous iteration are kept as new P1 through P4. This information is fed in the FSC program which then suggests four new cocktails (mutants of P1-P4) that are entered as T1 through T4.

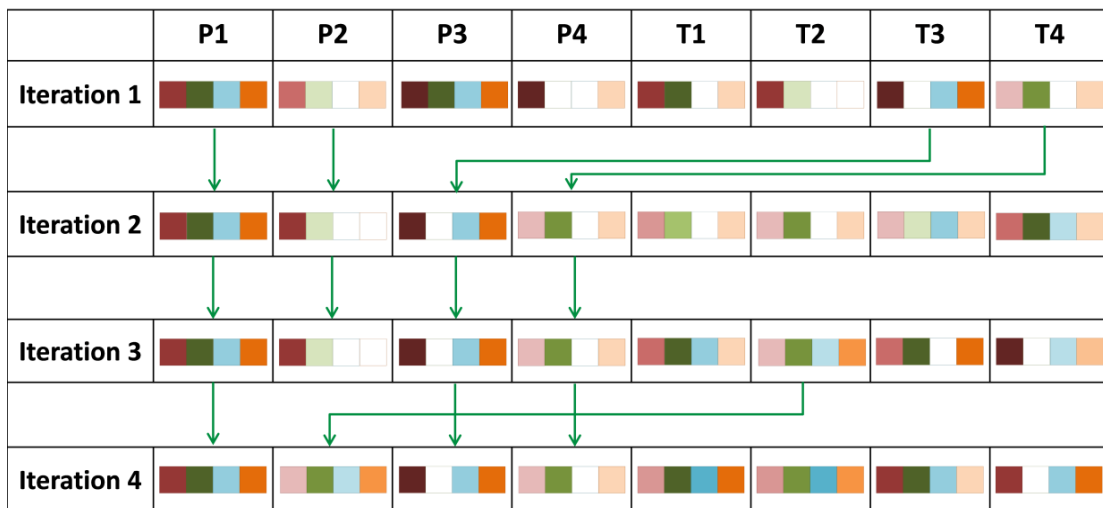


Figure 4.2 Each iteration has eight cocktails to be tested. Color codes of cocktails refer to the concentration keys used in each case. Experiments were conducted through four iterations.

4.4.2 Performance of different cocktails

To verify whether average velocity is an accurate measure of the worm's inhibition in drug environment, we calculated three parameters: (a) The instantaneous velocity was averaged over the entire length of the experiment (i.e. 600 seconds) and is plotted in [Figure 4.3](#). The performance of every cocktail through the four iterations is represented by a mean and standard deviation. In the first iteration, cocktails were randomly selected. The second iteration does not produce any cocktail that is better than those in the first iteration. The fourth iteration produces a cocktail having an average velocity below 15 $\mu\text{m/s}$, which is near the threshold of detection by the tracking software (Section 1.5). This cocktail is concluded to be our most effective drug combination. (b) The instantaneous velocity was averaged in the last 120 seconds and is plotted in [Figure 4.4](#). We notice that the performance trends here are similar to those found while averaging the velocity over the entire experimental time. In our view, the averaged velocity in the last 120 seconds is a better representation of the drug effect. The worm velocity within the first one-two minutes may show randomness as the worm is getting accustomed to the drug environment. This randomness fades away after a few minutes. (c) The total distance travelled by single worms is calculated and plotted in [Figure 4.5](#). Again, the performance trends are similar to those obtained from averaging the velocity. Intuitively, it may appear that total distance travelled and the average velocity are directly related. But, under hypothetical situations, these two parameters may differ: it may happen that a worm rests and shows sudden bursts of high velocity. However, in our experiments, we rarely encountered such cases. Plotting the total distance travelled is

thus to confirm that no unusual events occurred during worm movement and the performance trends are similar to those in the velocity plots (Figure 4.3 and 4.4).

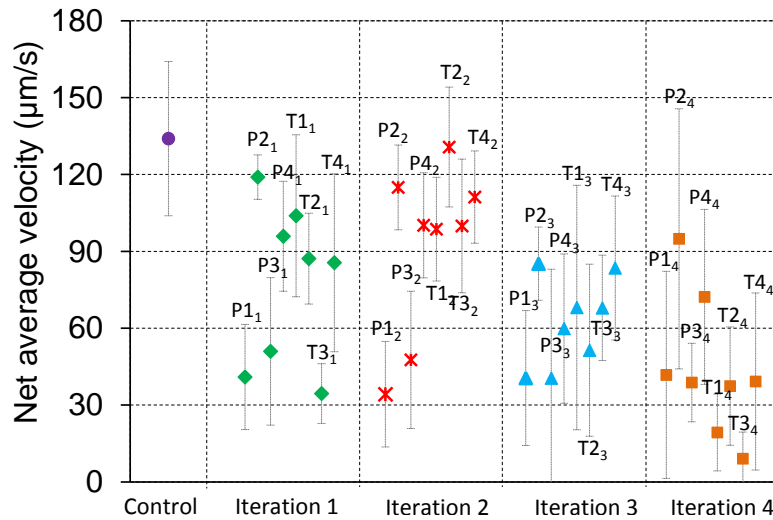


Figure 4.3 The velocity of body centroid is averaged over 600 seconds and is plotted for every cocktail through the four iterations. The fourth iteration produces a cocktail that is most effective.

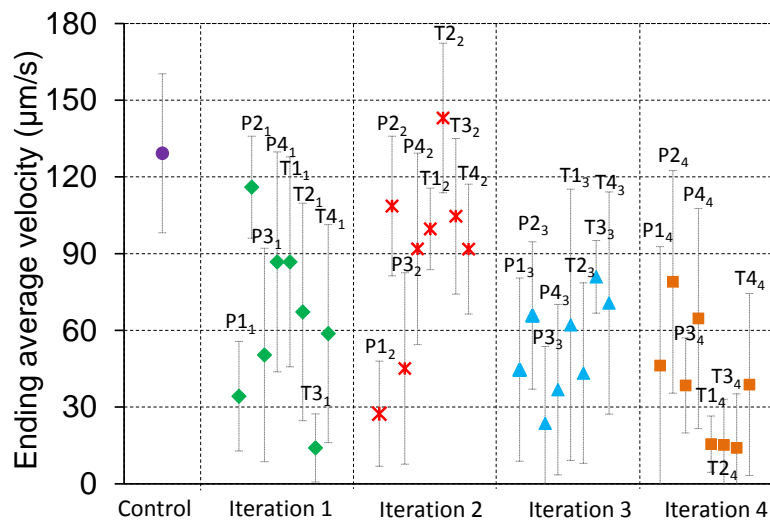


Figure 4.4 The velocity of body centroid is averaged over the last 120 seconds of the entire experimental time (i.e. 600 seconds). The fourth iteration shows three cocktails with least average velocity.

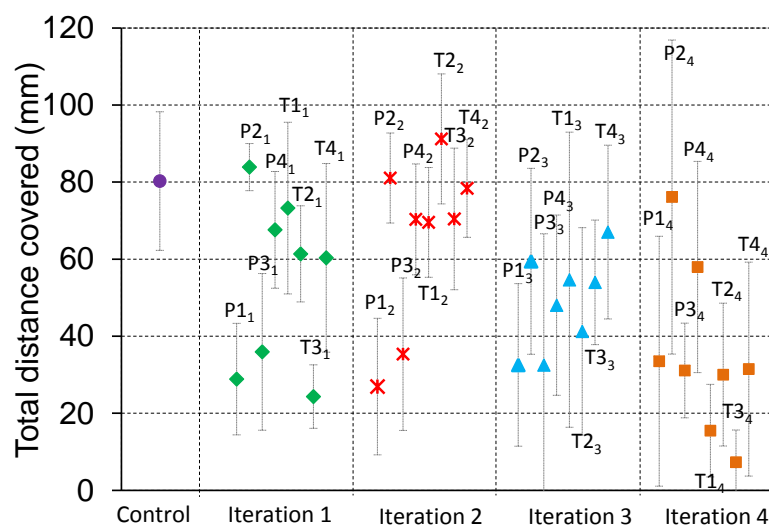


Figure 4.5 The total distance travelled by individual worms is calculated over the entire length of 600 seconds. The fourth iteration produces a cocktail where worms travel the least distance.

Besides evaluating the performance of each cocktail using the average velocity or total distance travelled, we investigated whether we could predict the efficacy of cocktails from any other information. To our advantage, our experiments with real-time imaging produced velocity data for every second of worm movement. The nature of average velocity over 600 seconds follows distinct patterns that can be broadly grouped into four categories, as shown in [Figure 4.6](#). The first group represents worms that show normal or hyper activity in the drug environment and have a steady average velocity above $150 \mu\text{m/s}$. These drug cocktails were least effective. The second group represents worms that show significant decrease in average velocity (below $70 \mu\text{m/s}$) through the experimental time. These drugs had the potential of being suitable candidates in the FSC algorithm. The third group represents worms that started with a normal/higher average velocity (around $150 \mu\text{m/s}$ for over 60 s) and slowed towards the end of the experiment (around $100 \mu\text{m/s}$). The last group comprised worms that started with a normal/higher

average velocity but showed an exponential decay in their velocities to values below 70 $\mu\text{m/s}$. The third and fourth groups were not effective candidates. Thus, observing the nature of average velocity could indicate the effectiveness of a drug cocktail. Worms put in the final effective cocktail (shown as a red-boxed plot, T3₄) showed lowered average velocity almost from the instance they enter the drug environment.

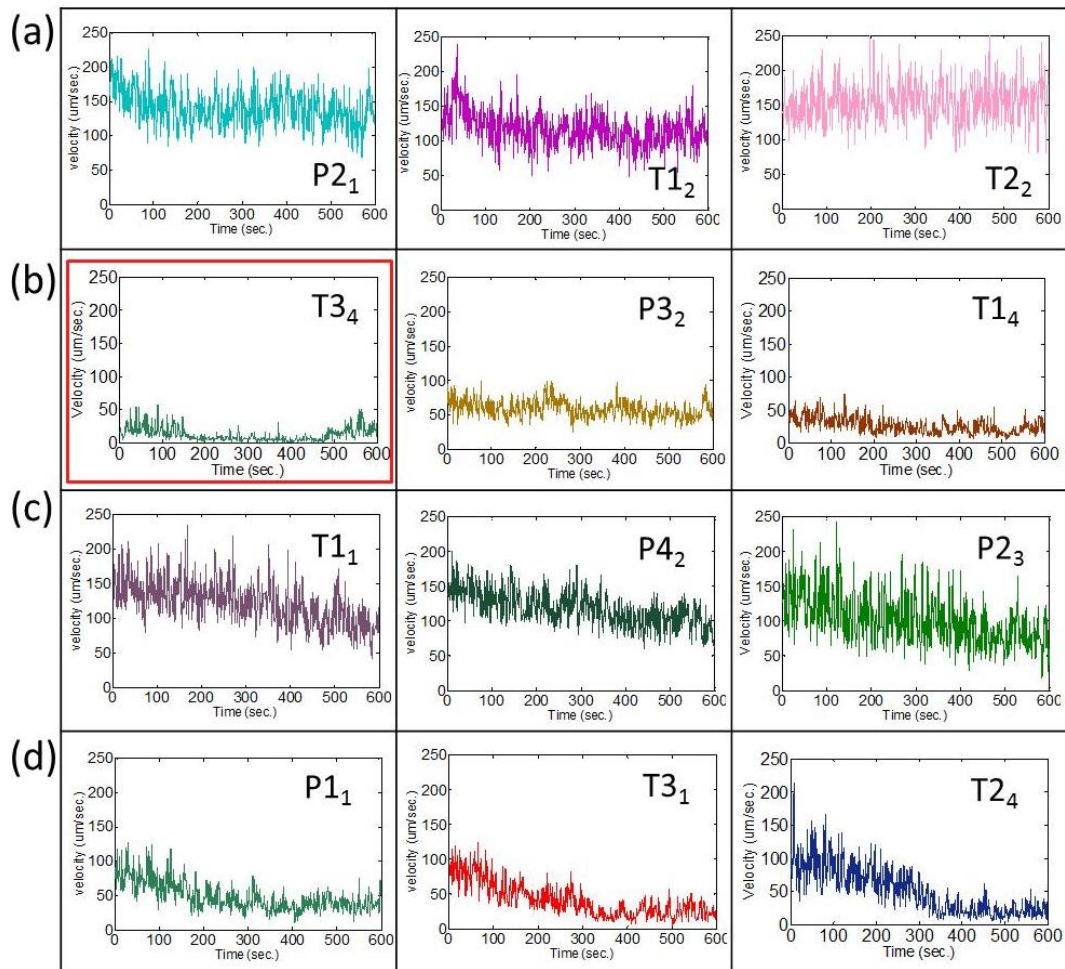


Figure 4.6 Instantaneous average velocities of worms in different cocktails can be grouped into four categories. The most effective cocktails were those in which worms exhibited dramatically reduced velocities throughout the length of the experiment (group (b)).

4.5 Discussion

We demonstrated the use of an algorithm to search for effective drug combinations using four existing drugs. A microfluidic device with real-time imaging was used to quantify the effects of drug exposure on *C. elegans*. By measuring three motility parameters (i.e. centroid velocity averaged over 600 seconds or averaged over last 120 seconds and the total distance travelled), we showed the performance of 36 different drug cocktails. The relative performances of the cocktails were similar in the three motility parameters. The winning cocktail had the concentration keys of the four drugs as [4, 5, 2, 1]. To the best of our knowledge, such an algorithmic search method has not been demonstrated in the available literature. We feel that the microfluidic technology presented here, being a short-term, reliable drug screening platform, will enlighten our understanding of worm behavior in the presence of drugs and unravel new biological phenomena that were not possible with traditional inhibition assays.²⁴⁻²⁸ Even though we investigated the behavioral changes in worm motility, additional biophysical studies need to be performed to verify the effectiveness of the winning cocktail. In this context, we verified the winning cocktail by droplet tests on worms, compared the results with control solutions, and observed that the drug effects were similar to those in microfluidic devices. Electrophysiological tests on targeted ion channels could reveal the precise modes of action of the winning cocktail.^{6,7,29}

We observed that pyrantel and levamisole may produce similar phenotypes in worms. In cocktails having similar concentrations of both pyrantel and levamisole, an active worm moves in a sinusoidal manner with periods of immobilization where it curls

its body and eventually paralyzes. The average time spent in each active cycle is similar in both cases and markedly distinct compared to those cocktails having higher concentrations of methyridine and tribendimidine. The inherent similarities between movement phenotypes in pyrantel and levamisole do suggest that these drugs act on the same subtype of nAChR receptors (i.e. L-subtype).^{8,9,30} There are some differences between pyrantel and levamisole. The average time spent in each immobilization cycle is longer in pyrantel than in levamisole. An active worm in pyrantel prefers to rest longer, curl up or move less often; whereas an active worm in levamisole spends similar time durations being active or resting/curling. These differences suggest that pyrantel may be more effective than levamisole.

It has been shown that tribendimidine affects *C. elegans* using the same pathway as levamisole and hence belong to the same class of L-subtype.^{3,4} Since these three anthelmintics have the same mechanism of action, should we expect differences in the patterns of paralysis? In general, we observed that the behavior of *C. elegans* paralysis is similar in the three drugs: an active worm moves in a sinusoidal manner with periods of immobilization where it curls its body and eventually paralyzes. One key difference is that the number of active cycles is much reduced in tribendimidine compared to those in levamisole or pyrantel. This may indicate that tribendimidine is more effective at a single dose than levamisole or pyrantel. In addition, the increased number of active cycles observed in levamisole and pyrantel may indicate that worms could recover from the drug exposure, if given at low concentrations with sufficient recovery time. Hence, we feel that tribendimidine is important in increasing the effectiveness of the drug

cocktail. The cocktails in which tribendimidine was missing (or in low concentrations) were not able to inhibit worm movement as effectively as the winning cocktail.

In cocktails with higher concentrations of methyridine, worms exhibited a swimming-like motion where the body formed half waves during moving and thrashed along in the drug well. Occasionally, the worms would thrash about a fixed location (that we defined as flailing) and then continue their swimming-like motion. In all cases with higher concentrations of methyridine, worms remained active and did not reduce their average velocity to an extent as exhibited in the winning cocktail. Considering that methyridine acts on the same nAChR receptor, our observed difference in movement could suggest that this drug acts on a different subtype of nAChR receptor. This assumption is in line with previous studies showing that methyridine target N-subtype nAChR receptors and not the L-subtype nAChR receptors.⁸

4.6 Conclusion

An algorithmic search method is used to find the most effective cocktail of four existing drugs using worm motility as a performance indicator. Microfluidic devices, along with real-time imaging and tracking, are employed to characterize the dose responses of the individual drugs. Subsequently, the algorithm proposes eight random cocktails during the first iteration. Based on the worms' performance in the first iteration, new cocktails are proposed in the next three iterations. In our case, the fourth iteration produces the winning cocktail where worm motility is significantly decreased within detection limits of the tracking software. The winning cocktail comprises all the four drugs, each at a concentration below their EC_{50} values. To show the broader

applicability and adoptability of this method towards testing other anthelmintics, we decreased the experimental time to 10 minutes, incorporated computer-controlled data analysis, and verified the results using different motility parameters. In addition, the method could complement rigorous electrophysiological experiments to rapidly test screen compounds against nematodes, establish suitable drug candidates, and predict the class of target receptor subtypes.

4.7 References

1. D. O. Connell, *Nature Reviews Microbiology*, 2006, **4**, 568-569.
2. R. Kaminsky, P. Ducray, M. Jung, R. Clover, L. Rufener, J. Bouvier, S. S. Weber, A. Wenger, S. Wieland-Berghausen, T. Goebel, N. Gauvry, F. Pautrat, T. Skripsky, O. Froelich, C. Komoin-Oka, B. Westlund, A. Sluder and P. Maeser, *Nature*, 2008, **452**, 176-U119.
3. Y. Hu, E. G. Platzer, A. Bellier and R. V. Aroian, *Proceedings of the National Academy of Sciences*, 2010, **107**, 5955-5960.
4. Y. Hu, S. H. Xiao and R. V. Aroian, *PLoS Neglected Tropical Diseases*, 2009, **3**, e499.
5. V. Leignel, A. Silvestre, J. F. Humbert and J. Cabaret, *Veterinary Parasitology*, 2010, **172**, 80-88.
6. H. Qian, R. J. Martin and A. P. Robertson, *The FASEB Journal*, 2006, **20**, 2606-2608.
7. H. Qian, A. P. Robertson, J. A. Powell-Coffman and R. J. Martin, *The FASEB Journal*, 2008, **22**, 3247-3254.
8. R. J. Martin, G. X. Bai, C. L. Clark and A. P. Robertson, *British Journal of Pharmacology*, 2003, **140**, 1068-1076.
9. R. J. Martin and A. P. Robertson, *Parasitology*, 2007, **134**, 1093-1104.
10. W. D. Atchison, T. G. Geary, B. Manning, E. A. VandeWaa and D. P. Thompson, *Toxicology and Applied Pharmacology*, 1992, **112**, 133-143.

11. S. Gaba, J. Cabaret, C. Sauve, J. Cortet and A. Silvestre, *Veterinary Parasitology*, 2010, **171**, 254-262.
12. F. Beugnet, D. Kerboeuf, J. C. Nicolle and D. Soubieux, *Veterinary Parasitology*, 1996, **63**, 83-94.
13. H. Bjørn, A. Roepstorff, P. J. Waller and P. Nansen, *Veterinary Parasitology*, 1990, **37**, 21-30.
14. J. E. Richmond and E. M. Jorgensen, *Nature Neuroscience*, 1999, **2**, 791-797.
15. E. Ruiz-Lancheros, C. Viau, T. N. Walter, A. Francis and T. G. Geary, *International Journal for Parasitology*, 2011, **41**, 455-461.
16. K. G. Simpkin and G. C. Coles, *Journal of Chemical Technology and Biotechnology*, 1981, **31**, 66-69.
17. W. Shi, J. Qin, N. Ye and B. Lin, *Lab on a Chip*, 2008, **8**, 1432-1435.
18. W. Shi, H. Wen, Y. Shi, B. Lin and J. Qin, *Lab on a Chip*, 2010, **10**, 2855-2863.
19. I. Al-Shyoukh, F. Yu, J. Feng, K. Yan, S. Dubinett, C. M. Ho, J. Shamma and R. Sun, *BMC Systems Biology*, 2011, **5**, 1-17.
20. X. Ding, D. J. Sanchez, A. Shahangian, I. Al-Shyoukh, G. Cheng and C. M. Ho, *International Journal of Nanomedicine*, 2012, **7**, 2281-2292.
21. X. Ding, H. Xu, C. Hopper, J. Yang and C. M. Ho, *Quality and Reliability Engineering International*, 2013, **29**, 299-304.
22. H. Tsutsui, B. Valamehr, A. Hindoyan, R. Qiao, X. Ding, S. Guo, O. N. Witte, X. Liu, C. M. Ho and H. Wu, *Nature Communications*, 2011, **2**, 167.
23. J. N. Saldanha, A. Parashar, S. Pandey and J. A. Powell-Coffman, *Toxicological Sciences*, 2013, **135**, 156-168.
24. L. A. Brown, A. K. Jones, S. D. Buckingham, C. J. Mee and D. B. Sattelle, *International Journal for Parasitology*, 2006, **36**, 617-624.
25. K. Chung, M. M. Crane and H. Lu, *Nature Methods*, 2008, **5**, 637-643.
26. C. E. James and M. W. Davey, *International Journal for Parasitology*, 2009, **39**, 213-220.

27. P. Steinmann, X. N. Zhou, Z. W. Du, J. Y. Jiang, S. H. Xiao, Z. X. Wu, H. Zhou and J. Utzinger, PLoS Neglected Tropical Diseases, 2008, **2**, e322.
28. S. H. Xiao, W. Hui-Ming, M. Tanner, J. Utzinger and W. Chong, Acta Tropica, 2005, **94**, 1-14.
29. S. R. Lockery, S. E. Hulme, W. M. Roberts, K. J. Robinson, A. Laromaine, T. H. Lindsay, G. M. Whitesides and J. C. Weeks, Lab on a Chip, 2012, **12**, 2211-2220.
30. R. J. Martin, C. L. Clark, S. M. Trailovic and A. P. Robertson, International Journal for Parasitology, 2004, **34**, 1083-1090.
31. R. Lycke, Graduate Theses and Dissertations, 2012, Paper 12972, Iowa State University.

Chapter 5

Plant-in-chip: Microfluidic system for studying root growth and pathogenic interactions in *Arabidopsis*

*Modified from a paper published in Applied Physics Letters
Archana Parashar and Santosh Pandey*

5.1 Abstract

In this chapter, we describe a microfluidic platform for the hydroponic growth of *Arabidopsis* plants with high-resolution visualization of root development and root-pathogen interactions. The platform comprises a set of parallel microchannels with individual input/output ports where 1-day old germinated seedlings are initially placed. Under optimum conditions, a root system grows in each microchannel and its images are recorded over a 198-hour period. Different concentrations of plant growth media show different root growth characteristics. Later, the developed roots are inoculated with two plant pathogens (nematodes and zoospores) and their interactions with the live root systems are observed.

5.2 Introduction

Plant development is greatly dependent upon its interactions with the environment which may present challenges to its sessile lifestyle.¹ On one hand, plants

need to search for essential resources as light, water, and nutrients.^{1,2} On the other hand, they need to compete with neighboring plants for limited resources and defend themselves against soil-borne pathogens.³⁻¹¹ In this context, the root system has been well-studied for elucidating the role of different genes,^{2,7} proteins,^{1,6} and phytohormones^{1,8} in the plasticity of root development.¹² A number of important revelations have come to light from root studies such as how plants regulate organ growth rates,¹¹ foraging responses,⁹ defense mechanisms,⁶ and cell cycle machinery.¹⁰ Observations of behavioral adaptability of root systems and associated genotype are providing insights into key biophysical and biochemical processes in plants (e.g. synthesis and transport of enzymes,⁷ cell production and expansion in growing tissues,^{10,11} nutrient sensing and transduction,⁷ search and navigation strategies,⁸ and evolution of phyllotactic patterns^{13,15}) and the varied interrelationships (both symbiotic and parasitic)^{3,4} they establish with their surroundings.

In the past three decades, several techniques were developed to study root development of the model plant, *Arabidopsis thaliana*. Besides being the first plant system to be fully sequenced, *Arabidopsis* has been exploited for its smaller size, ever increasing database of genetic information, and the relative ease of screening mutants.¹⁻³ Most studies on root development were based on genetic analysis because of the difficulty of characterizing root growth in soil pots.⁸ For real-time observation of root architecture, agarose plates have been used to grow *Arabidopsis* plants with controlled local environments.^{13,15-20} However, such experiments on agarose plates have limited spatial resolution (in the millimeter range) and throughput (one experimental condition

per plate).^{13,21} Recently, a microfluidic device with multi-laminar flow was demonstrated to chemically stimulate a 10-20 μm section of a live *Arabidopsis* root, showing the possible advantages of improved spatial and temporal resolution.²¹ In their work, *Arabidopsis* seeds were germinated, grown on agarose plates for 7 or 11 days, and then transferred to open microchannels in a PDMS mold.^{22,23} Subsequently, three converging laminar streams were flowed in the device to observe the effects of localized chemical stimulation on auxin transport and root hair growth over a 24-hours period.²¹

5.3 Material and Methods

We hypothesized that germinated *Arabidopsis* seedlings could be directly sown in microfluidic ports connected to microchannels filled with a suitable growth medium (Figure 5.1). Under optimum hydroponic growth conditions,²⁴ the shoots would grow upwards while the roots would grow into the microchannels. This could possibly allow the observation of growth kinetics of multiple roots over long time periods with the flexibility of testing plant responses to various abiotic and biotic stresses.

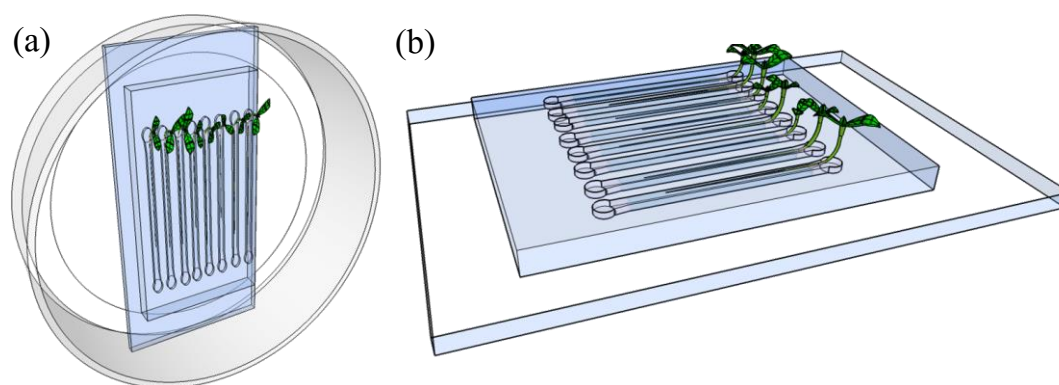


Figure 5.1 Schematic of the microfluidic device and experimental setup. **(a)** Eight parallel microchannels are fabricated with ports for housing seedlings and inoculation of pathogens. **(b)** Side view of the device illustrating the growth of *Arabidopsis* roots in microchannels.

Building on this hypothesis, we present a method of growing germinated *Arabidopsis* (*Col-0*) seedlings in a microfluidic platform. The device comprises eight parallel straight microchannels (length = 1 cm, width = 350 μm , height = 80 μm), each with its individual input and output ports (diameter = 2 mm). Standard soft lithography²² is used to fabricate the PDMS device from SU-8 master mold, which is then bonded to a microscope glass slide (75 mm \times 25 mm \times 0.2 mm). The microchannels are connected with thin vertical side channels (length = 750 μm , width = 25 μm , height = 80 μm) to allow the application of chemicals and pathogens in the entire chip. *Arabidopsis* seeds are surface sterilized by treating in 5% sodium hypochlorite solution followed by washing three times with distilled water and putting at 4°C for 48 hours to synchronize germination.¹² After germination, seeds are transferred to half-strength Murashige and Skoog (MS) media and incubated at 23°C for 24 hours.¹² The microchannels are filled with a pre-specified growth medium. Each seedling is hand-picked using sterile forceps and placed in individual input ports. The chip is put in a petri dish having a moist wick (tissue paper) which is later sealed (with a parafilm) and punched with perforations for ventilation. The petri dish is placed in a near vertical position under constant white light intensity (approximately 80-100 $\mu\text{E m}^{-2} \text{s}^{-2}$) at 23°C.²⁴ Individual root systems in the entire chip are monitored and imaged for 198 hours.

5.4 Results and discussion

5.4.1 Characterization of root growth parameters

Figure 5.2 shows the growth parameters of *Arabidopsis* roots measured in four different fluid media (deionized (DI) water, 10% MS, 25% MS, and 50% MS). The

transparent microfluidic chip is particularly useful in high-magnification imaging and analysis of root structures. The root length (L) is calculated as the distance from the root tip to the root apex and is measured for 198 hours of growth time (Figure 5.2).

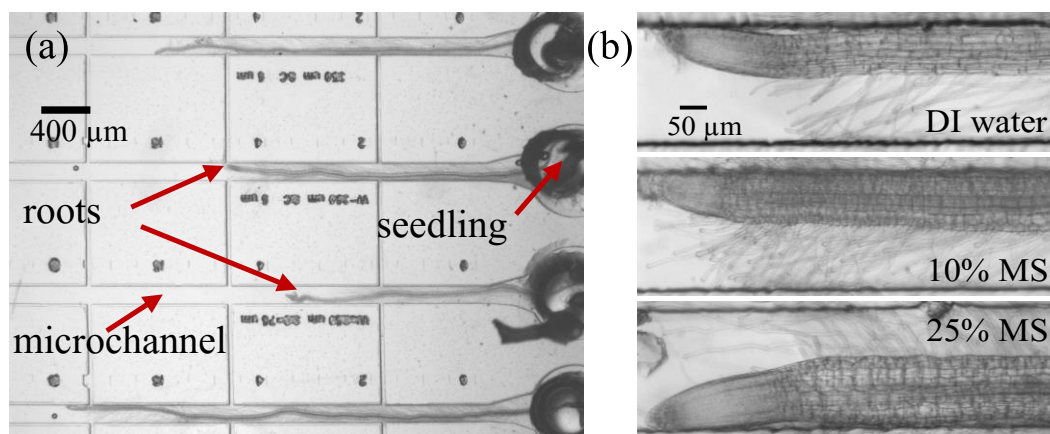


Figure 5.2 Snapshot of multiple *Arabidopsis* roots growing in the microchannels. **(a)** The image is taken after 60 hours of planting the seedlings in the input ports. **(b)** The root tip (at the end of the growth period) grown in DI water, 10% MS and 25% MS media.

All data are shown as mean \pm SD. In DI water, the growth rate ($55 \pm 9 \mu\text{m/hr}$) is steady during this time period. In 10% MS, 25% and 50% MS, the growth rate is higher in the first ~ 53 hours ($42 \pm 17 \mu\text{m/hr}$, $29 \pm 17 \mu\text{m/hr}$, $13 \pm 3 \mu\text{m/hr}$, respectively) and becomes slower at later times ($12 \pm 6 \mu\text{m/hr}$, $6 \pm 2 \mu\text{m/hr}$, $3 \pm 3 \mu\text{m/hr}$, respectively). At the end of the growth period, the roots in DI water are significantly longer ($L = 9345 \pm 901 \mu\text{m}$) and thinner than those in 10% MS ($L = 4063 \pm 450 \mu\text{m}$), 25% MS ($L = 2689 \pm 589 \mu\text{m}$) or 50% MS media ($L = 1275 \pm 54 \mu\text{m}$).

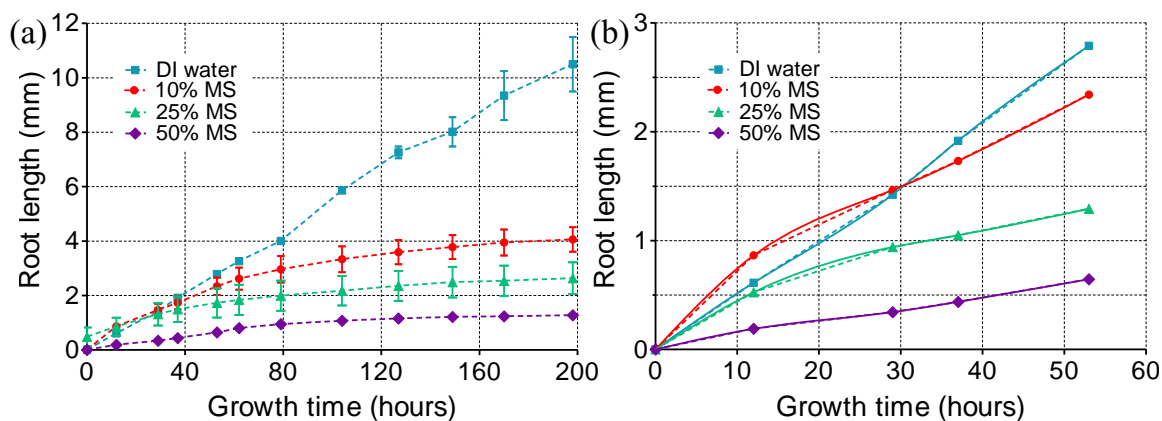


Figure 5.3 Root growth parameters measured during hydroponic growth of the *Arabidopsis* plants in the microfluidic device with different concentrations of growth media. **(a)** Root length versus growth time measured through 198 hours. **(b)** Root length versus growth time measured through the initial 53 hours showing the growth trends during the initiation phase.

Furthermore, root hairs are thinner and longer in DI water compared to those in 25% and 50% MS media. This observation is in agreement with current literature that suggests that root systems are short, compact and densely branched in nutrient-rich growth media (e.g. 50% MS), while they are long, thin, and sparsely branched in more dilute media (e.g. DI water).^{25,26} In addition, the root diameter (Figure 5.4a) and cell length (Figure 5.4b) are measured along the root (for up to 4 mm from the root tip) at the end of the growth period. In each media, the diameter is roughly uniform throughout the root length (DI water: $101 \pm 9 \mu\text{m}$, 10% MS: $154 \pm 11 \mu\text{m}$, 25% MS: $112 \pm 6 \mu\text{m}$).

However, there is significant difference between the root thicknesses measured in different growth media ($p < 0.0001$). The cell length is smaller close to the root tip (DI water: $22 \pm 3 \mu\text{m}$, 10% MS $13 \pm 6 \mu\text{m}$, 25% MS $28 \pm 4 \mu\text{m}$) and larger towards the root apex (DI water: $79 \pm 17 \mu\text{m}$, 10% MS $33 \pm 6 \mu\text{m}$, 25% MS $56 \pm 5 \mu\text{m}$).

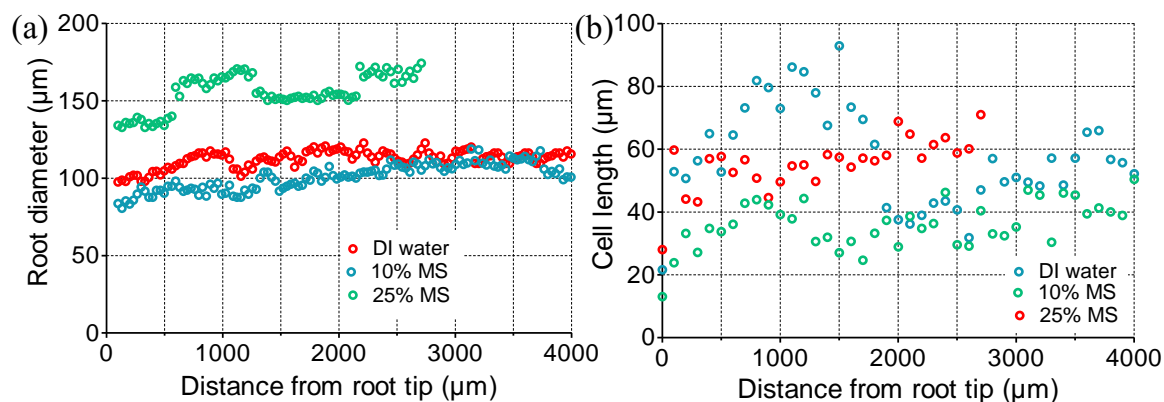


Figure 5.4 Measurements of root diameter and cell length. **(a)** Root diameter and **(b)** cell length along the root (for the first 4 mm from root tip) measured through 198 hours.

5.4.2 Imaging root-pathogen interactions

Besides root development, we show that the microfluidic platform is useful for studying root-pathogen interactions. Both nematodes (e.g. Sugar beet nematodes (SBNs)) and oomycetes (e.g. *Phytophthora sojae*) are known to establish relationships with numerous plants, resulting in several economically important diseases.²⁷⁻³²

Currently, functional genomic strategies of plant pathosystems,²⁷ along with microarray analyses and PCR techniques,³¹ are providing exciting leads into the role of specific genes in establishing biotrophic parasitism.^{3,4,8} It is, however, difficult to visually observe early interactions between pathogens and root systems with real-time imaging.²⁸⁻³⁰ We inoculated the developed roots in the microchannels with two pathogens: SBN and *P. sojae*. Image recordings were taken every 24 hours for the next 4 days. Upon inoculation, the SBNs migrated through the microchannels and found their way to the roots within the first 1-2 hours. Subsequently, they probed the root surface along its length and started penetrating the cell layers in the next 12 hours (Figure 5.5a).

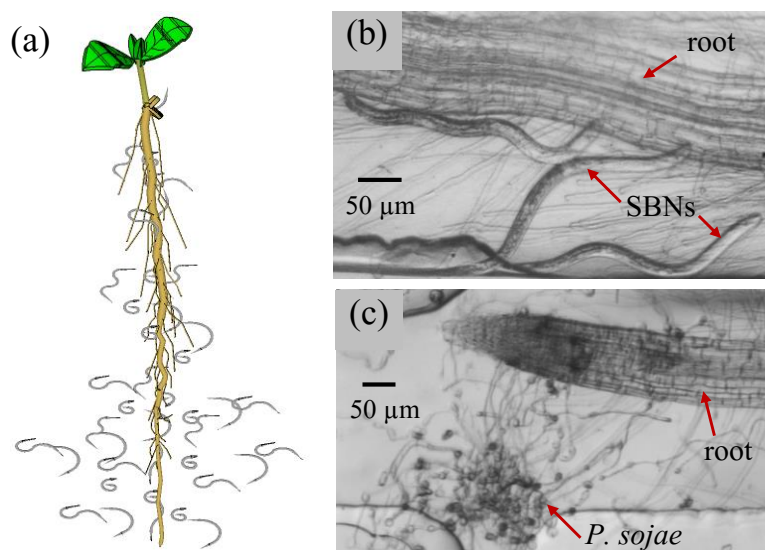


Figure 5.5 Interactions between the *Arabidopsis* roots grown in microfluidic device with two plant pathogens. **(a)** Schematic of plant-pathogen interaction **(b)** Sugar beet nematodes, inoculated 2 hours before, are probing the root surface. Later, some of them find their way to the root center and use their stylus to draw nutrients from the root. **(c)** *P. sojae* zoospores, inoculated 24 hours before, cluster around the root tip and grow hyphae towards the root.

After 2-3 days, some SBNs ($n = 3-5$ per root) were found inside roots (usually near the root apex) with their body aligned with the central vein of the root. The rhythmic motion of the stylet (i.e. hollow, feeding tube) was observed in the real-time videos. This is characteristic of plant-parasitic nematodes that use their stylets to secrete substances and establish feeding sites within the root.

Compared to SBNs ($\sim 400 \mu\text{m}$ long), *P. sojae* zoospores (i.e. motile spores) are much smaller in size ($\sim 3-5 \mu\text{m}$ in diameter) and show a different mode of interaction (Figure 5.5b). Upon inoculation, the zoospores swim randomly in the microchannels and start settling at locations close to the root tip in the first 2 hours.^{31,32} They form clusters as they settle, encyst, germinate, and grow their hyphae³¹ (i.e. germ tubes) in the next 6 hours to penetrate the root tissues. In our control experiments (i.e. without roots),

zoospores swell to form appressoria and the hyphae generally grow in random directions.³³ In the presence of roots, appressoria are also formed but with a majority of hyphae extending towards the root (Figure 5.5b). In subsequent days, the root tip appears darker indicating possible localized cell death (Figure 5.6).³⁴

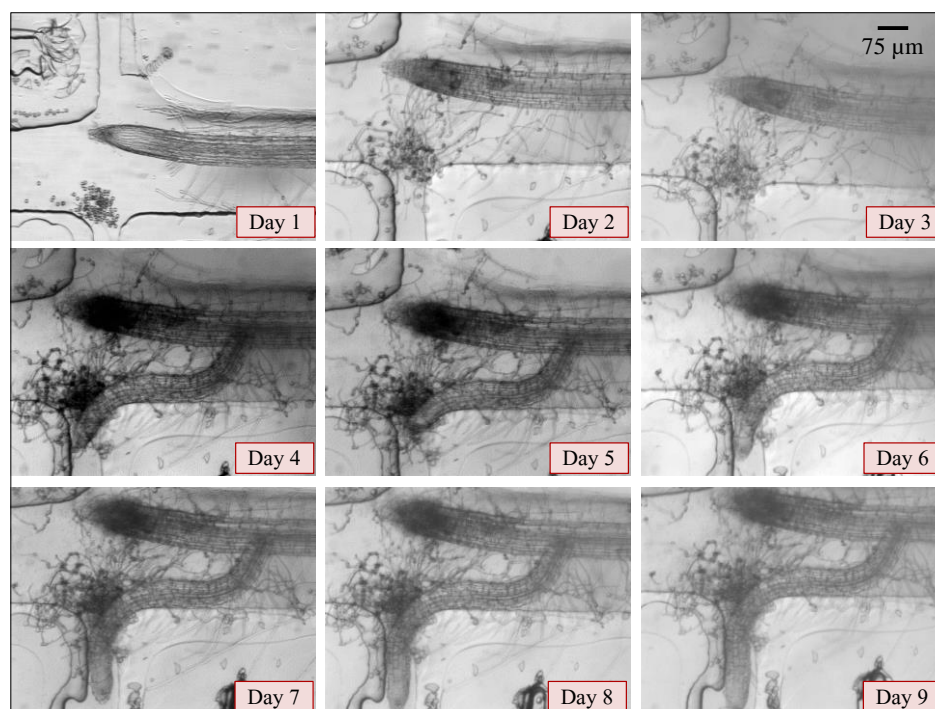


Figure 5.6 Time-lapsed images of *P. sojae* interaction with *Arabidopsis* root in microchannels.

5.5 Conclusion

In conclusion, this plant-in-chip platform harnesses the known advantages of microfluidics technology¹⁵ to conduct experiments in root development and root-pathogen interactions. We showed reliable and steady growth of *Arabidopsis* roots in microchannels with imaging at cellular resolution. The root morphology was influenced by different MS concentrations and opens possibilities of testing other nutrients and stress factors.^{6,14,18} The hydroponic growth of *Arabidopsis* seedlings in transparent,

closed microenvironments over long time periods offers improved throughput in conducting parallel growth tests and eliminates the need of macroscopic agarose plates¹⁴ for culturing seedlings. The real-time imaging of root-pathogen physicochemical interactions demonstrated here can significantly advance our knowledge about the plethora of physiological and molecular changes undergoing in the host or non-host system during pathogenic attack.^{3,4} Phenotypic characterization of the complex interactions between these multi-kingdom organisms in such microfluidic platforms can complement existing genetic and proteomic screening tools¹⁶ aimed at engineering nematode-resistant plant mutants and identifying the possible defense strategies (e.g. physical or chemical barriers)^{8,23} employed by plant systems.

5.6 References

1. X. Fu and N. P. Harberd, *Nature*, 2003, **421**, 740-743.
2. Q. Li, B. Li, H. J. Kronzucker, and W. Shi, *Plant, Cell and Environment*, 2010, **33**, 1529-1542.
3. P. Bonfante and I. Anca, *Annual Review of Microbiology*, 2009, **63**, 363-383.
4. A. E. Little, C. J. Robinson, S. B. Peterson, K. F. Raffa, and J. Handelsman, *Annual Review Microbiology*, 2008, **62**, 375-401.
5. B. R. Borlee, G. D. Geske, H. E. Blackwell, and J. Handelsman, *Applied and Environmental Microbiology*, 2010, **76**, 8255-8257.
6. J. L. Dangl and J. D. G. Jones, *Nature*, 2001, **411**, 826-832.
7. B. Forde and H. Lorenzo, *Plant and Soil*, 2001, **232**, 51-68.
8. P. Achard, H. Cheng, L. D. Grauwe, J. Decat, H. Schoutteten, T. Moritz, D. V. Straeten, J. Peng, and N. P. Harberd, *Science*, 2006, **311**, 91-94.

9. H. Zhang and B. G. Forde, *Science*, 1998, **279**, 407-409.
10. G. Beemster and T. I. Baskin, *Plant Physiology*, 1998, **116**, 1515-1526.
11. G. Beemster and T. I. Baskin, *Plant Physiology*, 2000, **124**, 1718-1727.
12. P. N. Benfey, P. J. Linstead, K. Roberts, J. W. Schiefelbein, M. Hauser, and R. A. Aeschbacher, *Development*, 1993, **119**, 57-70.
13. C. S. Buer, J. Masle, and G. Wasteneys, *Plant Cell Physiology*, 2000, **41**, 1164-1170.
14. H. Kanani, B. Dutta, and M. I. Klapa, *BMC Systems Biology*, 2010, **4**, 177-181.
15. F. Migliaccio, A. Fortunati, and P. Tassone, *Plant Signaling & Behavior*, 2009, **4**, 183-190.
16. N. Yazdanbakhsh and J. Fisahn, *Annals of Botany*, 2010, **105**, 783-791.
17. P. Basu, A. Pal, J. Lynch, and K. M. Brown, *Plant Physiology*, 2007, **145**, 305-316.
18. X. Qi, J. Qi, and Y. Wu, *Plant Root*, 2007, **1**, 10-16.
19. N. D. Miller, B. M. Parks, and E. P. Spalding, *Plant Journal*, 2007, **52**, 374-381.
20. A. French, S. Ubeda-Tomas, T. J. Holman, M. J. Bennett, and T. Pridmore, *Plant Physiology*, 2009, **150**, 1784-1795.
21. M. Meier, E. Lucchetta, and R. F. Ismagilov, *Lab on a Chip*, 2010, **10**, 2147-2153.
22. G. M. Whitesides, *Nature*, 2006, **442**, 368-373.
23. D. B. Weibel, W. R. DiLuzio, and G. M. Whitesides, *Nature Review of Microbiology*, 2007, **5**, 209-218.
24. B. Dutta, H. Kanani, J. Quackenbush, and M. I. Klapa, *Biotechnology and Bioengineering*, 2009, **102**, 264-278.
25. T. Ingestad and G. I. Agren, *Ecological Applications*, 1991, **1**, 168-174.
26. H. Zhang and B. G. Forde, *Journal of Experimental Biology*, 2000, **51**, 51-59.
27. P. C. Sijmons, F. M. W. Grundler, N. von Mende, P. R. Burrows, and Urs Wyss, *Plant Journal*, 1991, **1**, 245-254.

28. W. Grunewald, G. van Noorden, G. van Isterdael, T. Beeckman, G. Gheysen, and U. Mathesius, *Plant Cell*, 2009, **21**, 2553-2562.
29. N. Wuyts, G. Lognay, R. Swenne, and D. De Waele, *Journal of Experimental Biology*, 2006, **57**, 2825-2835.
30. V. Williamson and C. Gleason, *Current Opinion in Plant Biology*, 2003, **6**, 327-333.
31. E. Huitema, J. I. Bos, M. Tian, J. Win, M. E. Waugh, and S. Kamoun, *Trends in Microbiology*, 2004, **12**, 193-200.
32. D. Takemoto, D. A. Jones, and A. R. Hardham, *Plant Journal*, 2003, **33**, 775-792.
33. P. F. Morris, E. Bone, and B. M. Tyler, *Plant Physiology*, 1998, **117**, 1171-1178.
34. J. E. Rookes, M. L. Wright, and D. M. Cahill, *Physiology and Molecular Plant Pathology*, 2008, **72**, 151-161.

Chapter 6

Conclusions

In this thesis, a combination of microfluidics and real-time imaging is employed to characterize behavioral traits of nematodes, particularly the non-parasitic *C. elegans*. We realized that the power of engineering tools could only be successfully harnessed by pursuing biologically-driven hypotheses in close collaboration with biologists. We aimed at designing simple-to-use devices with user-friendly software interface that could eventually be passed on to biology laboratories. To some extent, we were able to achieve this goal. Modified versions of the devices discussed in the thesis are currently being used in experiments for phenotyping plant-and animal-parasitic worms, screening pharmacological agents, culturing higher plant systems, and assaying attractants/repellants on human parasites. It is worth mentioning that several chip designs, initially fabricated for *C. elegans* research, have now been adopted in testing other parasites with minor modifications.

The thesis started with a survey of some microfluidic systems for whole-animal screening, primarily capturing single worms, exposing them to chemical stimuli, and imaging neuronal or pharyngeal signals. We described protocols for fabricating

microfluidic devices, culturing *C. elegans*, and using a worm tracking program. A great deal of emphasis was placed on standardization of developed methods, statistical relevance of data, environmental conditions, and health of organisms during experiments, along with sufficient control replicates.

The work in Chapter 2 resulted from our observations of worm movement on agarose plates. Worms moved in sinusoidal manner and seemed to use their body force for forward/backward movement. Because the generated body force was known to be related to their amplitude and wavelength, we investigated worm movement in sinusoidal microchannels with modulating amplitude. We discovered that different mutants had different degrees of body flexibility that allowed them to crawl through distinct ranges of amplitudes. This passive device thus provided a portable platform to study the physical adaptability of free-moving microscopic nematodes, especially with and without applied stress.

In Chapter 3, we studied worm locomotion upon exposure to a chemical toxicant, potassium cyanide. While wild-type animals were sensitive to cyanide toxicity, deletion of specific genes induced different levels of resistance to the toxin. In this case, the design of the microfluidic device was challenging as worms were repelled by the toxin and, invariably, found ways to exit the microfluidic device. The proposed device allowed injection of worms through constricted ports and subsequent imaging over 15 minutes. A worm tracking program helped us extract multiple parameters that adequately described cyanide toxicity and resistance across different genetic backgrounds. The method is

currently being used to study the effects of hypergravity on *C. elegans* under different experimental conditions.

To show the applicability of the above cyanide testing device for screening other chemical compounds, we conducted experiments on the lethality of four anthelmintics that are known to damage the neuromuscular system of nematodes. The dose response of the four anthelmintics was characterized, which reflected the inherent resistance of *C. elegans* to the compounds. Increasing resistance of nematodes to available drugs is a well-recognized and growing problem, and discovery of new anthelmintics on biological hypotheses is a time-consuming, expensive process. We wished to investigate how our microfluidic screening platform could be applied for drug discovery, beyond directly testing available compounds. We hypothesized that a drug combination may be superior to existing drugs (even at low concentrations of individual drugs). An algorithmic search approach, previously demonstrated in cell culture experiments by our collaborator (Dr. Chih-Ming Ho, UCLA), was used to identify a winning drug combination that killed *C. elegans* at concentrations below EC_{50} values of the individual drugs.

The above devices could be applied for behavioral analysis of parasitic worms; however, such studies are best conducted *in vivo* where the parasite is in close contact with its host. Chapter 5 describes a method to grow *Arabidopsis* plant roots in microfluidics, which are subsequently used as host systems for plant-parasitic nematodes. Unlike previous experiments, this system required culture of healthy plants over 7-days and monitoring of root-nematode interactions over the next 10-days. We characterized root growth parameters over this prolonged time period and made visual

observations of nematode penetration within roots. This method is currently being explored for growing soybean roots with different treatments and studying the effectiveness of these treatments in inhibiting/repelling nematodes.

To summarize, there are identifiable problems in whole-animal studies, with significant social and economic importance, that could be addressed using tools developed in bioengineering. The ability to make physical structures with dimensions on the scale of microorganisms under study and computer-controlled image recognition programs has immense potential to revolutionize parasitology through active interdisciplinary collaborations between nematologists, geneticists, and engineers. Undoubtedly, the near future promises exciting technological advancements in bioengineering that will accelerate biological discoveries and directly impact our society.

LIST OF PUBLICATIONS

Journal Publications

1. **Archana Parashar**, Xianting Ding, Chih-Ming Ho, Santosh Pandey, “Algorithm-guided discovery of new combinations of existing drugs for parasitic worms”, under preparation.
2. Roy Lycke, **Archana Parashar**, Santosh Pandey, “Microfluidics-enabled method to identify modes of *C. elegans* paralysis in four anthelmintics”, *Biomicrofluidics*, 7, 064103 (2013).
3. **Archana Parashar***, Jenifer Saldanha*, Santosh Pandey, Jo Anne Powell-Coffman, “Multi-parameter behavioral analyses provide insights to mechanism of cyanide resistance in *Caenorhabditis elegans*”, *Toxicological Sciences*, 135, 156-168 (2013)
* first authors.
4. **Archana Parashar**, Santosh Pandey, “Plant-in-chip: Microfluidic system for studying root growth and pathogenic interactions in *Arabidopsis*”, *Applied Physics Letters*, 98, 263703 (2011) Selected as “frontier research article” by *Virtual Journal of Nanoscale Science & Technology*, vol. 24, issue 2, 2011.
5. **Archana Parashar**, Roy Lycke, John Carr, Santosh Pandey, “Amplitude-modulated sinusoidal microchannels for observing adaptability in *C. elegans* locomotion”, *Biomicrofluidics*, 5(2), 024112 (2011) Selected as “frontier research article” by *Virtual Journal of Biological Physics Research*, vol. 22, issue 1, 2011.
6. John Carr, **Archana Parashar**, Richard Gibson, Alan Robertson, Richard Martin, Santosh Pandey, “A microfluidic platform for high-sensitivity, real-time drug

screening on *C. elegans* and parasitic nematodes”, Lab on a Chip, 11, 2385-2396 (2011). Amongst the top ten accessed articles from the online version of Lab on a Chip in the month of June 2011.

7. Baozhen Chen, **Archana Parashar**, Santosh Pandey, “Folded floating-gate CMOS biosensor for the detection of charged biochemical molecules”, IEEE Sensors Journal, 11, 11, 2906 – 2910, (2011).
8. John Carr, **Archana Parashar**, Roy Lycke, Santosh Pandey, “Unidirectional electrotactic -response valve for *C. elegans*”, Applied Physics Letters, 98, 143701 (2011) Selected as “frontier research article” by Virtual Journal of Biological Physics Research, vol. 21, issue 8, 2011.
9. Santosh Pandey, Andrew Joseph, Roy Lycke, **Archana Parashar**, “Decision-Making by nematodes in complex microfluidic mazes”, Advances in Bioscience and Biotechnology, 2, 6, 409-415 (2011).
10. Abhishek K. Singh, **Archana Parashar**, Amit K. Singh, Rajeev Singh, “Pre-natal/juvenile chlorpyrifos exposure associated with immunotoxicity in adulthood in Swiss albino mice.”, Journal of immunotoxicology, 10, 2, 141-149 (2013).

Conference Publications

1. Jenifer Saldanha, **Archana Parashar**, Santosh Pandey, Jo Anne Powell-Coffman, “Effects of HIF-1 over-activation: Real-time assays for toxin response”, Aging, Metabolism, Pathogenesis, Stress, and Small RNAs, Poster presentation, Wisconsin, July 12-15 (2012).

2. Santosh Pandey, Andrew Joseph, Richard Gibson, Roy Lycke, **Archana Parashar**, John Carr, “Interaction of *C. elegans* Microorganisms with Hard, Soft and Hybrid Interfaces in Microchannels”, Materials Research Symposium, Oral presentation, San Francisco, 25-29th April (2011).
3. Santosh Pandey, **Archana Parashar**, Baozhen Chen, “Manipulation and Filtering of Nematodes and their Mutants in Modulated Sinusoidal Trenches”, Materials Research Symposium (MRS), Oral presentation, San Francisco, 25-29th April (2011).
4. Jenifer Saldanha, **Archana Parashar**, Qi Ye, Santosh Pandey, Jo Anne Powell-Coffman, “Deciphering *hif-1* regulatory networks: An interdisciplinary approach to diagnosing stress resistant phenotypes”, 18th International *C. elegans* Meeting Poster presentation, University of California at Los Angeles, June 22-26th (2011).
5. Santosh Pandey, **Archana Parashar**, Rishi Sumit, Madan K. Bhattacharyya, “A Microfluidic Platform for Long-term, Real-time Monitoring of *Arabidopsis thaliana* Root Growth Patterns”, Plant & Animal Genomes XIX Conference, Poster presentation, San Diego, January 15-19th (2011).
6. Santosh Pandey, Adam Bohl, Xuotong Mao, John Carr, **Archana Parashar**, “Artificial Soil: Substrate with Controlled Heterogeneity for Automatically Sorting and Screening Microscopic Worms”, Materials Research Symposium, Poster presentation, San Francisco, April 25-29th (2011).

APPENDIX

Buffer Recipes:**1. M9 buffer for *C. elegans* experiments (from wormbook)**

3 g KH_2PO_4

6 g Na_2HPO_4

5 g NaCl

1 mL 1 M MgSO_4

Added reagents to 900 mL of H_2O .

Adjusted the pH to 6.0 with 1 N NaOH/HCl.

Adjusted the final volume to 1 L with H_2O .

Sterilized by autoclaving.

2. MS media for growing *Arabidopsis* (from Cold Spring Harbor Protocols)

4.33 g Murashige and Skoog basal medium (Sigma M5519)

20 g sucrose

Added reagents to 900 mL of H_2O and stir until dissolved.

Adjusted the pH to 5.7 with 2 N KOH.

Adjusted the final volume to 1 L with H_2O .

Sterilized by filtration at room temperature.